T CHANNEL DYNAMICS IN A SILICON LGN

Kai Michael Hynnä

A DISSERTATION

in

Bioengineering

Presented to the Faculties of the University of Pennsylvania in Partial Fulfillment of the Requirements for the Degree of Doctor of Philosophy

2005

Kwabena Boahen,	John Schotland,
Supervisor of Dissertation	Graduate Group Chair

Acknowledgements

I would like to thank all of the people who have helped me along the way in the completion of this work.

To my advisor Kwabena Boahen: Thanks for all of your guidance and training over the years. The road was long and sometimes bumpy, but the journey well worth the effort. I am grateful for your patience and your support.

To my committee members Leif Finkel, Carson Chow, Diego Contreras and Bertram Shi: Thanks for all of your time and your advice. Your individual perspectives provided valuable insight into my work.

To my lab members: Many thanks for all of the shared experiences, for all of your help, for all of your creativity and ingenuity, and even for all of the mindless banter. Good luck in your future endeavors.

Most importantly, to those whose Paths have at some point crossed my own; to those who have shared their laughter and their spirit; to those who I have had the good fortune of knowing, both recently and in years past; to my Friends: Thanks.

Abstract

T CHANNEL DYNAMICS IN A SILICON LGN

Kai Michael Hynnä

Supervisor: Kwabena Boahen

This dissertation describes my efforts, in silicon, to study the role of the low threshold calcium channel in the processing of visual information in the lateral geniculate nucleus. Historically, neuroscientists have considered the LGN as simply a relay station for retinal transmission to the visual cortex. However, the LGN does not function alone; rather, it exists within a complicated network of feedback from both the reticular nucleus and the cortex.

The approach that I use to study geniculate function involves the design of silicon circuits of increasing model complexity. I begin at the channel level, modelling the low threshold calcium channel using a transistor analog of state transition rates for a voltage gated channel. Following validation of this model, I integrate this channel into a silicon cell and demonstrate how its state influences the cell's response. The next level of complexity involves the dynamics between a thalamocortical and an inhibitory reticular cell, probing their response to inputs at both retinal and cortical synapses. Finally, the system is extended to include many cells, in an effort to illuminate network operation.

Using this approach, I demonstrate the role of the low threshold calcium current in enhancing strong features within visual stimuli. In addition, through influence of synapses to both thalamic and reticular layers, the cortical feedback acts as an

attentional mechanism by which the response to weaker features can be markedly enhanced, through both increased bursting and increased excitability.

Contents

List of Tables

List of Figures

Chapter 1

Introduction

The lateral geniculate nucleus (LGN) is the primary visual division of the dorsal thalamus, and is the first stop for visual information from the retina en route to the cortex. Historically considered a relay station by neurobiologists, recent evidence suggests its role may involve more than a simple, unfiltered transfer of ascending sensory information.

Two properties of thalamic cells suggest a larger role for the thalamus in the awake animal. First, thalamic cells possess a low-threshold calcium channel, the state of which dramatically alters the response of the cell from individual spikes to a high-frequency burst of spikes. Recordings from unanesthetized awake animals have demonstrated bursts due to this channel, but the role of this channel in thalamic processing is not yet understood. Second, thalamic cells form reciprocal connections with two other areas of the brain: the reticular nucleus—a thin sheet of cells surrounding the thalamus—and the cortex. Chapter 2 provides a brief background on the thalamus, beginning with the visual response of thalamic cells and the influence

of the low-threshold calcium channel on their dynamics. Following that, I discuss the influence of those areas which form reciprocal connections with the thalamus, first describing the visual response of the perigeniculate nucleus (the visual section of the reticular nucleus) and its influence on thalamic cells, and then the influence of the cortical feedback on the thalamo-reticular system.

I structure the rest of the dissertation based on increasing complexity of my silicon model. Chapter 3 begins at the level of the low threshold calcium channel (also called the T channel). Before describing my silicon model, I begin by providing background on various models of the low threshold calcium channel. Many silicon models of voltage-dependent channels are silicon analogs of empirical Hodgkin-Huxley computational models. However, the models are incomplete: while capable of capturing the steady-state dynamics of activation and inactivation, they lack the dependence of the time constants on the membrane voltage. Taking inspiration from thermodynamic models, my model captures this temporal dependence through modelling of state transition rates. After presenting my approach and my model, I present data from the silicon chip demonstrating its operation.

The next step is to incorporate the channel model into a silicon neuron, which is the focus of Chapter 4. I begin by describing the complete neuron circuit, consisting of the T channel, the cell and an excitatory synapse. This chapter studies the changes in the TC cell response caused by the activation of the calcium channel, to compare the operation of my silicon neuron to similar experiments on real neurons. Given the voltage-dependence of the calcium channel, shifting the resting potential of the cell changes the 'mode' of the cell, from burst (T channel active) to tonic (T channel inactive). In the first set of experiments, I calculate the frequency response of my silicon neuron to injected current for each mode, and compare its performance to

results from biology.

The second set of experiments probes changes in the response of the cell by using an adaptation of the Wiener series to calculate a set of kernels describing system function. Rather than using Gaussian White Noise (as injected current), I use Poisson Spike Trains at the input synapses to probe the response with the cell in both modes. There are a couple of advantages to using spike trains over white noise for cells away from the sensory organs. First, the computed kernels include synapse dynamics in addition to the membrane and T channel dynamics. The other advantage of using spike trains is that the higher-order kernels are easier to interpret visually than those calculated using white noise, due to the discrete nature of spikes. I verify the ability of the kernels to capture system dynamics in each mode by using them to generate a spike train of the cell and comparing the generated output to the actual output of the silicon cell. Including higher order kernels into the system improves the ability the kernels to capture the output response, especially in burst mode given the nonlinear nature of the T channel.

In Chapter 5, I introduce a reticular cell into the system, studying the influence of the reticular cell on the response of the TC cell. Typically, in the awake state, thalamic cells are sufficiently depolarized such that the T channel, by default, is inactivated. Therefore, inhibition is necessary to deinactivate the T channel, placing importance on the role of reticular activity in the presence of bursts within the thalamus. This chapter demonstrates that the presence of bursts indicate the presence of strong, salient signals within the retinal inputs.

In addition, I probe the effects of the cortical feedback on the dynamics within the system. The cortical input, being weaker in nature, increases the background input

to both cells, increasing their excitability and reducing the threshold for the presence of bursts. Thus, the cortex can increase the probability of bursting for stimuli that would normally respond only in tonic mode in the retina-only scenario. This suggests a role for the cortical feedback similar to an attention mechanism.

The final chapter extends the results of the two cell system to the network (population) level. The discussion in this chapter revolves around the visual response properties of the reticular cells, since it is the inhibition from this layer that defines the existence of bursts in the LGN. Experimental results from my silicon population demonstrate how the number of bursts in the thalamic layer increases with stimulus size, since the divergence of axons between the TC and RE layers means greater inhibition for deinactivation with greater population activity. I end the chapter with a discussion of how this applies to processing within the visual system.

Chapter 2

The Thalamo-Reticular System

The dorsal thalamus[1] is an oval-shaped subcortical structure located in the center of the brain (Figure 2.1), and—along with the ventral thalamus, epithalamus, and hypothalamus—belongs to the embryonic division called the diencephalon[66]. It consists of a number of nuclei (Figure 2.2), each dedicated to a different information pathway to the neocortex. All sensory information, except olfactory, passes through a nucleus en route to their respective cortical regions; for this reason, the thalamus is often called the "gateway" to the cortex. These nuclei, however, are not limited to servicing ascending sensory information paths: Many nuclei mediate corticocortical connections.

Historically, neurobiologists have considered the thalamus as a simple relay station for ascending information in the awake animal. However, a couple of observations

[1] The dorsal thalamus is often referred to as simply the *thalamus* when discussing thalamocortical systems, since ventral thalamic cells do not project to the cortex. Since I will be focusing primarily on the dorsal thalamus, I will adopt this naming convention and only add the qualifier 'dorsal' when distinguishing it from the ventral thalamus.

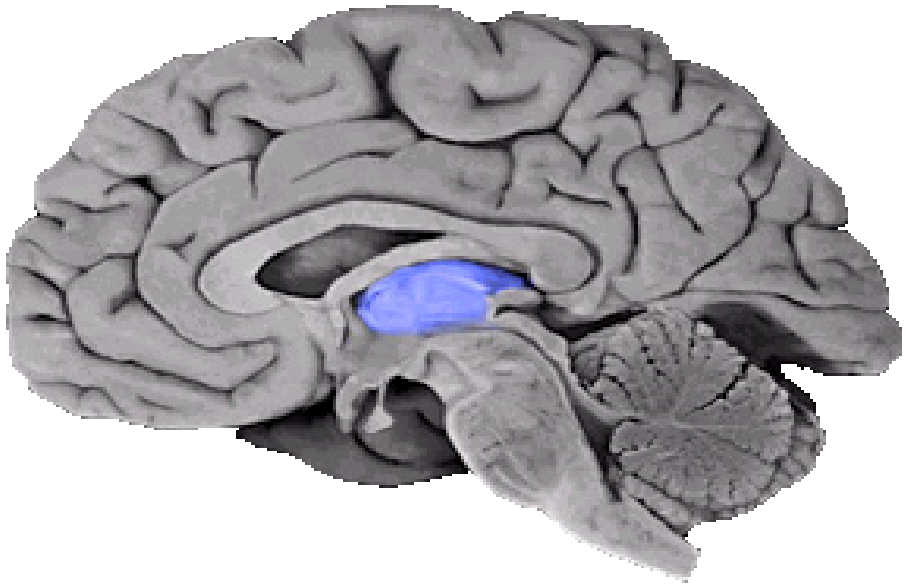

Figure 2.1: Dorsal Thalamus

Sagittal view of the brain, showing the location of the dorsal thalamus (blue).

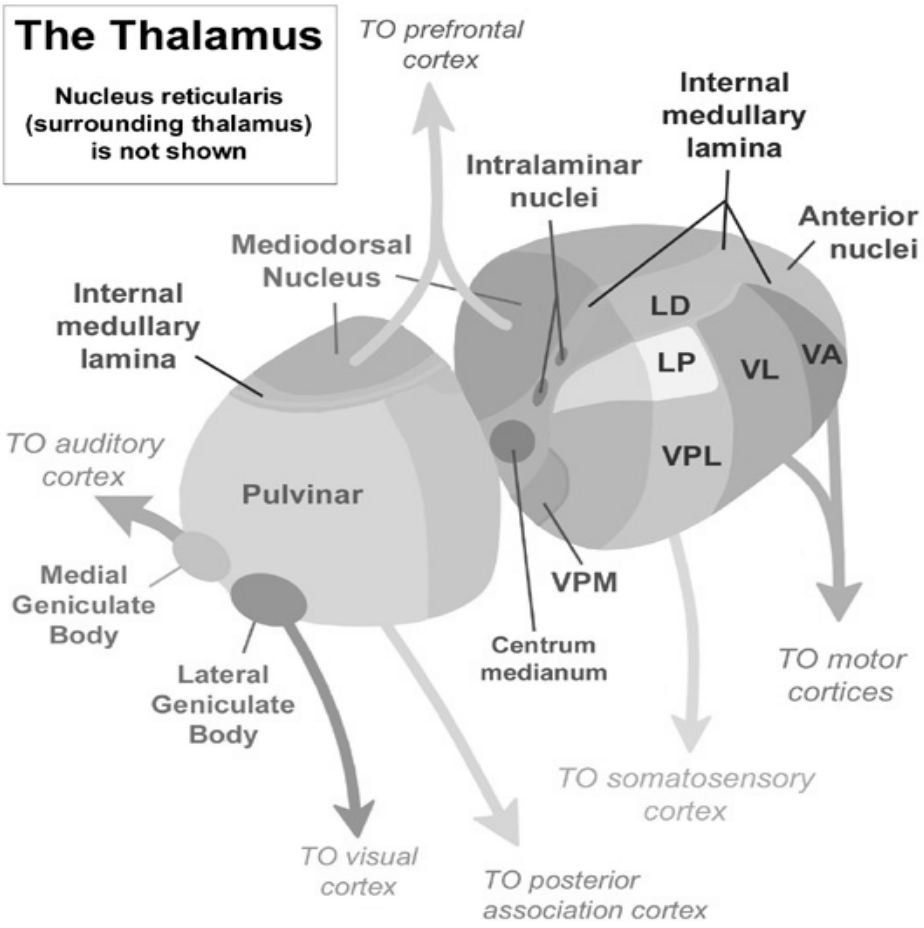

Figure 2.2: Subdivisions of the Dorsal Thalamus

Diagram of the subdivisions of the right dorsal thalamus. LD, Lateral Dorsal Nucleus; LP, Lateral Posterior Nucleus; VPL, Ventroposterior Lateral Nucleus; VL, Ventrolateral Nucleus; VA, Ventral Anterior Nucleus; VPM, Ventroposterior Medial Nucleus. From [97].

about thalamic cells—also called relay neurons or thalamocortical (TC) cells—suggest a more involved role in sensory processing. The first is of a low threshold calcium channel within the membrane of the cell[64]. This channel can dramatically alter the response of the relay neuron from a low-frequency *tonic* mode, where the output rate is strongly dependent on the input, to a high-frequency *burst* mode where the output rate is largely *independent* of the input. The state of this channel depends on sufficient hyperpolarization of the membrane voltage. During sleep, the membrane voltage of thalamic cells rests lower than when the animal is awake[52]. It is not surprising, then, that the calcium channel—also called T channel—is involved in many of the oscillations during sleep[93]. The higher membrane voltage during the awake state has, historically, been considered sufficient to keep the T channel inactivated[133, 66]. Recent experiments, described below, demonstrate the presence of the channel activity within thalamic cell responses of an awake animal. Its precise role, however, remains unclear.

The second observation is of the complex circuitry within which TC cells exist (Figure 2.3). Each relay nucleus forms reciprocal connections with two other areas of the brain. The first area is the *reticular nucleus* (TRN), a thin sheet of cells surrounding the dorsal thalamus and belonging to the ventral thalamus. Reticular neurons receive excitation from collaterals of the thalamocortical axons[1, 4] and project their inhibition back into their associated relay nucleus[66], forming an excitatory-inhibitory loop with relay neurons. The second area with which TC cells form reciprocal connections is the cortical destination for the TC cell axons. Feedback axons from the cortex, called corticothalamic axons, make up approximately 30% of the inputs into the thalamus[31, 146], exciting relay cells through both ionotropic and metabotropic glutamate receptors. And like thalamocortical axons, corticothalamic axons send col-

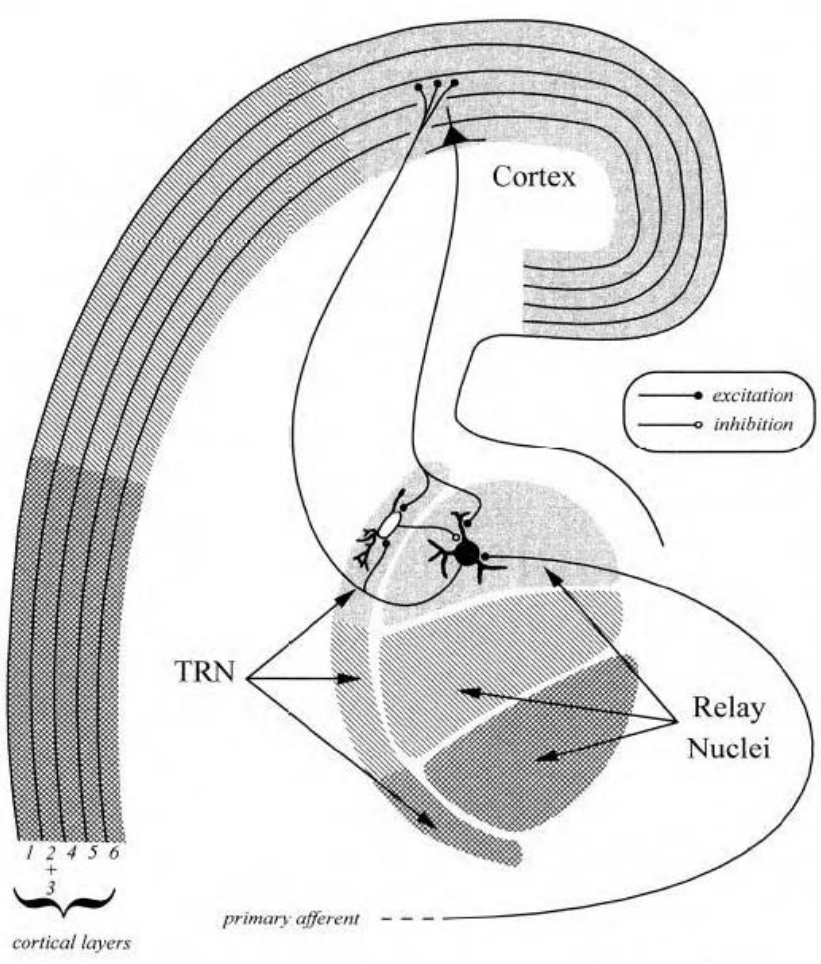

Figure 2.3: Thalamocortical Circuit

Primary afferents into the thalamic nuclei form excitatory synapses on relay cells. Relay cell axons pass through the reticular nucleus (TRN) and project to layer 4 of the cortex. Layer 6 cells, from the same cortical area, send axons back to the thalamus, also passing through the TRN. Reticular cells, receiving both feedforward and feedback excitation, send inhibition back into the thalamic nucleus. From [121].

laterals into the reticular nucleus[3], influencing the feedback inhibition from reticular cells. Thus, cortical influence on the thalamus can be both excitatory and inhibitory.

This chapter provides a brief background on the thalamo-reticulo-cortical system, focusing on the visual pathways in the awake animal. The primary visual nucleus within the thalamus is the lateral geniculate nucleus (LGN), and the visual section of the reticular nucleus is called the perigeniculate nucleus (PGN)[2]. Cells within any relay nucleus are referred to as thalamocortical (TC) cells or relay neurons, while cells specifically in the LGN are called geniculate neurons. Since I am focusing on the visual system, I use these three designations interchangeably, but will predominantly use the term TC cell. Cells within the reticular nucleus are called reticular cells (RE) cells, or perigeniculate (PGN) cells when referring specifically to vision. As in the case of TC cells, I will use both terms for reticular cells interchangeably, but will predominantly use the term RE cells.

The first section in this chapter describes response properties of cells within the LGN, describing first visual responses followed by the influence of the low threshold calcium channel on the cell output. The second section describes the visual response properties of the inhibitory cells within the PGN, and their influence on LGN cells. The final section discusses the observed influence of the cortical feedback on both LGN and PGN cells.

[2]Though the perigeniculate nucleus is a separate area from the reticular nucleus, neurobiologists often group them together given the similarity in both structure and connectivity[66]. For the purposes of my thesis, the distinction is not important.

2.1 Thalamocortical Cells

It is not surprising that neurobiologists considered the thalamus a simple relay station: The low convergence of ganglion cell axons to geniculate cells (as low as one or two[145, 89, 90]) results in many similarities in their visual responses. Geniculate receptive fields, like those of ganglion cells, consist of an excitatory center with an inhibitory surround[56, 114, 74]. Cells excited by light within their receptive field center are called ON cells; by dark, OFF cells. In the cat, relay neurons, also like retinal cells, are classified as either X or Y[14], depending on the linearity of their response. Spatial input into X cells sum linearly, allowing for a "null" response where the positive and negative spatial inputs cancel[30]. Y cells are nonlinear: They do not possess a null response, and demonstrate "frequency-doubling" through responses on both the rising and falling edge of a square stimulus. X cells have smaller receptive fields ($< 1°$, depending on the eccentricity) compared to Y cells ($< 1.5°$) [54], and thus respond better at higher spatial frequencies. Though X and Y cells in the thalamus are typically identified through their visual responses, they can also be identified through their morphology[34].

Within the thalamus itself, there is a further division of the response in the temporal domain into lagged and nonlagged cells[88, 89]. The input to nonlagged cells is mediated through fast glutamatergic receptors, presumably AMPA[45], replicating the responses of their ganglion cell inputs to flashing spots: for an X-cell, a strong initial transient, followed by a sustained output for the duration of the stimulus. Lagged cells, as the name implies, demonstrate a delay in their response in place of the strong transient. After about 20-30ms[88], the lagged cell slowly increases to a sustained response level. The initial delay is from a fast inhibition—possibly from local inhibitory

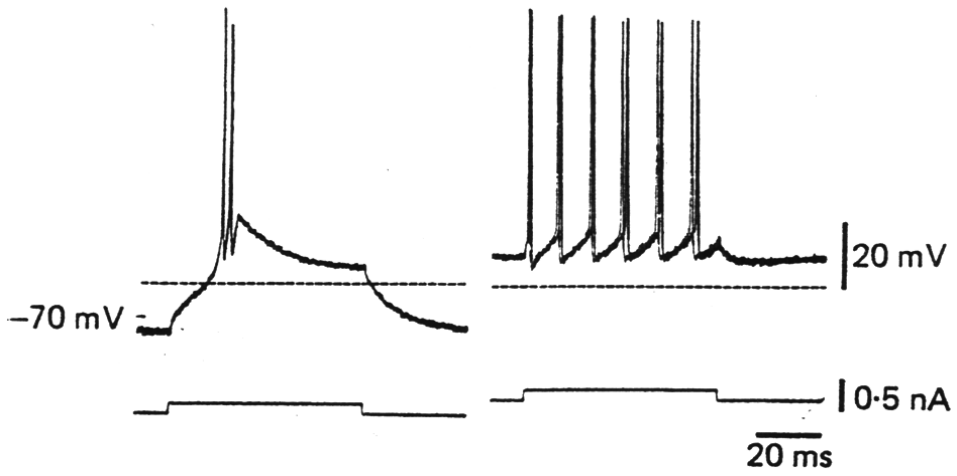

Figure 2.4: TC Cell Response Modes

Thalamocortical cells can exhibit two distinct responses to similar inputs, depending on the state of a low threshold calcium channel within the membrane. LEFT: From an initial hyperpolarized level (which deinactivates the calcium channel), a step in the input results in a high-frequency burst, ending when the channel has inactivated. RIGHT: From an initial more depolarized membrane voltage, a similar step in the input current results in a steady train of output spikes. The channel, in this case, has been inactivated due to the resting membrane voltage. From [64].

interneurons—while the slow excitation derives from NMDA receptors[46]. One role for lagged and nonlagged cell types is the generation of direction selectivity within cortical cells[118, 119].

The most interesting characteristic of relay neurons is the low threshold calcium channel. This channel—often called a T channel—gives the cell the ability to demonstrate two very different responses (Figure 2.4). Assuming the channel has been deinactivated, depolarization of the membrane potential demonstrates two characteristics of the channel dynamics (Figure 2.4(left)): a fast activation, which hastens

the cell depolarization and causes the cell to elicit a burst of Na^+ spikes, and a slower inactivation, which closes the channel and ends the burst. Full inactivation occurs after approximately 25-30ms, after which the cell needs to be hyperpolarized for greater than 100ms to deinactivate the channel. By contrast, a cell that is initially depolarized—such that the T channel is inactivated—responds to the same depolarization with a steady train of single spikes (Figure 2.4(right)). In this situation, since the channel is already inactivated, the frequency of the spikes depends on the level of the injected current, while within a burst the frequency is predominantly defined by the channel current.

The influence of this channel has dramatic effects on the response properties of the cell. Figure 2.5(a) plots the output frequency of the cell to varying steps in the input current under these two modes. The tonic mode (here called single spike) of the cell has a linear response above its rheobase (current threshold). The burst mode is non-linear: Once the input current is able to sufficiently depolarize the cell, the output frequency jumps to over 300Hz, much greater than in the single spike mode. Further increases in input current linearly increases the output frequency, but negligibly compared to the influence of the channel.

The linear/non-linear nature is further demonstrated in Figure 2.5(b). The histograms in the bottom row show the response of both modes to four cycles of a drifting grating in the visual field. The linear tonic mode is able to faithfully reproduce, through the histogram, the shape of the visual stimulus. The burst mode, though able to respond during each cycle, provides no information on the finer details of the stimulus. Another interesting feature in Figure 2.5(b) is the difference in the spontaneous activity of both modes. The hyperpolarization needed to deinactivate the T current, presumably through a membrane leak, acts as a higher current

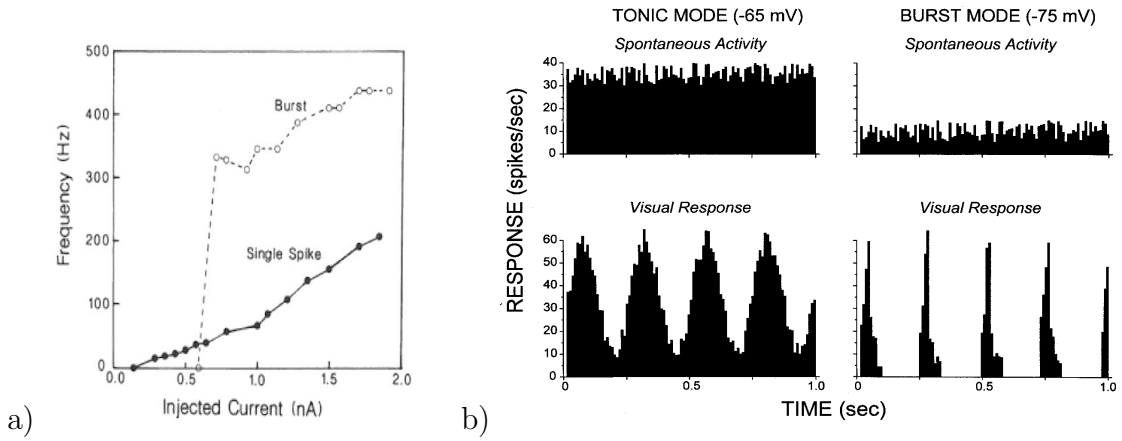

Figure 2.5: Response Mode Properties

a) Output frequency versus input current for the relay cell in its two response modes. *Single Spike* refers to tonic mode, where the initial membrane voltage is sufficiently high to inactivate the T channel. For the burst response, the cell begins sufficiently hyperpolarized for channel deinactivation. Output frequency calculated using the initial interspike in response to a step to the new current level. From [94]. b) Peri Stimulus Time Histogram of spontaneous activity (top row) and visual response (bottom row) to drifting gratings for geniculate cells biased, using injected current, to either tonic (left column) or burst modes (right). From [124].

threshold (also seen in Figure 2.5(a)), reducing the spontaneous activity within the cell.

In these experiments, the state of the channel, and thus the response mode, is biased through changes in the resting membrane potential by an injected current. This is not wholly unrealistic, as TC cells possess a K^+-leak within the membrane that can perform this very function. In addition, the level of this leak can be adjusted through either metabotropic receptors activated by cortical glutamatergic inputs[95, 39] or through activation of ascending inputs from the parabrachial region[84]. This suggests

that the response of the cell, through the state of the channel, can be modulated by sources external to the thalamus, depending on the type of processing that is required.

These results have led to the hypothesis that bursts function as a "wake-up" call to the cortex[121]. In this scenario, the absence of attention to a portion of the visual scene—which, presumably, corresponds to a reduction of cortical feedback—increases the membrane K^+ leak for cells in that area. This high leak state has two functions in addition to deinactivating the T channel: it keeps the spontaneous background 'noise' low while also acting as a higher threshold, causing the cell to respond only to strong stimuli. Thus, since bursts are a strong signal to cortical cells[137, 144], bursting is a powerful indicator of a strong stimulus within an unattended area of the visual field. This strong burst signal activates the cortex, sending corticothalamic feedback to the same retinotopic area. Through the action of metabotropic receptors[95, 39], the resting potential of the TC cell rises, inactivating the T channel and switching the response mode of the cell to tonic. The tonic mode, then, sends more detailed information (Figure 2.5(b)) of the stimulus to the cortex.

There are a couple of problems with this idea. First, relay cells are depolarized in the awake state[52], sufficiently so to keep the channel inactivated[133]. The burst response in the wake-up hypothesis requires a resting membrane potential sufficiently low to deinactivate the T channel, so that the absence of an input, or a shift in attention, primes the burst response. However, for depolarized cell, this is not possible.

Another problem with the "wake-up" hypothesis deals with the use of cortical or subcortical inputs to controls the depolarization level of the cell. There is no doubt that these mechanisms exist[95, 39, 84], the question is whether they could function as described. First, the time constant of both of these mechanisms are on the order of

a second: for example, two spikes at 3-500Hz from the corticothalamic axons caused a small depolarization for 3-4 seconds, while 10 spikes caused depolarizations greater than 20 seconds[95]. Considering the eye makes saccades approximately three times per second[47, 48], a slow depolarization of this duration would incapacitate areas of the visual field that have been switched to tonic mode. Given the low frequency and number of spikes needed to cause the depolarization, it seems more likely the cell is *already* depolarized during the awake state.

In many of the studies that focussed on the burst response[41, 109, 78], it is not clear how much the anesthesia, which increases the number of bursts[87], influenced the results. Does this mean bursts do not exist in the awake state? Not necessarily: bursts have been observed in the LGN of awake, unanesthetized monkeys[107] and cats[42], in addition to the somatosensory thalamus of the rat[32]; but their precise role is not clearly understood.

Many researchers also work under the assumption of two distinct responses; that is, the cell either responds in burst or tonic mode. Part of this is the limitation of detecting bursts: most studies use extracellular recordings and only are able to use the spike train statistics[83], rather than recording either the membrane voltage or being able to record T channel activation directly. Once fully deinactivated, the activation of the T channel demonstrates an all-or-none response similar to the faster Na^+ channel response within the action potential; as such, it has been described as a Ca^{++} *spike*[157]. But the size of the response is defined by the level of deinactivation[157], suggesting that the T channel need not function in two distinct modes, but in a continuum with the burst and tonic at the two extremes.

With the cell depolarized in the awake state, deinactivation of the T channel

requires inhibition of sufficient strength and duration. A source of inhibitory action onto TC cells, as mentioned previously, is the reticular nucleus. Thus, understanding the response properties of the reticular cells could shed some light on the role of I_T, which is the focus of the next section.

2.2 Reticular/Perigeniculate Cells

Perigeniculate receptive fields are much larger than those of the geniculate cells, approximately 5° in diameter[29], but can range from $3 - 10^\circ$[35]. Since geniculate cells are the only source of excitatory ascending input[1], there is a convergence from multiple geniculate cells. Like the geniculate nucleus[117], the reticular nucleus is retinotopic in organization[99].

Sudden changes in contrast within the receptive field of PGN cells, such as a spot stimulus, elicits a transient response at both the on- and offset (Figure 2.6(a)), but generates a negligible sustained response. Increasing the stimulus size increases the size, and reduces the latency, of the transient[35], presumably through the activity of a greater number of geniculate cells. PGN cells also demonstrate strong responses to moving stimuli[29, 35]—stronger than to static stimuli (Figure 2.6(b))—through the transient activity of the underlying geniculate cells within the receptive field[35]. Interestingly, the output spikes are not phase-locked to the edges of the drifting grating; rather, the enhancement due to the motion tends to be a general increase in the firing rate of the cell[35].

Inhibition from the PGN cell on the TC cell is mediated through both $GABA_A$ and $GABA_B$ receptors. At low reticular frequencies, the inhibitory response in a TC cell

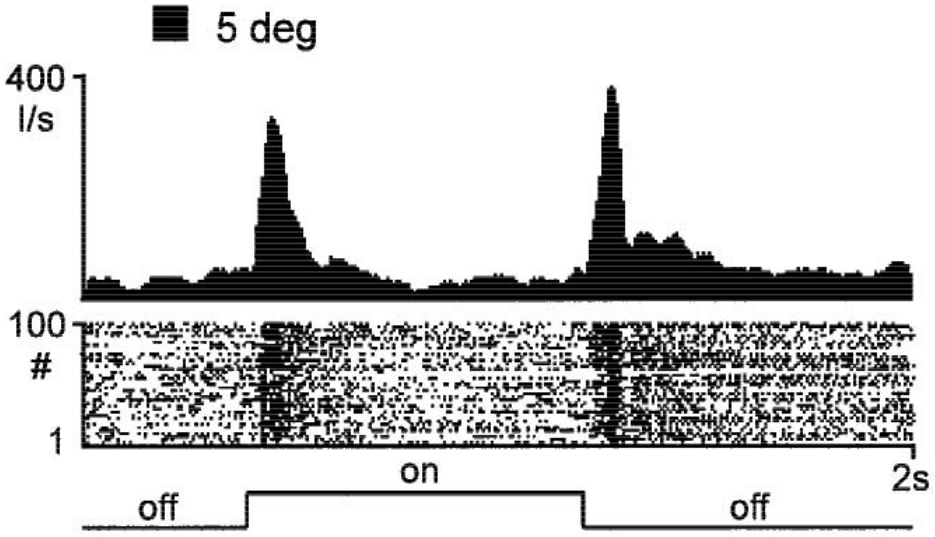

(a)

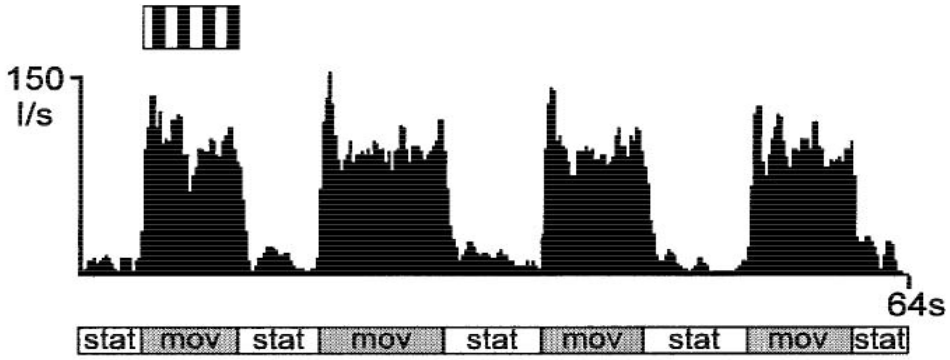

(b)

Figure 2.6: PGN Cell Responses

a) Peri Stimulus Time Histogram (PSTH) and raster plot of a PGN cell response to a spot (5 degrees in diameter). b) PSTH of a cell responding to alternating patterns of a stationary (stat) and moving grating (mov). From [35].

is dominated by fast, $GABA_A$ dynamics[70]. To activate the slow $GABA_B$ response, a single PGN cell needs to fire at high frequencies for a prolonged period of time[70]. Regardless of the receptor type, inhibition from a single neuron—mediated through both $GABA_A$[141, 148] and $GABA_B$[140] receptors—is capable of deinactivating the low-threshold calcium channel in TC cells if the cell fires strongly for a sufficient duration. However, a synchronous volley of inputs from a population of cells could deinactivate the T channel under $GABA_A$[28] and $GABA_B$[116].

Figure 2.7 shows the response of an ON center geniculate Y-cell to a large 20°x20° square flashed over its receptive field. The inhibitory dip immediately post-peak is from perigeniculate inhibition[35]. The second peak immediately after the inhibition is the rebound burst caused by deinactivation of the T channel by the PGN input, since retinal inputs, whether X or Y, demonstrate only the initial peak[30]. Given the increase in PGN response to stimulus size[35] and that a synchronous response from RE cells could deinactivate the T channel[28, 116], it is possible the size of the rebound burst correlates with the size of the stimulus. This agrees with the observation that geniculate cells in awake cats demonstrate greater burst probability for larger stimuli[152].

Reticular cells also possess a low threshold calcium channel, similar to that within the TC cell but slower in dynamics[59]. Interactions between the burst response of TC and RE cells are responsible for spindle oscillations seen during sleep[93]. In the awake state, RE cells, like TC cells, are depolarized[134]. Compared to TC cells, RE cells require greater inhibition for T channel deinactivation[28], suggesting RE bursts are less likely to appear than TC cell bursts. Though there are suggestions that reticular bursts may represent different processing states in the awake rat[44], the reticular cells, in the context of this document, are considered to remain in tonic

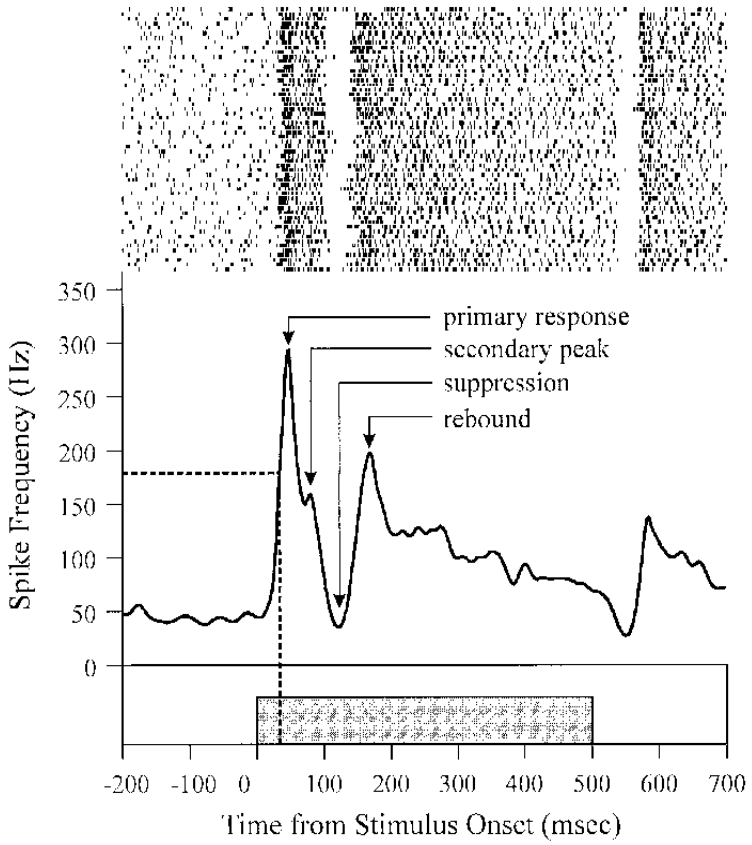

Figure 2.7: Geniculate Response to a Large Stimulus

Response of an ON center Y-cell to a 20°x20° square presented within 500ms after a saccade. Note that the histogram is generated relative to the onset of the flash stimulus, rather than the saccade. The flash onset relative to the saccade varies from 0-500ms. From [77].

mode.

2.3 Role of the Cortical Feedback

Corticothalamic axons make up approximately 30% of the synapses onto relay neurons[31, 146]. Like thalamocortical axons, they also send collaterals in the reticular nucleus as they pass through[65, 135], providing both excitatory and inhibitory influences to thalamic cells. Also like the relay and the reticular nuclei, the corticothalamic axons preserve the topography of the retinal space[142, 102].

Corticothalamic axons that feed back to the LGN derive from cells in layer VI of the visual cortex. These cells are strongly direction selective[126], and as such, many studies have focussed on changes in the geniculate response to moving bars. These studies suggest a cortical enhancement of the inhibitory surround of geniculate cells by cortical activity[101, 17], affecting such properties as length-tuning[101], and sensitivity to discontinuities in orientation[125].

This feedback can also influence the burst response of geniculate cells. As already discussed previously, corticothalamic axons activate metabotropic receptors on TC cells[95, 39], reducing a membrane leak in the cell causing depolarization, and thus inactivating the T channel. But changes in the layer VI activity can also increase the number of bursts[149]. Applying $GABA_B$ receptor antagonists to layer VI cells of the visual cortex enhances the gain of the visual response of these cells without adjusting their spontaneous rate. This increased gain in layer VI caused 68% of geniculate cells to change their ratio of burst to tonic firing, with 63% of those showing less bursting and the remaining cells showing more.

These examples provide direct evidence that the cortical feedback influences the response of individual geniculate cells to visual input. In a larger context of brain function, evidence suggests that attentional mechanisms can influence activity as early as the LGN[103], in the form of enhanced responses to attended stimuli versus attenuated responses to unattended stimuli, and increased baseline activity in the absence of visual stimulus. Many theories focus on the role of the reticular nucleus in attention (reviewed in [91]), which is not so surprising given that corticoreticular synapses are stronger than corticothalamic synapses[40]. Lesions of the reticular nucleus eliminate the attentional advantages of a visual cue preceding a target in reaction time tasks in rats[151]. In addition, the reticular nucleus in rats demonstrated higher levels of activity in those areas used during active exploration[98].

2.4 Summary

This chapter provides some background into the influence of both the low threshold calcium channel and the cortical feedback on the response properties of relay neurons. The results presented here are by no means exhaustive; rather, they are meant to provide a basis from which to proceed. It should be clear, however, that the thalamus acts more than a simple relay for information en route to the cortex, given the influence of the various components described here. The rest of this document explores the role of the T channel in the context of the network interactions between the reticular cells and the cortical feedback, using silicon as the medium of study.

Chapter 3

Silicon Model

In the previous chapter, I provided some background on the thalamo-reticular system, discussing the influence of the T channel and the reticular and cortical feedback on the TC cell response. The next two chapters describe the design and verification of my silicon model of the system, beginning with my approach to designing a silicon analog of the low threshold calcium channel.

The first section begins with a description of existing computational models of the T channel, which provides a background on the dynamics of the channel but also a framework from which I will model the T channel. Following that, I provide a succinct description of the transistor, the building block of neuromorphic models, and proceed to describe existing neuromorphic models of voltage-dependent channels.

I then proceed to describe the motivation for my design, demonstrating how it can be implemented in silicon. Following an analysis of my circuit, I present experimental data from a silicon chip that verifies the behavior of my design.

3.1 T Channel Models

Numerous models of ion channels exist[24], each possessing a different degree of complexity, accuracy and biological basis. In an ideal world, most researchers would choose the most accurate model available; however, in practice, most people choose their model based on their available computational resources, as greater accuracy usually translates to greater complexity and a need for more resources. This section explores two different models of the T channel: empirical and thermodynamic models.

3.1.1 Empirical Models

Over 50 years ago, Hodgkin and Huxley[53] introduced a framework through which to study the dynamics of an excitable membrane. Their approach describes conductance changes of an ion channel with respect to changes in the membrane potential of a cell. Though they focussed only on the Na^+ and K^+ channels involved in action potential generation, their technique was easily adaptable to the myriad of ion channels that exist in the nervous system. For this reason, their approach provides the basis for many modern computational models.

In their model, each ion channel consists of a series of independent "gating particles", whose binary state—open or closed—determines the channel permeability. A *Hodgkin-Huxley* (HH) variable represents the probability of a particle being in the open state, or, with respect to the channel population, the fraction of gating particles that are in the open state. The dynamics of the HH variable can be described by

$$u \quad \underset{\beta\,(\mathrm{V})}{\overset{\alpha\,(\mathrm{V})}{\rightleftharpoons}} \quad (1-u)\,, \tag{3.1}$$

where u is the HH variable and represents the fraction of open states, $(1-u)$ represents the fraction of closed states, and $\alpha\,(\mathrm{V})$ and $\beta\,(\mathrm{V})$ are the transition rates (dependent on the membrane voltage V) for opening and closing respectively. Based on this two-state model, the kinetics of the HH variable are represented by

$$\frac{\mathrm{d}u}{\mathrm{dt}} = \alpha\,(\mathrm{V})\ (1-u) - \beta\,(\mathrm{V})\ u. \tag{3.2}$$

Typically, Equation 3.2 is expressed in the following form:

$$\frac{\mathrm{d}u}{\mathrm{dt}} \;=\; -\frac{1}{\tau_{\mathrm{u}}\,(\mathrm{V})}\,(u - \mathrm{u}_{\infty}\,(\mathrm{V})) \tag{3.3}$$

where u_{∞} and τ_{u} represent the steady-state level and time-constant functions for u respectively, and are defined as

$$\mathrm{u}_{\infty}\,(\mathrm{V}) \;=\; \frac{\alpha\,(\mathrm{V})}{\alpha\,(\mathrm{V}) + \beta\,(\mathrm{V})} \tag{3.4}$$

$$\tau_{\mathrm{u}}\,(\mathrm{V}) \;=\; \frac{1}{\alpha\,(\mathrm{V}) + \beta\,(\mathrm{V})}. \tag{3.5}$$

A channel model consists of multiple HH variables, the product of which represents the probability of a channel being open. The channel current, $\mathrm{I_{ch}}$, is defined as

$$\mathrm{I_{ch}} \;=\; \left(\prod_{i=1}^{n} u_i\right)\; \overline{\mathrm{g}}\; (\mathrm{V} - \mathrm{E_{rev}}), \tag{3.6}$$

where u_i is one of n HH variables for this channel, $\overline{\mathrm{g}}$ is the maximum channel conductance, V is the membrane voltage, and $\mathrm{E_{rev}}$ is the reversal potential for the ion. The equations $\mathrm{u_\infty}\,(\mathrm{V})$ and $\tau_{\mathrm{u}}\,(\mathrm{V})$ are determined empirically, by fitting exponential functions to experimental data.

For some channels, however, it is not accurate to model the channel dynamics as changes in the channel conductance. This is true for calcium channels, to which belongs the thalamic low-threshold calcium current. The large imbalance between extracellular and intracellular concentrations of calcium cause a nonlinear current-voltage relationship[51]. In these situations, rather than modulate a conductance, the HH variables modulate a maximum permeability. Thus, many modelling studies of the low threshold calcium current (e.g. [58, 27, 157]) use the following form:

$$\mathrm{I_T} \;=\; m^2 h\; \overline{\mathrm{P}}_{\mathrm{Ca}}\; \mathrm{G}(\mathrm{V}, \mathrm{Ca_o}, \mathrm{Ca_i}) \tag{3.7}$$

where $\overline{\mathrm{P}}_{\mathrm{Ca}}$ is the maximum permeability of the T channel, m and h are the HH variables (for activation and inactivation respectively), and $\mathrm{G}(\mathrm{V}, \mathrm{Ca_o}, \mathrm{Ca_i})$ is the Goldman-Hodgkin-Katz current equation, which captures the nonlinear dependence

Eqn.	Activation (m)	Inactivation (h)
$\mathrm{u}_\infty(V)$	$\frac{1}{1+\exp\left[-\frac{V+56}{6.2}\right]}$	$\frac{1}{1+\exp\left[\frac{V+80}{4}\right]}$
$\tau_\mathrm{u}(V)$	$0.204+\frac{0.333}{\mathrm{e}\left[\frac{V+15.8}{18.2}\right]+\mathrm{e}\left[-\frac{V+131}{16.7}\right]}$	$9.32+0.333\ \mathrm{e}\left[-\frac{V+21}{10.5}\right]; V \geq -81$ $0.333\ \mathrm{e}\left[\frac{V+466}{66.6}\right]; V < -81$

Table 3.1: Steady State and Time Constant Equations for Relay Cell Model

This table displays the equations used for activation and inactivation in the Hodgkin-Huxley model of $\mathrm{I_T}$. All voltages are in millivolts. These equations are plotted in Figure 3.1. From [23].

of $\mathrm{I_T}$ on both the membrane voltage and internal and external calcium concentrations. T channel dynamics are best represented with two independent gating particles for activation (m^2) and one for inactivation (h). Table 3.1 presents, and Figure 3.1 plots, the steady-state and time-constant functions for the HH variables of $\mathrm{I_T}$ for relay cells[58].

How do these variables interact to shape $\mathrm{I_T}$? Figure 3.2(a) plots the time course of the gating variable product m^2h to depolarizing step changes in the membrane voltage of a simulated TC cell. The cell begins in a hyperpolarized state (-90mV) with $\mathrm{I_T}$ deinactivated. Once the step size is sufficiently large, the gating variable product begins to demonstrate a response: a fast rise due to the activation variable (m) followed by a slow decay due to the inactivation variable (h). Further increasing the step size results in an increase in the rate and magnitude of response. Eventually,

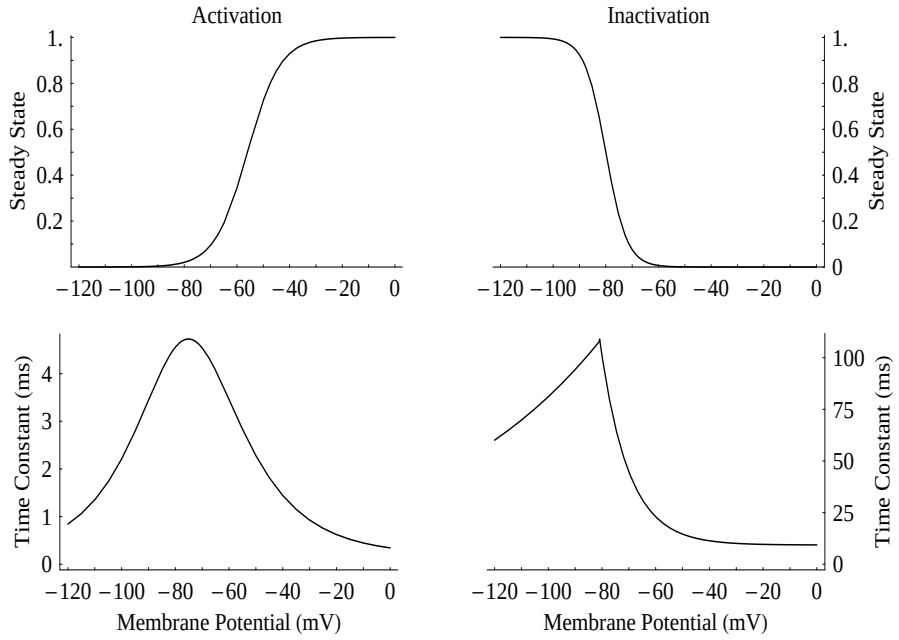

Figure 3.1: Activation/Inactivation Parameters for TC cells

These four figures plot the equations from Table 3.1, showing the steady state and time constant dependence on membrane potential for the Hodgkin-Huxley variables of the relay neuron. The left column plots activation equations and the right inactivation; the top row shows the steady state levels for each variable and the bottom the time constant.

a characteristic shape forms as the variable functions asymptote at higher membrane voltages (Figure 3.1).

Figure 3.2(b) plots another simulation, this time demonstrating the dependence of the response on the level of channel deinactivation. An inactivated T channel requires sufficient hyperpolarization—both in time and in magnitude—to conduct again. The experiment varies the total time the cell is hyperpolarized, from an initial inactivated state, before being depolarized again. As shown in Figure 3.2(b), progressively longer

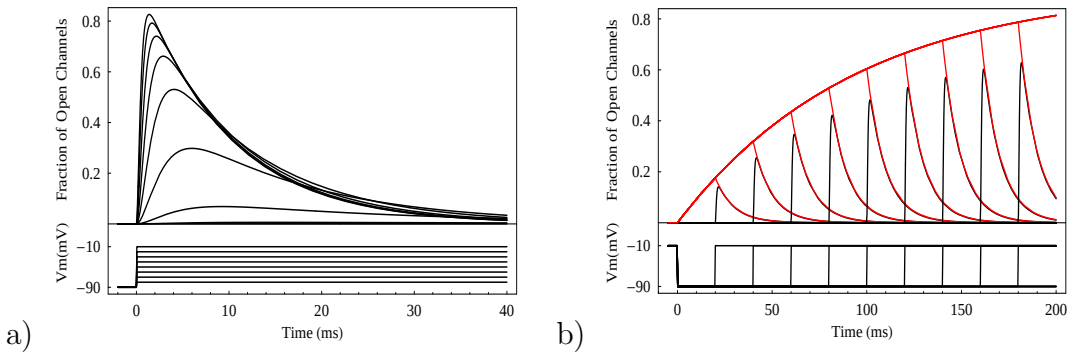

Figure 3.2: Channel activation

These two plots demonstrate the time course of the I_T variable pair m^2h for a model TC cell to two simulated 'voltage clamp' experiments. (a) The cell begins hyperpolarized (at −90mV) so that the T channels begin deinactivated. At t = 0s, the membrane potential is stepped to different depolarized levels (from −80mV to −10mV), demonstrating the time course of activation and inactivation at the different membrane voltage levels. (b) This figure shows the deinactivation of the variable product. The cell is initially depolarized (at −10mV) and the channel inactivated. At t = 0s, the voltage is stepped down to −90mV for increasing time intervals and then re-depolarized. The deinactivation is demonstrated by the increase in the peak response. The inactivation variable h is plotted in red.

periods of hyperpolarization result in larger responses upon depolarization. This effect is due to the increased deinactivation of h (plotted in red).

Unfortunately, voltage clamp experiments—like the simulations in Figure 3.2—provide only a glimpse into the channel dynamics; in reality, the membrane voltage is rarely fixed. However, the two simulated experiments in Figure 3.2 do provide clues to the roles the two variables may play in the dynamics of the channel. Activation of the T channel has a positive feedback effect: the current I_T depolarizes the cell,

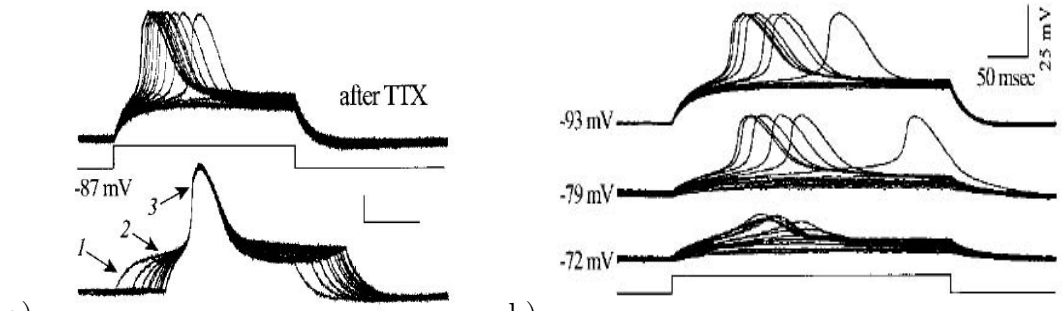

a) b)

Figure 3.3: Variable Influences on I_T

a) Current clamp experiments demonstrating the influence of the activation variable. The membrane voltage begins hyperpolarized, deinactivating I_T; steps in the input current level adjust the response of the membrane voltage. At lower step size, there is insufficient activation for the burst to occur. Once the level of activation is sufficient for I_T to overcome any passive membrane leaks, I_T quickly depolarizes the cell, generating a Ca^{++} spike. b) Changing the initial membrane voltage changes the size of the Ca^{++} spike. From [157].

opening more channels. This generates a Ca^{++} *spike* (Figure 3.3(a)), an 'all-or-none' event like its (faster) Na^{+} channel counterpart, the action potential. The activation variable defines the point at which I_T overcomes the ohmic response of the membrane. As demonstrated in Figure 3.2(a), small initial depolarizations result in a slow, small activation, and thus a longer latency for the Ca^{++} spike (if generated at all). Larger depolarizations will result in a faster initial activation, and thus a smaller latency.

While the activation plays a role in the temporal position of the I_T response, the inactivation variable controls the shape and size of the response. Both the duration (Figure 3.2(b)) and level (Figure 3.3(b)) of the hyperpolarization influences the deinactivation of I_T, which then affects the size of the Ca^{++} spike[157, 158] and the

number of Na^+ spikes in the burst[158].

This suggests that the dynamics of the inactivation variable are more important to the function of the T channel than the dynamics of activation. In fact, many of the frequency response properties of the TC cell in burst mode can be captured using a simple, threshold model for the T channel[130], which includes only the temporal dynamics of inactivation (activation occurs instantaneously). In addition, this simple model highlights the importance of the increase in the inactivation time constant during channel deinactivation (compared to inactivation), demonstrating the necessity of this feature in any model of I_T to correctly capture the channel dynamics.

3.1.2 Thermodynamic Models

Since empirical models are fits to experimental data, their form have no basis on the physical structure of ion channels. Thermodynamic models attempt to explain the state changes of a gating particle through conformational changes of the ion channel protein[50, 23, 24].

Figure 3.4 shows a diagram of the free energy between two states (G_0 and G_1) and an intermediate, activated (transitional) state (G^*). The rate of transition between two states (say, from G_0 to G_1) depends exponentially on the free energy barrier ΔG_0 [51]. Thus, for a two-state variable (Equation 3.1), the reaction rates are defined as

$$\alpha(V) = \alpha_0 \, e^{-\Delta G_0(V)/RT} \tag{3.8}$$

$$\beta(V) = \beta_0 \, e^{-\Delta G_1(V)/RT}, \tag{3.9}$$

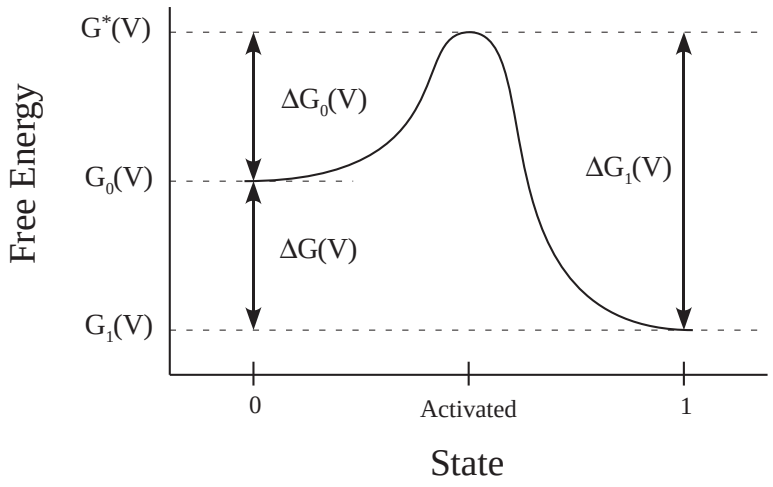

Figure 3.4: Free Energy Reaction Diagram

The transition rates between two states is dependent on the height of the free energy barriers (ΔG_0 and ΔG_1), which involves the difference in free energy between the activated state (G^*) and the initial state (G_0 or G_1). The steady-state level of the reaction depends on the relative difference in free energy between the states (ΔG), while the time constants of reaction depends on the height of the free energy barrier.

where $\alpha(V)$ is the voltage-dependent transition rate from G_0 to G_1, $\beta(V)$ is the reverse transition rate (from G_1 to G_0), α_0 and β_0 are constants representing base transition rates, $\Delta G_0(V)$ and $\Delta G_1(V)$ are the voltage-dependent free energy barriers (the difference between the free energy of the activated state and the initial state), R is the gas constant and T is the temperature in Kelvin.

The steady-state of the reaction is based on the relative values of the free energy between the two states. In other words, at equilibrium, the ratio of open versus closed states depends on the free energy between them: $u/(1-u) = \exp[-\Delta G/R\,T]$. The time course of the reaction depends on the size of the free energy barrier. Larger

barriers have slower dynamics, since fewer molecules within a state have the necessary energy to overcome the barrier.

The voltage dependence of the free energy for each state (initial, final and activated) depends on the effect of the electric field on the ion channel protein. This nonlinear voltage dependence can be approximated using a Taylor expansion:

$$\mathrm{G}_i\,(V) = \mathrm{A}_i + \mathrm{B}_i\,V + \mathrm{C}_i\,V^2 + \ldots \tag{3.10}$$

where $\mathrm{G}_i\,(V)$ is the free energy of conformational state i, and A_i, B_i, C_i, ... are constants defining the dependence of the free energy for this state to changes in the electric field. A_i represents any free energy that is independent of the electric field. The linear term (B_i) and nonlinear terms (C_i, D_i, ...) corresponds to such effects as the interaction of isolated charges and dipoles with the electric field[50, 136], or the mechanical constraints in the movement of charges[50, 23] due to the structure of the ion channel protein.

It follows, then, that the free energy barrier can also be represented as a Taylor series, being difference in free energy of the activated and the initial states. Thus, the reaction rates (Equations 3.8 and 3.9) become

$$\alpha\,(V) = \alpha_0\,\mathrm{e}^{-\left(\mathrm{a}_1+\mathrm{b}_1\,V+\mathrm{c}_1\,V^2+\ldots\right)/\mathrm{R\,T}} \tag{3.11}$$

$$\beta\,(V) = \beta_0\,\mathrm{e}^{-\left(\mathrm{a}_2+\mathrm{b}_2\,V+\mathrm{c}_2\,V^2+\ldots\right)/\mathrm{R\,T}} \tag{3.12}$$

where a_1, a_2, ... represent the difference between the coefficients of the Taylor series for the initial and activated states.

For linear thermodynamic models, the nonlinear voltage terms are discarded, and the variables rearranged to achieve the following form:

$$\alpha(V) = A\, e^{-b_1 (V - V_H)/RT} \tag{3.13}$$

$$\beta(V) = A\, e^{-b_2 (V - V_H)/RT} \tag{3.14}$$

where V_H is the half-activation voltage, b_1 and b_2 are the linear terms of the transition rates on the membrane voltage, and A is the half-activation rate. Figure 3.5 shows the fit of the linear model to voltage clamp data. While the steady-state data is easily captured, the model is unable to fit both the steady-state and time constant equations simultaneously. This is due to the relationship between the slopes of the steady-state sigmoid and the slopes of the time constant curve on either side of the peak. As a result, the time constants drops more rapidly at hyperpolarized voltages.

The biggest problem with these linear models, however, involves the decay of the time constant to very small values at voltages distant from the location of the peak. At these voltages, the exponential within the transition-rate equations reach very high values, thus bringing the time constant close to zero. However, this problem with can be resolved by either saturating the transition rate[153] or by using a three-state model[24], where the transition rates between two of the states are fixed and effectively set the minimum time constant.

Including higher-order terms in the free energy barrier equation improves the fit of the model. For a cubic expansion[23]:

$$\alpha\,(V) = A\,\mathrm{e}^{-\left(\mathrm{b_1}(V-\mathrm{V_H})+\mathrm{c_1}(V-\mathrm{V_H})^2+\mathrm{d_1}(V-\mathrm{V_H})^3\right)/\mathrm{R\,T}} \tag{3.15}$$

$$\beta\,(V) = A\,\mathrm{e}^{-\left(\mathrm{b_2}(V-\mathrm{V_H})+\mathrm{c_2}(V-\mathrm{V_H})^2+\mathrm{d_2}(V-\mathrm{V_H})^3\right)/\mathrm{R\,T}} \tag{3.16}$$

where the additional constants (compared to the linear case) are for the higher order voltage dependencies (as described above).

The cubic expansion improves on the ability of the model to fit the voltage-clamp data, coming very close to matching the empirical equations from Section 3.1.1. The higher-order terms counter the increasing exponential within the linear expansion to set a minimum time constant within the voltage range of operation. Thus, these nonlinear thermodynamic techniques provide a more biologically plausible way to model the dynamics of the T channel over the empirical ones.

3.2 Silicon Background

Before choosing a model from which to base my own, it is useful to provide a brief background on the transistor, the fundamental building block of VLSI chips. Following that, I proceed to detail some of the previous models designed by other neuromorphic engineers to model neural circuits. Finally, in this section, I describe the basis for my own model.

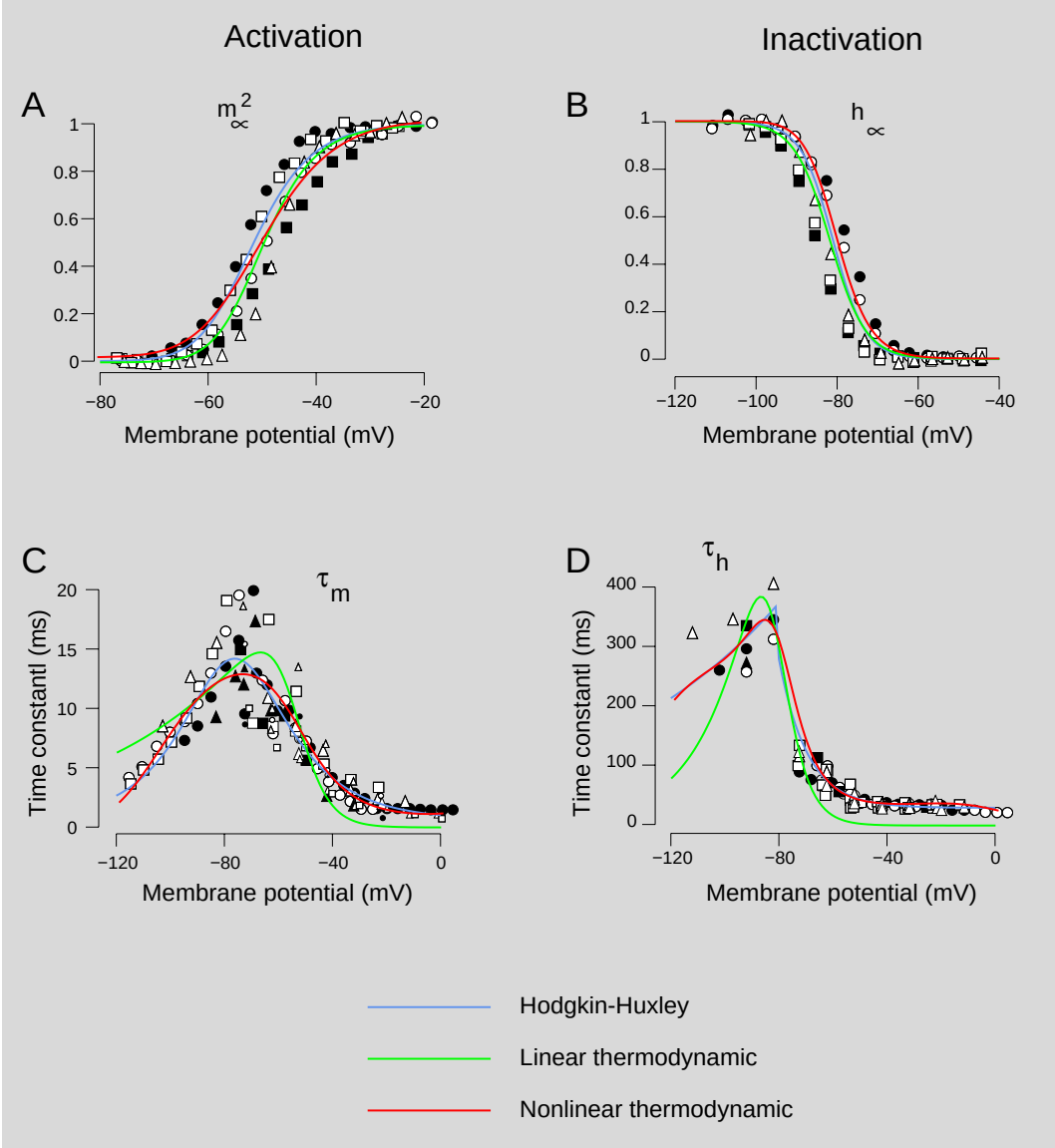

Figure 3.5: Empirical and Thermodynamic HH Equations

Steady-state and time constant equations for activation and inactivation HH variables versus experimental data from cells. The equations in Table 3.1 and Figure 3.1 have been adjusted for temperature compared with the data and equations plotted here. From [24].

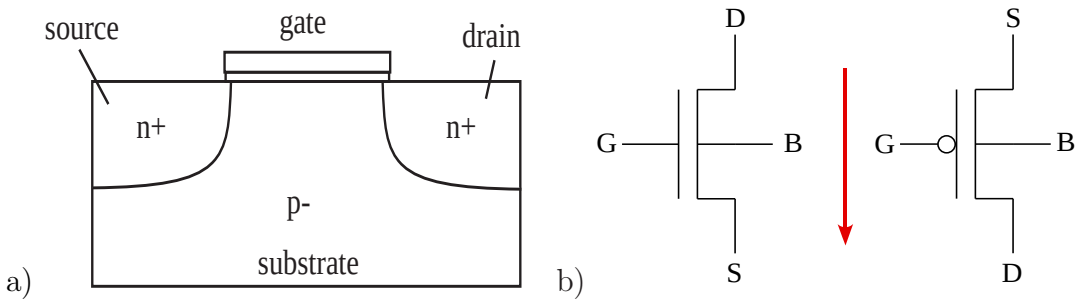

Figure 3.6: CMOS Transistor

(a) Cross-sectional diagram of an n-type MOS transistor. (b) Schematic Representation of the two transistor types: the nFET (left) and the pFET (right). The transistor has four terminals: *source* (S), *drain* (D), *gate* (G) and *bulk* (B), or sometimes referred to as the *back-gate*. The transistor is a symmetric device, and thus the direction of the channel current—by convention the flow of positive charges—defines the drain and the source. In an nFET, current flows from drain to source as indicated by the arrow. Conversely, current in the pFET flows from source to drain.

3.2.1 Transistor Basics

The basic building block of neuromorphic models—and much of the computer industry—is the MOS transistor. Short for *Metal Oxide Semiconductor*, the MOS transistor is named for its structure: a **metallic** *gate*[1] atop a thin **oxide** insulator which separates the gate from a **semiconductor** channel. The channel, part of the *body* or *substrate* of the transistor, lies between two heavily doped regions called the *source* and the *drain* (Figure 3.6(a)), between which current flows. There are two types of MOS transistors: n-type and p-type Field Effect Transistors (nFETs and pFETs respectively). The nFET possesses a drain and a source that are heavily doped n-type

[1]Nowadays, a polysilicon gate.

regions within a p-type substrate[2]. A pFET consists of a p-type source and drain within an n-type well.

In the subthreshold regime, current flows within the channel by diffusion from the higher charge density at the source end to the lower charge density at the drain end. In the nFET, the charge carrier is negative and thus electrons flow from the lower potential at the source—typically ground—to the drain. In the pFET, the carriers are positively charged holes, and diffusion occurs from the higher potential at the source to the lower potential at the drain. However, by convention, current is always represented as the flow of positive charge, regardless of the transistor type (Figure 3.6(b)).

The density of charge carriers at each end of the channel depends exponentially on the size of energy barrier (in Figure 3.7, ϕ_S for the source and ϕ_D for the drain). The transistor is fabricated with an initial energy barrier between the souce/drain and the channel; the size of the barrier is modulated by the voltage difference between the channel and the source/drain. For an nFET, increasing the voltage at the source/drain linearly increases the size of the barrier. Since $V_D > V_S$ during transistor operation, $\phi_S < \phi_D$; thus, the density of the charge carrier is greater at the source. Increasing the gate voltage (e.g., from V_G to V_{G1} in Figure 3.7) lowers the barrier at both ends, since the gate voltage influences the surface potential of the channel.

The current in the transistor is proportional to the density gradient along the channel, from source to drain. Since the density of carriers is exponentially related to the energy barrier and the energy barrier is linearly related to the terminal voltages[3],

[2]An n-type region is an area of doped silicon where the primary charge carrier is negatively charged electrons. Conversely, the primary charge carriers in a p-type region are positively charged holes.

[3]For a more detailed description of transistor physics, see [96].

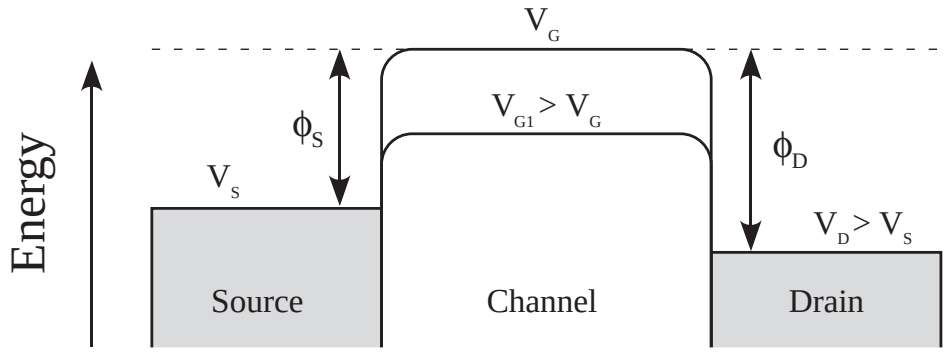

Figure 3.7: Energy Diagram of a Transistor

This diagram shows the energy of the negative charge carrier (electrons) within an nFET. The vertical axis represents energy, while the horizontal axis (not shown) represents the location within the transistor. ϕ_S and ϕ_D represent the energy barrier for electons at the source and drain respectively. The voltages are the terminal voltages, designated by their subscripts. During transistor operation, $V_D > V_S$, and thus $\phi_S < \phi_D$. V_{G1} represents another scenario with a higher gate voltage. Adapted from [96].

the relationship between the channel current and its terminal voltages for an nFET is defined by

$$I_{ds} = I_{ds0}\, e^{\kappa \frac{V_{GB}}{U_T}} \left(e^{-\frac{V_{SB}}{U_T}} - e^{-\frac{V_{DB}}{U_T}} \right), \tag{3.17}$$

where κ describes the relationship between the gate voltage and the channel surface potential, U_T is called the thermal voltage[4], typically 25.4mV at room temperature,

[4]NOTE: For clarity, all transistor voltages from hereon are assumed to be in units of U_T.

and I_{ds0} is the base diffusion current down the concentration gradient at the junction between the source (drain) and body. This relationship also applies for pFETs, except the signs of all the terminal voltages are reversed, due to the opposite sign in the charge carriers.

The channel current can be divided into two components: a source (forward) current and a drain (reverse) current. For large differences between the drain and source voltages (i.e., $> 4\ U_T$), the reverse current is considered negligible, and the transistor is said to be in *saturation*. In this regime, the channel current depends only on the gate and the source. For drain voltages less than $4\ U_T$ from the source, the reverse current is no longer negligible: It decreases the channel current. In this regime (called *ohmic*), the transistor acts like a nonlinear conductor: The gate voltage defines the conductance and the channel current is proportional to the difference between two terminal quantities—in this case a nonlinear function of the terminal voltages (as opposed to the voltages themselves). If the drain and source voltages are equal, then the channel current is zero.

All the terminal voltages—V_{GB}, V_{SB} and V_{DB}—are referenced to the bulk of the transistor (indicated by the subscript 'B'). More often than not, the bulk terminal is connected to one of the rails (Gnd and V_{dd} for nFETs and pFETs, respectively). However, the bulk can also be used as a separate means to control the channel current; for this reason, it is often called the *back gate*. I isolate the dependence of the channel current on the bulk by changing the reference of all the voltages in Equation 3.17 to Gnd (the actual reference voltage is arbitrary).

$$
\begin{aligned}
\mathrm{I_{ds}} &= \mathrm{I_{ds0}}\, \mathrm{e}^{\kappa \mathrm{V_{GB}}} \left(\mathrm{e}^{-\mathrm{V_{SB}}} - \mathrm{e}^{-\mathrm{V_{DB}}} \right) \\
&= \mathrm{I_{ds0}}\, \mathrm{e}^{\kappa (\mathrm{V_G} - \mathrm{V_B})} \left(\mathrm{e}^{-(\mathrm{V_S} - \mathrm{V_B})} - \mathrm{e}^{-(\mathrm{V_D} - \mathrm{V_B})} \right) \\
&= \mathrm{I_{ds0}}\, \mathrm{e}^{\kappa \mathrm{V_G}} \left(\mathrm{e}^{-\mathrm{V_S}} - \mathrm{e}^{-\mathrm{V_D}} \right) \mathrm{e}^{(1-\kappa)\mathrm{V_B}}
\end{aligned} \tag{3.18}
$$

Since κ is typically closer to unity than to zero, the back gate provides a weaker means to control the transistor current.

Appendix A introduces a few circuits commonly used in analog transistor design. These circuits form various components in my model, which is described later in this chapter.

3.2.2 Neuromorphic Models

Many previous neuromorphic models focus on mimicking the synaptic wiring within neural circuits, concentrating on the functional role of a network while ignoring many of the rich dynamics due to voltage dependent conductances within a cell[62, 43, 55, 80]. In their designs, neuromorphic engineers must choose between complexity of their neuron model versus the size of the population: for a fixed area of silicon die, larger circuits—which require more area—translate to fewer instances of the circuit. With a focus on network dynamics, the importance leans heavily towards the number of cells versus the complexity of the neuron.

For essential voltage-dependent channels, such as those involved in action potential generation, the engineer uses an abstraction of the channel, implementing the

important functional consequences of the channel as opposed to the precise dynamics of activation and inactivation. For Na^+ spikes, once the membrane voltage crosses a threshold, positive feedback—either current from an inverter circuit[155, 18, 63] or by capacitive-coupling to a digital signal[96, 10, 62, 61, 80]—generates the rising phase of the action potential. Shortly thereafter, a K^+-like current resets the membrane voltage to subthreshold levels, ending the spike. Often, the spiking mechanism of the neuron is the interface between the analog circuits within the cell and the digital circuits that send the action potentials out of the chip[10, 11].

One channel frequently found within neuromorphic models is the Ca^{++}-dependent K^+ channel[10, 61, 55, 80], due to its simplicity in implementation. The output of the channel depends on a representation of internal calcium levels. As such, as few as three transistors—one for channel current, one for calcium uptake and one for calcium entry into the cell—and a capacitor are sufficient for its implementation[61].

Like many computational models, neuromorphic models that do implement voltage-dependent channels use the empirical form of the Hodgkin-Huxley models; that is, the silicon circuit explicitly models the steady-state and time constant equations for HH variables (see Section 3.1.1). One of the first silicon neuron models was of a single cell, complete with a number of common neuron conductances [85]: the Na^+ and the delayed-rectifier K^+ channels involved in action potential generation, a subthreshold-activated K^+ channel (I_A), and a Ca^{++}-dependent K^+ channel (I_{AHP}). The first three channels are voltage-dependent, and rather than simplify the dynamics (as described for the action potential channels above), Mahowald and Douglas implemented the dynamics of activation and inactivation for each through the use of HH variables. Since both the Na^+ and the low-threshold K^+ channel had activation and inactivation components, they used the same circuit for both, but adjusted the channel

operation—to match biological time scales and voltage dependence of each variable—through voltage biases. In doing so, they demonstrated they could represent a wide range of voltage-dependent channels (both with and without inactivation) through modular design. However, their design possessed a number of areas of improvement.

First, the implementation of the HH variable was incorrect. A low-pass filter of the membrane potential introduced the temporal dynamics of the variable, the output of which passed through a *differential pair*, a circuit that outputs a sigmoid in current with respect to an input voltage. This, however, is the reverse of the Hodgkin-Huxley implementation, where a sigmoid function is the *input* to a low-pass filter (Equation 3.3). The resulting dynamics of their circuit to step changes in the membrane voltage follow more of a sigmoidal path, as opposed to exponential. It could be argued, however, that the sigmoidal path represented the delay typically associated with (for example) multiple independent activation variables.

Second, inactivation of a channel is achieved through current *subtraction* from the activation component. This is an inefficient use of energy: the maximum power occurs when the channel is *inactivated*. A product of variables—as opposed to a subtraction—would reach the maximum power only during channel conduction, a situation that would occur much less often given the channel is open only during activation and before inactivation. Additionally, using current subtraction makes the design more susceptible to problems with *mismatch*[5]. Current subtraction requires the inactivation current to be at least as large as the activation current; any variance in the currents may result in a membrane current that does not fully inactivate.

Finally, their model does not account for the membrane voltage dependence of

[5] *Mismatch* is another term for the variance in current between identically-sized transistors on a single chip.

the time constant for *any* of the gating particles; rather, the time constant is fixed over all membrane voltages. This can be a problem for some HH variables like the inactivation variable of I_T, the dynamics of which (deinactivation versus inactivation) depend strongly on the changing time constant. Control of their time constants is through a voltage bias; thus, it is technically possible to implement this dependence through additional circuitry that modulates this voltage appropriately.

Recently, Simoni et al.[128] sought to improve on these conductance models and addressed many of these very issues. Like the previous model, they used the empirical Hodgkin-Huxley models as the basis for their circuits, and used circuit modules that implemented the temporal dynamics and the steady-state function independently. Unlike the model of Mahowald and Douglas, however, the membrane voltage first passed through a sigmoid circuit for the steady-state equation, and then a low-pass filter for the temporal dynamics of the variable. This is more in line with the Hodgkin-Huxley model (Equation 3.3). As another improvement, the channel model consisted of the product of gating particles, rather than a subtraction.

One area where their design did not improve upon the model from Mahowald and Douglas is the membrane voltage dependence of the time constant for the HH variables. Simoni's model also controls the time constant through a voltage bias, and thus it is possible to add additional circuitry to implement this dependence. However, like all neuromorphic engineers, they chose to limit the size of their circuits, and thus keep the complexity down[128]. Presumably, they would include this dependence if the model deems it necessary, but at the expense of circuit size.

3.2.3 Choosing a Model

Like previous circuit designers, I am faced with the decision between model accuracy (complexity) and number of neurons on the chip. The most important feature of the T channel is the deinactivation that occurs much slower than inactivation (Figure 3.1).

One of the simplest models presented of the T channel reduces the dynamics of I_T around a defined threshold (V_h) [130]. Activation does not possess any temporal dynamics; instead, a Heaviside function at V_h defines its operation. Inactivation is also nonlinear around this threshold, with deinactivation (i.e., the inactivation variable $h \rightarrow 1$) occuring below V_h at a time constant of 100ms, while inactivation (i.e., $h \rightarrow 0$) occurring at a time constant of 20ms. This simple model reproduces the temporal frequency response of geniculate cells in the burst and tonic modes[130, 100]. However, there are a number of concerns that eliminate its use in my design. First, without the activation dynamics, the possibility of burst delay is eliminated (see Figure 3.3(a), [157]). Second, the use of a Heaviside for the inactivation allows for only a continuous deinactivation through time, but not in the level of hyperpolarization (Figure 3.3(b)). Finally, using the same threshold for activation and inactivation (i.e. V_h) eliminates the possibility of inactivation of the channel before activation[130].

The neuromorphic models discussed in the previous subsection implement the empirical form of the HH variable, like many computational models. Their approaches are very similar: they both use circuit building blocks to implement the various components of each variable (i.e. the steady-state function and the temporal dynamics). However, this modular construction increases the size the circuit. A more efficient approach is to integrate the implementation of both functions into a single circuit.

The inspiration for the design is the linear thermodynamic models discussed previously (Section 3.1.2). There is a similarity between the state transition rates of the thermodynamic model and the channel current within a transistor: they both rely on particles overcoming an energy barrier. As such, the exponential dependence of the transition rate on the free energy barrier is easy to model in silicon given the exponential dependence of the transistor current on the gate voltage (Equation 3.17). The analogy is not perfect: The transistor itself cannot represent state transitions in both directions. Thus, multiple transistors are necessary. However, because of this similarity, a more efficient design can be created by modelling these transition rates. Now, rather than implementing the steady-state and time constant functions directly, these functions are implemented indirectly through modelling of the transition rates.

Though the linear model was not a good match for the data (as compared to the nonlinear models) (Figure 3.5), the model was able to capture the membrane voltage dependence of both the steady-state and the time constant. One issue with the linear model was the time constant that approached zero at depolarized membrane voltages. This is easily accounted for by the inclusion of a saturation for the transition rate at the depolarized voltages[153]. This is the starting point for the neuromorphic model.

3.3 HH Variable Circuit Design

The neuromorphic model of a HH variable begins with the integration of current on a capacitor C_u to obtain a voltage u_V. That is,

$$C_u \frac{du_V}{dt} = I_{in}(V_m) \tag{3.19}$$

I define the HH variable $u = \mathrm{e}^{\mathrm{a\,u_V - b}}$, where a and b, for the moment, are constants, and $\mathrm{u_V}$ is the capacitor voltage corresponding to u. This form should be obvious for the HH variable—at least for those familiar with neuromorphic methods—since all the terminal voltages of the transistor affect the current exponentially. This also means the voltage across the capacitor is a *log-domain* representation of the Hodgkin-Huxley variable. The constant a (in units of V^{-1}) defines the exponential relationship between u and $\mathrm{u_V}$. The constant b is used as a normalization factor. To simplify the following derivation, I initially assume it is not needed (i.e., b = 0). Rewriting Equation 3.19 in terms of u:

$$\frac{\mathrm{d}u}{\mathrm{dt}} = \frac{1}{\mathrm{Q_u}}\, u\, \mathrm{I_{in}}\left(\mathrm{V_m}\right), \tag{3.20}$$

where $\mathrm{Q_u} = \mathrm{C_u}\,\mathrm{U_T}/\mathrm{a}$ is the amount of charge required to *e-fold* the variable u. To realize the form of Equation 3.3, I define the input current as

$$\mathrm{I_{in}}\left(\mathrm{V_m}\right) = \frac{1}{u}\,\mathrm{I_A}\left(\mathrm{V_m}\right) - \left(\,\mathrm{I_A}\left(\mathrm{V_m}\right) + \mathrm{I_B}\left(\mathrm{V_m}\right)\,\right). \tag{3.21}$$

Substituting into Equation 3.20:

$$\begin{aligned}\frac{\mathrm{d}u}{\mathrm{dt}} &= \frac{1}{\mathrm{Q_u}}\left(\mathrm{I_A}\left(\mathrm{V_m}\right) - u\left(\mathrm{I_A}\left(\mathrm{V_m}\right) + \mathrm{I_B}\left(\mathrm{V_m}\right)\right)\right) \\ &= \frac{\mathrm{I_A}\left(\mathrm{V_m}\right)}{\mathrm{Q_u}}\left(1-u\right) - \frac{\mathrm{I_B}\left(\mathrm{V_m}\right)}{\mathrm{Q_u}}\,u \end{aligned} \tag{3.22}$$

In this form, it is clear from Equation 3.2 that $\alpha\left(\mathrm{V_m}\right) = \mathrm{I_A}\left(\mathrm{V_m}\right)/\mathrm{Q_u}$ and $\beta\left(\mathrm{V_m}\right) = \mathrm{I_B}\left(\mathrm{V_m}\right)/\mathrm{Q_u}$. Rearranging

$$\begin{aligned}\frac{\mathrm{d}u}{\mathrm{dt}} &= -\frac{\mathrm{I_A}\left(\mathrm{V_m}\right) + \mathrm{I_B}\left(\mathrm{V_m}\right)}{\mathrm{Q_u}}\left(u - \frac{\mathrm{I_A}\left(\mathrm{V_m}\right)}{\mathrm{I_A}\left(\mathrm{V_m}\right) + \mathrm{I_B}\left(\mathrm{V_m}\right)}\right) \\ &= -\frac{1}{\tau_{\mathrm{u}}\left(\mathrm{V_m}\right)}\left(u - \mathrm{u}_\infty\left(\mathrm{V_m}\right)\right).\end{aligned}$$

The problem has now been reduced to designing the functions of $\mathrm{I_A}\left(\mathrm{V_m}\right)$ and $\mathrm{I_B}\left(\mathrm{V_m}\right)$ such that $\tau_{\mathrm{u}}\left(\mathrm{V_m}\right)$ and $\mathrm{u}_\infty\left(\mathrm{V_m}\right)$ match those of the HH variable being modelled.

3.4 Silicon T Channel Model

Figure 3.8 shows a block diagram of my T channel model. In the following sections, I use the variable $\mathrm{I_T}$ to represent the output current in transistor P2, not necessarily the *channel current*. This distinction is important: in my design $\mathrm{I_T}$ represents the product of the HH variables with either the maximum channel conductance (Equation 3.3), maximum channel permeability (Equation 3.7) or even the maximum channel current. Which maximum parameter $\mathrm{I_T}$ represents depends largely on the neuron

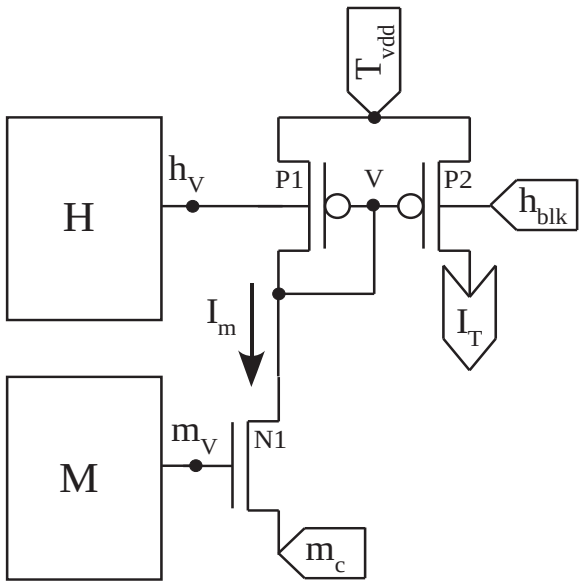

Figure 3.8: T Channel Model

The current from transistor N1 represents the activation of the output current I_T: $I_m = m^\kappa \ \bar{I}_T$. The bulk of transistor P1 implements the inactivation variable h by reducing the gain in the mirror. See text for details.

model; for this chapter, the representation does not matter.

Transistor N1 acts as I_T activation: upon membrane depolarization the transistor 'activates', passing current through a current mirror (see Appendix A.1) and into the neuron. The voltage h_V at the bulk node of transistor P1 controls the level of channel inactivation. When $h_V = h_{blk}$ (the bulk voltage on transistor P2), the mirror acts with unity gain. Lowering h_V with respect to h_{blk} reduces the gate voltage V necessary for the diode-connected transistor P1 to source the activation current. This effectively reduces the gain of the mirror from unity; by further lowering h_V, the output current can be fully inactivated.

To derive an expression for I_T, I begin with Equation A.1—which describes the gain of a current mirror due to differences in bulk voltages—and expand the terms into m_V and h_V:

$$\begin{aligned} I_T &= I_m \, e^{-(1-\kappa)(h_{blk}-h_V)} \\ &= I_{ds0} \, e^{\kappa \, m_V - m_C} \, e^{-(1-\kappa)(h_{blk}-h_V)} \end{aligned}$$

By defining the activation variable $m = e^{m_V - m_H}$ and the inactivation variable $h = e^{-(1-\kappa)(h_{blk}-h_V)}$, the above expression becomes

$$I_T = m^\kappa \, h \, \bar{I}_T, \tag{3.23}$$

where $\bar{I}_T = I_{ds0} \, e^{\kappa \, m_H - m_C}$. In this form, the activation and inactivation variables generate I_T through the modulation of a maximum I_T current ($\bar{I}_T$).

What should immediately stand out from Equation 3.23 is the exponent on the activation variable. Computational models of I_T (see Section 3.1.1) typically use an exponent of two for m, a representation in the HH model of two gating particles. However, for my silicon implementation, to simplify the circuit, I have chosen to use an exponent slightly less than one ($\kappa \approx 0.8$). This difference impacts the dynamics of activation and deactivation—not to be confused with *deinactivation*—of the channel.

First, an exponent greater than one on the HH variable introduces a delay in the

activation (in the case of I_T) of a variable; that is, there is a sigmoid-like rise in the activation of the variable, as opposed to an exponential rise. So while I ignore this delay (by implementing an exponent less than one), I can slow down my activation to account for this.

Also, any exponent on a HH variable other than one introduces an asymmetry in the *perceived* time constants[6] of a rising versus a falling variable. In the two variable case (i.e., an exponent of two), the perceived time constant for activation is larger than for deactivation. The reason is quite simple: for variables less than one, which is true for all HH variables, applying an exponent greater than one moves the variable *away* from unity. This accounts for the perception of a slower rise but a faster decay. For exponents less than one, the converse is true: the perceived time constant during activation is *faster* than during deactivation (a good example of this is seen Figure 2-16 in [51]).

Thus, depending on the circuit parameters, the dynamics of activation for my model will either open too fast (if I try to match the deactivation), close too slow (if I match the activation) or both (if I try to minimize the error). I do not expect this simplification to handicap the model, as the slower deactivation is largely overshadowed by the *even slower* deinactivation. Previous studies[130, 12] have completely ignored activation dynamics by using a Heaviside function as an activation threshold, and were still able to reproduce some responses of real cells[130]. Higher order Hodgkin-Huxley variables are possible in transistor design, but the decision often comes down to complexity versus area on a chip. In this case, the simpler design seemed more appropriate as the important dynamics of I_T seem to rely more on the inactivation

[6]The *perceived time constant* can be thought of as the time constant calculated by a fit of the rising or falling product (e.g., m^2) to a single exponential.

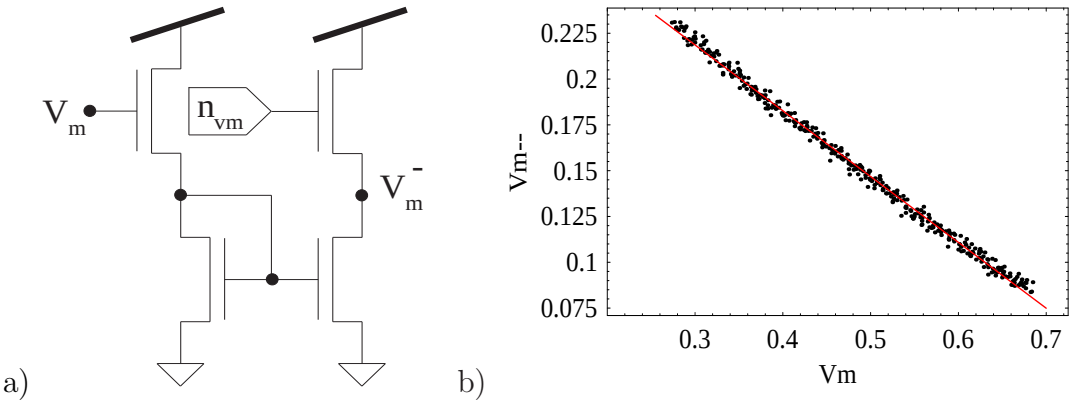

Figure 3.9: V_m^- vs. V_m

(a) Circuit for V_m^- generation. (b) Chip data showing V_m^- versus V_m. The red line shows the fit using Equation 3.25, with extracted parameters of $n_{vm} = 0.405$V, $\kappa = 0.806$.

variable.

3.4.1 V_m vs. V_m^-

I introduce an *inverse membrane voltage* V_m^- to facilitate the modeling of dynamics at hyperpolarized levels. The transistor is a monotonic transconductance: The output current increases exponentially with the gate voltage. This, then, captures channel dynamics at depolarized membrane voltages. However, for hyperpolarization dynamics, such as deinactivation, I need a current that increases as the membrane voltage *decreases*. This is easily accomplished by generating a voltage that decreases with increasing V_m (Figure 3.9(a)). The relationship between V_m and V_m^- can be described by

$$V_m^- = U_T \log\left[1 + \exp\left[\frac{\kappa}{U_T}\left(n_{vm} - \frac{\kappa}{\kappa+1}V_m\right)\right]\right] \tag{3.24}$$

where κ and U_T are transistor parameters (see Section 3.2.1) and n_{vm} is an external voltage bias. At small V_m, V_m^- approaches the gate voltage n_{vm}. As V_m increases, the current output of the mirror subsequently increases, decreasing V_m^-.

The equation above is complicated by the fact that at higher V_m, the mirror output transistor begins to move out of saturation as the drain (V_m^-) approaches the source. However, I can simplify this equation by assuming all transistors stay in saturation, at least for the relevant range of operation:

$$V_m^- = \kappa\left(n_{vm} - \frac{\kappa}{\kappa+1}V_m\right) \tag{3.25}$$

Thus V_m^- is a linear decreasing function of V_m. Figure 3.9(b) plots data from a silicon chip and the fit to Equation 3.25. I chose the slope for this relationship to account for the asymmetry in the slopes around the peak of the inactivation time constant (Figure 3.1). The time constant of a HH variable is generated by the inverse of a current (Section 3.3); a slope less than unity ensures the current will increase slower as the voltage decreases from the peak (and thus the time constant will decrease slower) than when the voltage increases.

Of note, $V_m = V_m^-$ when

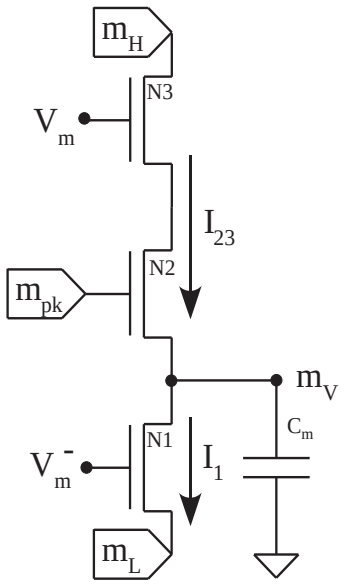

Figure 3.10: Activation Variable m Circuit

The voltage m_V is the *log-domain* representation of the activation variable m. V_m^- is inversely related to V_m (Equation 3.25). m_H, m_L, and m_{PK} are adjustable voltage parameters. See text for details.

$$V_m = \frac{\kappa + 1}{1 + \kappa + \kappa^2} \kappa \; n_{vm} \tag{3.26}$$

3.4.2 Activation Variable m

Figure 3.10 shows the circuit for the activation variable m. The circuit uses the source of the input transistor N2 to obtain a *log-domain* representation of m with m_V. Assuming transistor N1 remains in saturation, the sum of the currents integrating on the capacitor C_m is

$$C_m \frac{dm_V}{dt} = I_{23}\left(e^{-m_V} - e^{-m_H}\right) - I_m^- \, e^{-m_L}$$

Substituting $m = e^{m_V - m_H}$,

$$\begin{aligned} Q_m \, \frac{1}{m} \, \frac{dm}{dt} &= I_{23}\left(\frac{1}{m}\, e^{-m_H} - e^{-m_H}\right) - I_m^- \, e^{-m_L} \\ \frac{dm}{dt} &= I_{23} \, \frac{e^{-m_H}}{Q_m}\,(1-m) - I_m^- \, \frac{e^{-m_L}}{Q_m} \, m \\ &= \frac{I_m \, I_{pk}}{I_m + I_{pk}} \, \frac{e^{-m_H}}{Q_m}\,(1-m) - I_m^- \, \frac{e^{-m_L}}{Q_m} \, m \end{aligned}$$

where $I_{23} = \frac{I_m \, I_{pk}}{I_m + I_{pk}}$ is the current through the two series nFETs (see Equation A.3). From here it is easy to see the rate constants between the open and closed states (Equation 3.2). Thus, to calculate the steady-state and time constant equations:

$$\begin{aligned} m_\infty(V_m) &= \frac{\alpha(V_m)}{\alpha(V_m) + \beta(V_m)} \\ &= \frac{\frac{I_m \, I_{pk}}{I_m + I_{pk}} \, e^{-m_H}}{\frac{I_m \, I_{pk}}{I_m + I_{pk}} \, e^{-m_H} + I_m^- \, e^{-m_L}} \\ &= \frac{1}{1 + \left(e^{-\kappa \, m_{PK}} + e^{-\kappa \, V_m}\right) e^{\kappa \, V_m^-} \, e^{m_H - m_L}} \end{aligned} \tag{3.27}$$

In computational models, $m_\infty(V_m)$ is a sigmoid with a center voltage V_m^{mid}. I can realize this form with the above equation by restricting $\kappa \, m_{PK} > (m_H - m_L + 4\,U_T)$,

or, in simpler terms, by stating that by the time the exponential term with m_{PK} becomes significant (with respect to $\exp[-\kappa V_m]$), the sigmoid already has reached its maximum. Thus, assuming this restriction and substituting Equation 3.25 for V_m^-, the above equation reduces as follows:

$$\begin{aligned} m_\infty(V_m) &= \frac{1}{1+\left(e^{-\kappa\ m_{PK}}+e^{-\kappa\ V_m}\right)\ e^{\kappa\ V_m^- + m_H - m_L}} \\ &= \frac{1}{1+\exp\left[-\kappa\ V_m - \frac{\kappa^3}{\kappa+1}V_m + \kappa^2\, n_{vm} + m_H - m_L\right]} \\ &= \frac{1}{1+\exp\left[-\kappa\ \left(\frac{\kappa^2+\kappa+1}{\kappa+1}\right)V_m + (\kappa^2\, n_{vm} + m_H - m_L)\right]} \\ &= \frac{1}{1+\exp\left[-\frac{V_m - V_m^{mid}}{V_m^*}\right]} \end{aligned} \tag{3.28}$$

where

$$\begin{aligned} V_m^{mid} &= \frac{1}{\kappa}\frac{\kappa+1}{\kappa^2+\kappa+1}\left(\kappa^2\, n_{vm} + m_H - m_L\right) \\ V_m^* &= \frac{1}{\kappa}\frac{\kappa+1}{\kappa^2+\kappa+1}U_T. \end{aligned}$$

Like n_{vm} (Section 3.4.1), m_H and m_L are both external voltage biases. The first term in V_m^{mid} is the point where $V_m = V_m^-$ (Equation 3.26); the midpoint is shifted from this point through the difference $(m_H - m_L)$. For the time constant:

$$
\begin{aligned}
\tau_{\mathrm{m}}\left(\mathrm{V_m}\right) &= \frac{1}{\alpha\left(\mathrm{V_m}\right)+\beta\left(\mathrm{V_m}\right)} \\
&= \frac{\mathrm{Q_m}}{\frac{\mathrm{I_m\ I_{pk}}}{\mathrm{I_m+I_{pk}}}\ \mathrm{e}^{-\mathrm{m_H}}+\mathrm{I_m^-}\ \mathrm{e}^{-\mathrm{m_L}}} \\
&= \frac{1}{\frac{\mathrm{e}^{\kappa\ \mathrm{V_m}}}{\mathrm{e}^{\kappa\ \mathrm{V_m}}+\mathrm{e}^{\kappa\ \mathrm{m_{PK}}}}+\mathrm{e}^{\kappa\ \mathrm{V_m^-}}\ \mathrm{e}^{\mathrm{m_H}-\mathrm{m_L}-\kappa\ \mathrm{m_{PK}}}}\frac{\mathrm{Q_m}\ \mathrm{e}^{\mathrm{m_H}}}{\mathrm{I_{pk}}} \\
&= \frac{1}{\frac{\mathrm{e}^{\kappa\ \mathrm{V_m}}}{\mathrm{e}^{\kappa\ \mathrm{V_m}}+\mathrm{e}^{\kappa\ \mathrm{m_{PK}}}}+\mathrm{e}^{\kappa\ \mathrm{V_m^-}}\ \mathrm{e}^{\mathrm{m_H}-\mathrm{m_L}-\kappa\ \mathrm{m_{PK}}}}\ \tau_{\mathrm{msat}}
\end{aligned}
$$

where $\mathrm{Q_m}=\mathrm{C_m U_T}$, and $\tau_{\mathrm{msat}}=\mathrm{Q_m}\,\mathrm{e}^{\mathrm{m_H}}/\mathrm{I_{pk}}$ represents the minimum time constant at depolarized membrane potentials. To simplify τ_{m}, I first rewrite the above expression as three separate terms:

$$
\begin{aligned}
\frac{\tau_m\left(\mathrm{V_m}\right)}{\tau_{\mathrm{msat}}} &= \frac{\mathrm{e}^{\kappa\ \mathrm{V_m}}+\mathrm{e}^{\kappa\ \mathrm{m_{PK}}}}{\mathrm{e}^{\kappa\ \mathrm{V_m}}+\left(\ \mathrm{e}^{\kappa(\mathrm{V_m}-\mathrm{m_{PK}})}+1\ \right)\ \mathrm{e}^{\kappa\,\mathrm{V_m^-}+\mathrm{m_H}-\mathrm{m_L}}} \\
&= 1+\frac{\mathrm{e}^{\kappa\ \mathrm{m_{PK}}}-\left(\ \mathrm{e}^{\kappa\ (\mathrm{V_m}-\mathrm{m_{PK}})}+1\ \right)\ \mathrm{e}^{\kappa\,\mathrm{V_m^-}+\mathrm{m_H}-\mathrm{m_L}}}{\mathrm{e}^{\kappa\ \mathrm{V_m}}+\left(\ \mathrm{e}^{\kappa\ (\mathrm{V_m}-\mathrm{m_{PK}})}+1\ \right)\ \mathrm{e}^{\kappa\,\mathrm{V_m^-}+\mathrm{m_H}-\mathrm{m_L}}} \\
&= 1+\frac{\mathrm{e}^{\kappa\ \mathrm{m_{PK}}}}{\mathrm{e}^{\kappa\ \mathrm{V_m}}+\left(\ \mathrm{e}^{\kappa\ (\mathrm{V_m}-\mathrm{m_{PK}})}+1\ \right)\ \mathrm{e}^{\kappa\,\mathrm{V_m^-}+\mathrm{m_H}-\mathrm{m_L}}} \\
&\quad -\frac{\left(\ \mathrm{e}^{\kappa(\mathrm{V_m}-\mathrm{m_{PK}})}+1\ \right)\ \mathrm{e}^{\kappa\,\mathrm{V_m^-}+\mathrm{m_H}-\mathrm{m_L}}}{\mathrm{e}^{\kappa\ \mathrm{V_m}}+\left(\ \mathrm{e}^{\kappa(\mathrm{V_m}-\mathrm{m_{PK}})}+1\ \right)\ \mathrm{e}^{\kappa\,\mathrm{V_m^-}+\mathrm{m_H}-\mathrm{m_L}}}
\end{aligned}
$$

The first term dominates at depolarized membrane voltages, as the other two terms become negligible due to the exponential $\mathrm{e}^{\kappa\ \mathrm{V_m}}$ in the denominators. Thus, as $\mathrm{V_m}$ increases, $\tau_{\mathrm{m}} \rightarrow \tau_{\mathrm{msat}}$. The last term becomes significant only at hyperpolarized levels, approaching one as the $\mathrm{V_m}$ drops and effectively reducing the time constant to zero. The second term, with a constant numerator, dominates in the middle voltage

ranges, when the denominator—a sum of two exponentials, one of V_m and the other of V_m^-—is minimized.

I reduce the equation with two simplifications. First, I ignore the last term, simply because the expression does not influence the important aspects of the activation time constant, such as the peak or the time constant at depolarized levels. Without this term, the time constant will reduce to τ_{msat} as V_m drops, as opposed to zero. Second, I use the same assumption as m_∞ ($m_{PK} \gg V_m$) to simplify the second term. This eliminates the expression $\left(e^{\kappa(V_m - m_{PK})} + 1 \right)$ from the denominator. This term only becomes significant at high V_m, but by then the denominator will have reduced the term to zero. Therefore, Equation 3.25 becomes

$$\begin{aligned}
\frac{\tau_m(V_m)}{\tau_{msat}} &\approx 1 + \frac{e^{\kappa\ m_{PK}}}{e^{\kappa\ V_m} + e^{-\kappa\ \left(\frac{\kappa^2}{\kappa+1}\right)V_m} e^{\kappa^2 n_{vm} + m_H - m_L}} \\
\tau_m &\approx \tau_{msat}\left(1 + \frac{1}{e^{\kappa\ (V_m - m_{PK})} + e^{-\kappa\ \left(\frac{\kappa^2}{\kappa+1}\right)V_m} e^{\kappa^2 n_{vm} + m_H - m_L} e^{-\kappa\ m_{PK}}}\right) \\
&= \tau_{msat}\left(1 + \frac{1}{\exp\left(\frac{V_m - V_{1m}}{V_{1m}^*}\right) + \exp\left(-\frac{V_m - V_{2m}}{V_{2m}^*}\right)}\right) \qquad (3.29)
\end{aligned}$$

where

$$\begin{aligned}
V_{1m} &= m_{PK} \\
V_{1m}^* &= U_T/\kappa \\
V_{2m} &= \frac{\kappa + 1}{\kappa^3}\left(\kappa^2 n_{vm} + m_H - m_L - \kappa\ m_{PK}\right) \\
V_{2m}^* &= \frac{\kappa + 1}{\kappa^3} U_T
\end{aligned}$$

m_{PK} is also an external voltage bias, in addition to those mentioned previously. As designed, Equations 3.28 and 3.29 are similar in form to their computational counterparts (Table 3.1). The external adjustable biases are present in the parameters that either scale the time constant (e.g., τ_{msat}) and/or those that shift the voltage dependence of activation (e.g., V_m^{mid}, V_{1m}, V_{2m}). However, not all of the parameters are externally controllable. These parameters—namely the voltage constants V_m^*,V_{1m}^* and V_{2m}^*—rely on the product of thermal voltage U_T and a polynomial function of κ, both physical parameters of the transistor. Since external biases only affect the current in a transistor exponentially, I am limited in my ability to modify the voltage constant in any exponential except by designing circuits that achieve a desired polynomial function of κ. However, once the chip has been fabricated, I can shift or scale the functions but cannot change the basic shape. This, of course, is a drawback with my technique, and requires careful consideration in the design of these circuits.

Intuitively, the circuit function is quite simple. At steady state, the current in all three transistors is equal ($I_{23} = I_1$). Since m_V is the source voltage for I_{23}, m_V adjusts I_{23} to match I_1. As the cell hyperpolarizes and I_1 increases (due to V_m^-), m_V drops to increase I_{23}. Conversely, if the cell depolarizes, I_1 decreases and thus m_V rises. At some point, transistor N3 moves out of saturation and the reverse current (due to the drain voltage m_H) is no longer negligible. In this case, as I_1 proceeds to drop, m_V slows down in its rate of increase, as it no longer reduces I_{23} through the gate-source voltage of N3 but through the reverse current. Eventually, once I_1 is off, $m_V \approx m_H$, and $m \approx 1$ (since I have defined $m = e^{m_V - m_H}$).

I_1 and the reverse component of I_{23} define the shape of the membrane voltage dependence of the activation time constant. Since I_1 is active at hyperpolarized voltages and the reverse component of I_{23} at depolarized levels, the inverse of their

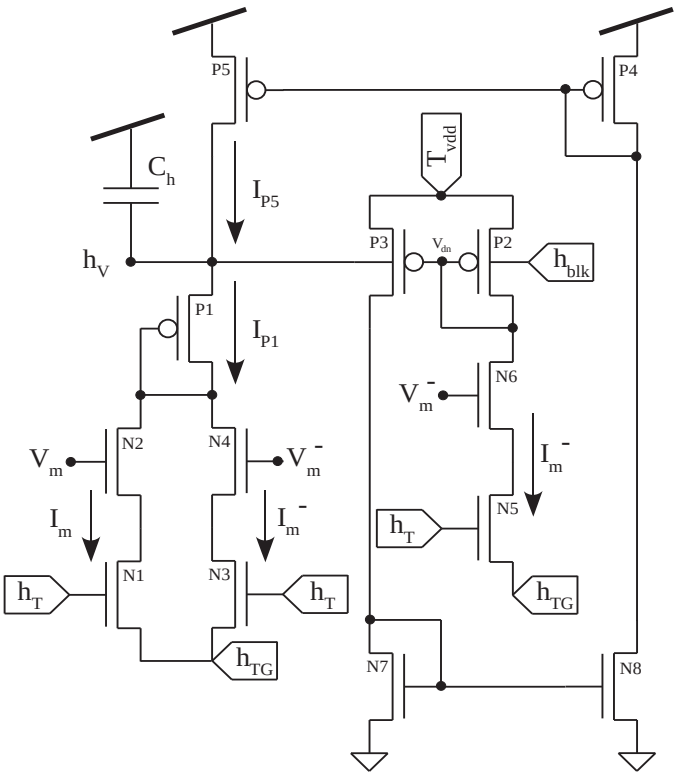

Figure 3.11: Transistor Implementation of Inactivation Variable

The voltage h_V on the capacitor is the log-domain representation of the variable h. As shown in Figure 3.8, h_V uses the bulk node of a pFET to implement inactivation of I_T. See text for details.

sum achieves a bell shape (see Figure 3.1). The gate of transistor N2, m_{PK}, sets the time constant τ_{msat} at depolarized levels by saturating the reverse current. Without N2, τ_m would decrease to zero as V_m increased. With N2, the reverse current becomes proportional to $e^{\kappa\, m_{PK} - m_H}$ when $V_m \gg m_{PK}$.

3.4.3 Inactivation Variable h

Figure 3.11 shows the circuit for the inactivation variable h. Similar to the activation variable, the voltage $\mathrm{h_V}$ is a *log-domain* representation of the variable h, achieved using the bulk node of the pFET. The dynamics of $\mathrm{h_V}$ are described by

$$\mathrm{C_h}\frac{\mathrm{dh_V}}{\mathrm{dt}} = \mathrm{I_{P1}} + \mathrm{I_{P5}}$$

$\mathrm{I_{P1}}$ is simply the sum of two currents, $\mathrm{I_m} + \mathrm{I_m^-}$. $\mathrm{I_{P5}}$ is the output of three series current mirrors. The last two are unity gain mirrors, and so $\mathrm{I_{P5}}$ is completely defined by the output of the first mirror (transistors P2-3). From Equation A.1,

$$\begin{aligned} \mathrm{I_{P5}} &= \mathrm{I_m^-}\ \mathrm{e}^{-(1-\kappa)(\mathrm{h_V}-\mathrm{h_{blk}})} \\ &= \frac{1}{h}\ \mathrm{I_m^-} \end{aligned}$$

where $h = \mathrm{e}^{(1-\kappa)(\mathrm{h_V}-\mathrm{h_{blk}})}$. Therefore, the total input current on the capacitor $\mathrm{C_h}$ is

$$\begin{aligned} \mathrm{C_h}\ \frac{\mathrm{dh_V}}{\mathrm{dt}} &= -\frac{1}{h}\ \mathrm{I_m^-} + \left(\ \mathrm{I_m^-} + \mathrm{I_m}\ \right) \\ \mathrm{Q_h}\ \frac{1}{h}\ \frac{\mathrm{d}h}{\mathrm{dt}} &= -\left(\ \frac{1}{h} - 1\ \right)\mathrm{I_m^-} + \mathrm{I_m} \\ \frac{\mathrm{d}h}{\mathrm{dt}} &= -\frac{\mathrm{I_m^-}}{\mathrm{Q_h}}\ (\ 1-h\ ) + \frac{\mathrm{I_m}}{\mathrm{Q_h}}\ h \end{aligned}$$

where $Q_h = C_h U_T/(1-\kappa)$. Recalling Equation 3.22, I solve for h_∞:

$$\begin{aligned} h_\infty(V_m) &= \frac{I_m^-}{I_m + I_m^-} \\ &= \frac{\frac{e^{\kappa\ V_m^-}}{e^{\kappa\ V_m^-} + e^{\kappa\ h_T}}}{\frac{e^{\kappa\ V_m^-}}{e^{\kappa\ V_m^-} + e^{\kappa\ h_T}} + \frac{e^{\kappa\ V_m}}{e^{\kappa\ V_m} + e^{\kappa\ h_T}}} \\ &= \frac{1}{1 + \frac{1+e^{\kappa\ \left(h_T - V_m^-\right)}}{1+e^{\kappa\ (h_T - V_m)}}} \end{aligned} \tag{3.30}$$

Expanding the expression into two terms:

$$\begin{aligned} h_\infty(V_m) &= \frac{1}{1 + \frac{1+e^{\kappa\ \left(h_T - V_m^-\right)}}{1+e^{\kappa\ (h_T - V_m)}}} \\ &= \frac{1}{2 + e^{\kappa\ (h_T - V_m)} + e^{\kappa\ \left(h_T - V_m^-\right)}} + \frac{e^{\kappa\ (h_T - V_m)}}{2 + e^{\kappa\ (h_T - V_m)} + e^{\kappa\ \left(h_T - V_m^-\right)}} \\ &= \frac{1}{2 + e^{\kappa\ (h_T - V_m)} + e^{\kappa\ \left(h_T - V_m^-\right)}} + \frac{1}{1 + 2\,e^{-\kappa\ (h_T - V_m)} + e^{\kappa\ \left(V_m - V_m^-\right)}} \end{aligned}$$

The first term becomes negligible if I restrict h_T such that $h_T > (V_m + 4\,U_T)$ when $V_m = V_m^-$, ensuring that one of the two exponential terms is always greater than 2. In addition, with this restriction, the middle term in the denominator of the second fraction becomes useless as the last term in the denominator will always be more significant. Thus,

$$
\begin{aligned}
\mathrm{h}_{\infty}\left(\mathrm{V_m}\right) &= \frac{1}{1+\mathrm{e}^{\kappa\ \left(\mathrm{V_m}-\mathrm{V_m^-}\right)}} \\
&= \frac{1}{1+\mathrm{e}^{\kappa\ \left(\frac{1+\kappa+\kappa^2}{\kappa+1}\mathrm{V_m}-\kappa\ \mathrm{n_{vm}}\right)}} \\
&= \frac{1}{1+\exp\left[\frac{\mathrm{V_m}-\mathrm{V_h^{mid}}}{\mathrm{V_h^*}}\right]}
\end{aligned}
\tag{3.31}
$$

where

$$
\begin{aligned}
\mathrm{V_h^{mid}} &= \frac{\kappa\ +1}{\kappa\ \left(\kappa^{\,2}+\kappa\ +1\right)}\ \kappa^{\,2}\ \mathrm{n_{vm}} \\
\mathrm{V_h^*} &= \frac{\kappa\ +1}{\kappa\ \left(1+\kappa\ +\kappa^{\,2}\right)}\ \mathrm{U_T}
\end{aligned}
$$

Note that the midpoint of the sigmoid $\mathrm{V_h^{mid}}$ occurs where $\mathrm{V_m} = \mathrm{V_m^-}$ (Equation 3.26). For the time constant,

$$
\begin{aligned}
\tau_{\mathrm{h}}\left(\mathrm{V_m}\right) &= \frac{\mathrm{Q_h}}{\mathrm{I_m}+\mathrm{I_m^-}} \\
&= \frac{1}{\frac{\mathrm{e}^{\kappa\ \mathrm{V_m^-}}}{\mathrm{e}^{\kappa\ \mathrm{V_m^-}}+\mathrm{e}^{\kappa\ \mathrm{h_T}}}+\frac{\mathrm{e}^{\kappa\ \mathrm{V_m}}}{\mathrm{e}^{\kappa\ \mathrm{V_m}}+\mathrm{e}^{\kappa\ \mathrm{h_T}}}}\ \frac{\mathrm{Q_h}}{\mathrm{I_{ds0}}\ \mathrm{e}^{\kappa\ \mathrm{h_T}}\ \mathrm{e}^{-\mathrm{h_{TG}}}} \\
&= \frac{1}{\frac{\mathrm{e}^{\kappa\ \mathrm{V_m^-}}}{\mathrm{e}^{\kappa\ \mathrm{V_m^-}}+\mathrm{e}^{\kappa\ \mathrm{h_T}}}+\frac{\mathrm{e}^{\kappa\ \mathrm{V_m}}}{\mathrm{e}^{\kappa\ \mathrm{V_m}}+\mathrm{e}^{\kappa\ \mathrm{h_T}}}}\ \tau_{\mathrm{hsat}}
\end{aligned}
$$

where $\tau_{\mathrm{hsat}} = \mathrm{Q_h}\,\mathrm{e}^{\mathrm{h_{TG}}}/\mathrm{I_{ht}}$ represents the base inactivation time constant. Rearranging the expression into the form $(1 + f(\mathrm{V_m}))$,

$$
\begin{aligned}
\frac{\tau_{\mathrm{h}}\left(\mathrm{V_m}\right)}{\tau_{\mathrm{hsat}}} &= \frac{\mathrm{e}^{\kappa\ \left(\mathrm{V_m}+\mathrm{V_m^-}\right)}+\mathrm{e}^{\kappa\ \mathrm{h_T}}\left(\mathrm{e}^{\kappa\ \mathrm{V_m}}+\mathrm{e}^{\kappa\ \mathrm{V_m^-}}\right)+\mathrm{e}^{2\kappa\ \mathrm{h_T}}}{2\mathrm{e}^{\kappa\ \left(\mathrm{V_m}+\mathrm{V_m^-}\right)}+\mathrm{e}^{\kappa\ \mathrm{h_T}}\left(\mathrm{e}^{\kappa\ \mathrm{V_m}}+\mathrm{e}^{\kappa\ \mathrm{V_m^-}}\right)} \\
&= 1+\frac{\mathrm{e}^{2\kappa\ \mathrm{h_T}}-\mathrm{e}^{\kappa\ \left(\mathrm{V_m}+\mathrm{V_m^-}\right)}}{2\mathrm{e}^{\kappa\ \left(\mathrm{V_m}+\mathrm{V_m^-}\right)}+\mathrm{e}^{\kappa\ \mathrm{h_T}}\left(\mathrm{e}^{\kappa\ \mathrm{V_m}}+\mathrm{e}^{\kappa\ \mathrm{V_m^-}}\right)} \\
&= 1+\frac{\mathrm{e}^{2\kappa\ \mathrm{h_T}}}{2\mathrm{e}^{\kappa\ \left(\mathrm{V_m}+\mathrm{V_m^-}\right)}+\mathrm{e}^{\kappa\ \mathrm{h_T}}\left(\mathrm{e}^{\kappa\ \mathrm{V_m}}+\mathrm{e}^{\kappa\ \mathrm{V_m^-}}\right)} \\
&\quad -\frac{\mathrm{e}^{\kappa\ \left(\mathrm{V_m}+\mathrm{V_m^-}\right)}}{2\mathrm{e}^{\kappa\ \left(\mathrm{V_m}+\mathrm{V_m^-}\right)}+\mathrm{e}^{\kappa\ \mathrm{h_T}}\left(\mathrm{e}^{\kappa\ \mathrm{V_m}}+\mathrm{e}^{\kappa\ \mathrm{V_m^-}}\right)} \\
&= 1+\frac{\mathrm{e}^{2\kappa\ \mathrm{h_T}}}{2\mathrm{e}^{\kappa\ \left(\mathrm{V_m}+\mathrm{V_m^-}\right)}+\mathrm{e}^{\kappa\ \mathrm{h_T}}\left(\mathrm{e}^{\kappa\ \mathrm{V_m}}+\mathrm{e}^{\kappa\ \mathrm{V_m^-}}\right)}-\frac{1}{2+\mathrm{e}^{\kappa\ \mathrm{h_T}}\left(\mathrm{e}^{-\kappa\ \mathrm{V_m}}+\mathrm{e}^{-\kappa\ \mathrm{V_m^-}}\right)}
\end{aligned}
$$

By applying the same assumptions as for h_∞, I can eliminate the third term from the above expression as $\mathrm{e}^{\kappa\ \mathrm{h_T}}\left(\mathrm{e}^{-\kappa\ \mathrm{V_m}}+\mathrm{e}^{-\kappa\ \mathrm{V_m^-}}\right) \gg 2$ over all $\mathrm{V_m}$. I can also ignore the first term in the denominator of the first fraction as—also due to the same assumptions—$\mathrm{e}^{\kappa\ \left(\mathrm{V_m}+\mathrm{V_m^-}\right)} \ll \mathrm{e}^{\kappa\ \mathrm{h_T}}\left(\mathrm{e}^{\kappa\ \mathrm{V_m}}+\mathrm{e}^{\kappa\ \mathrm{V_m^-}}\right)$. Thus,

$$
\begin{aligned}
\frac{\tau_{\mathrm{h}}\left(\mathrm{V_m}\right)}{\tau_{\mathrm{hsat}}} &\approx 1+\frac{\mathrm{e}^{2\kappa\ \mathrm{h_T}}}{\mathrm{e}^{\kappa\ \mathrm{h_T}}\left(\mathrm{e}^{\kappa\ \mathrm{V_m}}+\mathrm{e}^{\kappa\ \mathrm{V_m^-}}\right)} \\
&= 1+\frac{1}{\mathrm{e}^{\kappa\ \left(\mathrm{V_m}-\mathrm{h_T}\right)}+\mathrm{e}^{\kappa\ \left(\mathrm{V_m^-}-\mathrm{h_T}\right)}} \\
&= 1+\frac{1}{\mathrm{e}^{\kappa\ \left(\mathrm{V_m}-\mathrm{h_T}\right)}+\mathrm{e}^{\kappa\ \left(\kappa\,\mathrm{n_{vm}}-\frac{\kappa^2}{\kappa+1}\mathrm{V_m}-\mathrm{h_T}\right)}} \\
\therefore \tau_{\mathrm{h}}\left(\mathrm{V_m}\right) &\approx \tau_{\mathrm{hsat}}\left(1+\frac{1}{\exp\left(\frac{\mathrm{V_m}-\mathrm{V_{1h}}}{\mathrm{V_{1h}^*}}\right)+\exp\left(-\frac{\mathrm{V_m}-\mathrm{V_{2h}}}{\mathrm{V_{2h}^*}}\right)}\right) \qquad (3.32)
\end{aligned}
$$

where

$$
\begin{aligned}
\mathrm{V_{1h}} &= \mathrm{h_T} \\
\mathrm{V^*_{1h}} &= \mathrm{U_T}/\kappa \\
\mathrm{V_{2h}} &= \frac{\kappa + 1}{\kappa^2}\left(\kappa\ \mathrm{n_{vm}} - \mathrm{h_T}\right) \\
\mathrm{V^*_{2h}} &= \frac{\kappa + 1}{\kappa^3}\mathrm{U_T}
\end{aligned}
$$

$\mathrm{h_T}$ and $\mathrm{h_{TG}}$ are external voltage biases for inactivation. The HH equations governing h are almost identical in form to those for the activation variable m (Equations 3.28 and 3.29), so much so the parameters listed above seem only to differ in the external bias names. Most of the similarities derive from the fact that both circuits share $\mathrm{V_m^-}$ (see Section 3.4.1). There are a couple of key distinctions, however. The first difference exists between the terms $\mathrm{V_h^{mid}}$ and $\mathrm{V_m^{mid}}$. $\mathrm{V_m^{mid}}$ contains an additional term $(\mathrm{m_H} - \mathrm{m_L})$, used to separate the activation and inactivation steady state curves.

The second difference exists in the time constants τ_{msat} and τ_{hsat}, more specifically the factor $1/(1-\kappa)$. According to Figure 3.1, the time constant for inactivation is roughly 25-50 times larger than that of activation. The simplest solution, increasing the inactivation capacitance $\mathrm{C_h}$, is unreasonable since silicon models are constrained by die area. Another solution involves reducing the magnitude of the current involved in generating the time constant. However, leakage currents within a transistor—an issue that is becoming increasingly problematic with smaller processes—set a floor on how small a current can be generated. My solution involves the use of the back gate of the transistor (Equation 3.18), which, as described in Section 3.2.1, provides a weaker mechanism for affecting the output current. This means the bulk voltage has to change by $\kappa/(1-\kappa)$ more than a gate voltage to affect the current equivalently.

Assuming $\kappa \approx 0.8$, this is equivalent to a capacitance that is approximately five-fold greater.

As in the case of the activation variable, the steady state level of h is controlled by the balance of current on the capacitor. That is, h_V continues to transition until the current through transistor P5 (I_{P5}) matches I_{P1}. Full deinactivation ($h = 1$) occurs when $I_{P5} = I_{P1} = I_m^-$, or when the cell is sufficiently hyperpolarized such that I_m is negligible. As V_m begins to rise, I_{P1} begins to increase and h must drop sufficiently so that at steady state $I_{P5} = I_{P1}$. $h = 0.5$ occurs when $I_{P1} = 2\ I_m^-$, or in other words when $V_m = V_m^-$. Further increases in V_m will continue to drop h, thus inactivating I_T.

Like its activation counterpart, the membrane voltage dependence of the inactivation time constant (τ_h) asymptotes at extreme voltages and peaks in the middle. The components of I_{P1} have been designed such that they each saturate at opposite extremes but never sum to greater than the saturation level, otherwise a trough would exist in place of the peak. Since the gate voltage h_T provides the limit on the current level for each component of I_{P1}, the time constant at hyperpolarized and depolarized levels is proportional to $e^{-(\kappa\ h_T - h_{TG})}$. At the peak in the inactivation time constant curve, if h_T is sufficiently large, I_{P1} depends only on V_m and V_m^-.

3.5 Results

The results presented here were taken from a chip fabricated with TSMC's 0.25μm process. I tested my design using voltage clamp experiments similar to those used in biology. However, in silicon, I have the advantage of studying the dynamics of

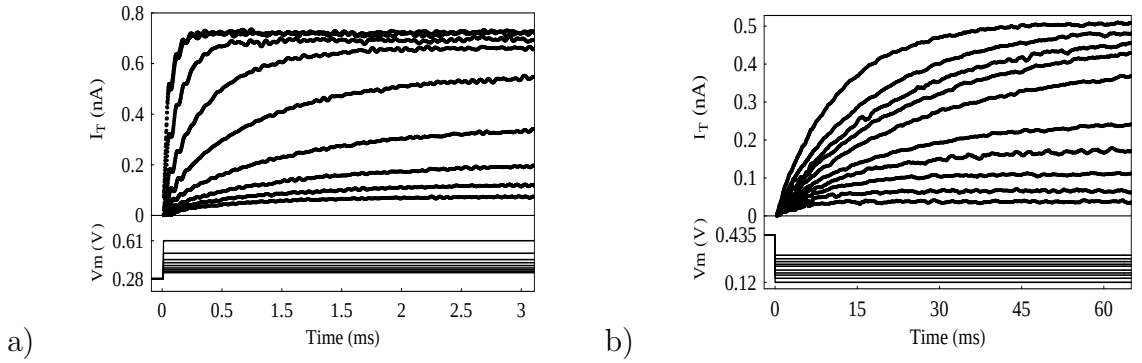

Figure 3.12: Voltage clamp experiments in silicon

For both sets of experiments, the opposite variable is kept fixed (and open) so that I_T reflects the dynamics of the variable under study. The membrane voltage begins in an initial state with the dependent variable closed (i.e., equal to zero) and then stepped to a new voltage (in the direction of variable opening). The time constant is extracted by fitting a rising exponential to the recorded I_T data. The membrane voltage dependencies of the time constant is calculated by sweeping the step size and re-fitting the data. (a) Activation experiments for calculating $\tau_m(V_m)$. The cell begins in a state with I_T deactivated, and the membrane voltage is stepped to more depolarized levels. (b) Inactivation experiments for calculating $\tau_h(V_m)$. The cell begins in a state with I_T inactivated, and the membrane voltage is stepped down to more hyperpolarized levels.

activation and inactivation independently by fixing one and measuring the other, as I_T becomes directly proportional to the independent variable (Equation 3.23).

Figure 3.12 plots some of the I_T responses due to activation (Figure 3.12(a)) and inactivation (Figure 3.12(b)) to steps in the membrane voltage. These responses are used to calculate the membrane voltage dependence of the time constant for each HH variable. The membrane voltage dependence of the steady-state levels is calculated

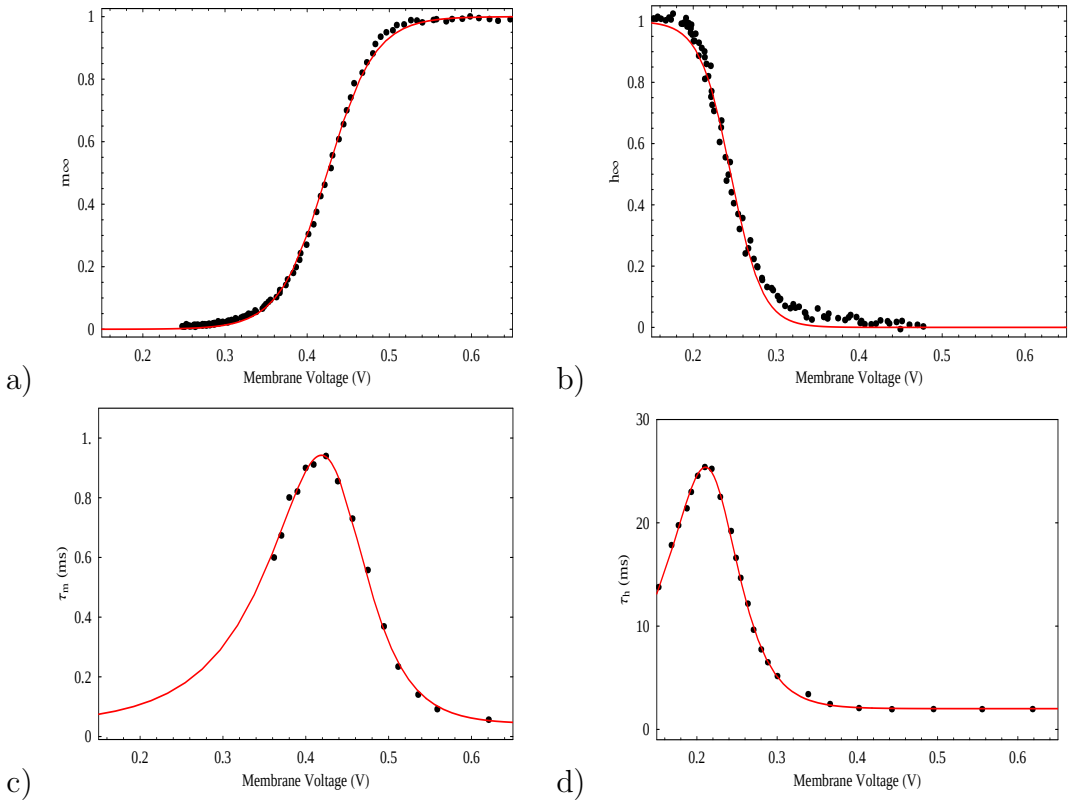

Figure 3.13: HH Variable Functions

Top and bottom rows show the steady state level and time constant curves respectively for activation (left) and inactivation (right). The steady state data is captured by slowly sweeping the membrane voltage and recording I_T directly. The time constant is measured through steps in the membrane voltage (Figure 3.12). The red curve in each plot are the fits of Equations 3.28 and 3.29 (for activation) and Equations 3.31 and 3.32 (for inactivation) to the measured data.

directly by sweeping V_m continuously and recording I_T. Figure 3.13 plots all of these curves for activation and inactivation. The red curve in each plot is the fit of my analytical solutions—Equations 3.28 and 3.29 for activation and Equations 3.31 and 3.32 for inactivation—to the collected data. The analytical solutions fit very nicely with the actual performance of my circuit. This is not surprising, but the question remains: how does my model compare with the computational models?

The most obvious difference is the scale of the time constants. One of the issues in subthreshold transistor design is the existence of leakage currents that set a floor on the level of circuit currents. For proper dynamics, current levels within a transistor must be significantly larger than any intrinsic leakage current. Though I am unable to measure the leakage currents explicitly, I can see their effects through whether or not my circuits are operating correctly. Thus, the range of operation can be determined by scaling the current levels within my transistors.

For the inactivation variable, the current levels are scaled using the bias h_{TG}. This bias is the source for all of the transistors (N1, N3 and N5 in Figure 3.11) involved in generating h. The effect of varying h_{TG}—and thus the magnitude of all the currents—is demonstrated in Figure 3.14. For sufficiently low h_{TG} (i.e., large currents within the circuit), the behavior of the circuit is normal: There is an exponential approach of the inactivation variable to the steady state level. However, as h_{TG} rises—reducing current levels—there is a dramatic change in both the shape of the deinactivation and the steady state level. At its most extreme, the currents in the rest of the circuit are negligible compared to the leak, and the circuit malfunctions. Figure 3.14(b) shows a numerical solution to the inactivation circuit with a 'leak transistor' parallel to transistor P5 (Figure 3.11). The solutions are similar to the measured data in Figure 3.14(a), suggesting the leak acts through transistor P5, but could be due to

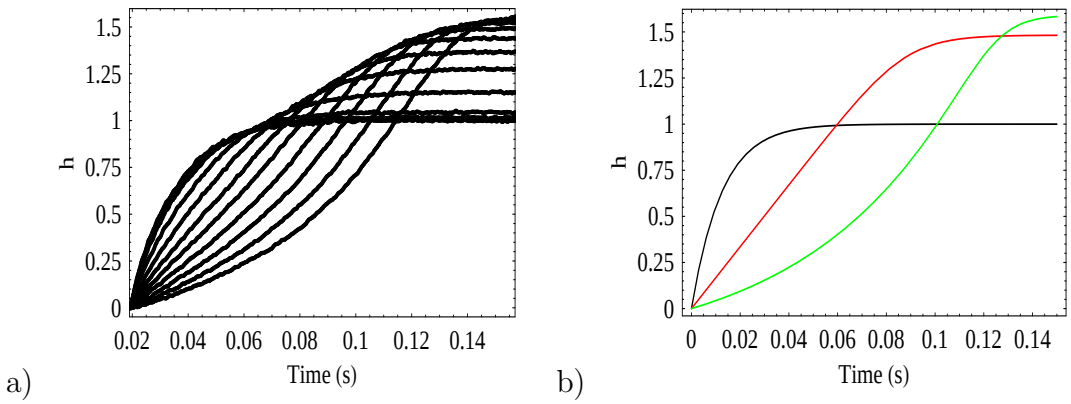

Figure 3.14: Leakage effects on the Inactivation Dynamics

(a) Measured deinactivation of I_T to a step in the membrane voltage for different current levels set by h_{TG}. (b) Numerical solution to the inactivation circuit that assumes the leak acts as a transistor current source parallel to transistor P5. Three conditions are plotted: 1) current levels are larger than the leakage current (black); 2) current levels are roughly of the same magnitude as leakage current (red); 3) current levels are low compared to the leakage current (green).

the leakage in any one of the transistors in the series of current mirrors. During the leakage dominated case in Figure 3.14, h rises exponentially as the voltage h_V now changes at a constant rate proportional to the leak through I_{P5}, rather than $1/h$ I_m^- during proper function. At steady state, h rests at levels larger than one because now h_V settles at a voltage that balances the current in I_{P1} and the leakage current. Since the leak is larger than I_{P1}, h_V must rise sufficiently to move the 'leak transistor' out of saturation and into the ohmic region, which causes $h > 1$.

To ensure proper function, it is important that h_{TG} is set sufficiently low such that the leak current remains sufficiently small in comparison to the other currents. As a result, due to the higher currents, I am required to run my chip in *hypertime*: in other words, faster than biology. Thus, it is necessary to scale all the time constants,

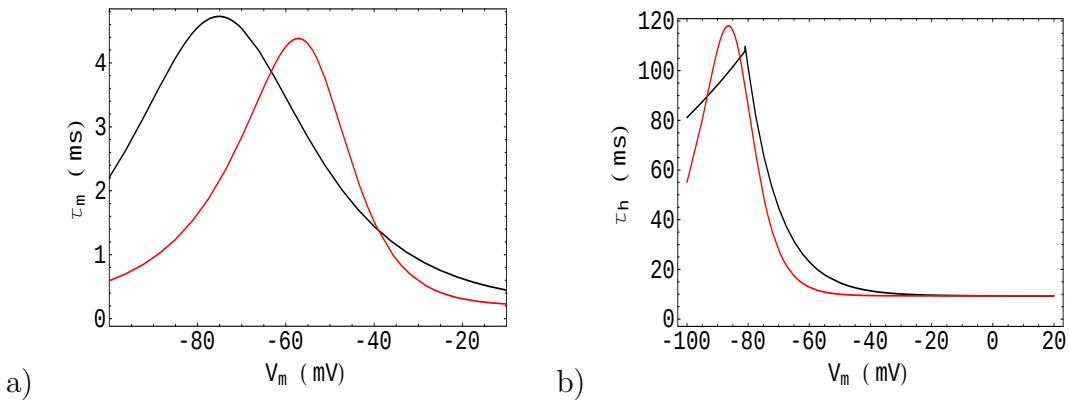

Figure 3.15: Time constant comparison between silicon and empirical models

Empirical (black) versus silicon (red) time constant equations for (a) activation and (b) inactivation. The mappings from the silicon membrane voltages to biological membrane voltages for each of the variables are calculated using their respective steady state curves. The silicon curves are scaled to match the depolarized inactivation time constants.

both within the I_T circuit and within all other circuits (e.g., synaptic).

To look at the performance of my silicon model, I compare the results of my voltage clamp experiments to the empirical equations from Figure 3.1. While the empirical equations are part of another model (Hodgkin-Huxley), they fit well all of the voltage-clamp data from real cells (Figure 3.5), providing the general shape of each function. However, in making the comparison, I only discuss obvious qualitative differences, as opposed to precise quantitative differences.

Figure 3.15 plots the time constant equations for the silicon and empirical models for activation (Figure 3.15(a)) and inactivation (Figure 3.15(b)). Since the membrane voltages for the silicon neuron span a different range than real cells, I use the steady-state sigmoids to define a mapping from one voltage space to another, allowing a

direct comparison of the curves. In addition, the silicon curves have been scaled such that the inactivation time constant for both the silicon and empirical curves match at depolarized levels.

For the activation variable, the obvious difference is the position of the activation peak, which occurs at more depolarized voltages in my silicon model than in the empirical model. This means there is a substantial difference in the activation variable time constants at hyperpolarized membrane voltages, where the channel deactivates. Thus, my silicon I_T will deactivate much quicker than in real cells. However, this is unlikely to cause any problems, as after the cell activates, it typically only repolarizes once the channel has inactivated, which gives the channel the all-or-none response property[157]. This detail makes the time course of deactivation at these voltages unimportant as the channel dynamics depends on the much slower dynamics of deinactivation.

For the inactivation variable, the silicon design captures well the change in the time constant, from the slow deinactivation time course at more hyperpolarized levels (around the peak) to the faster inactivation dynamics at more depolarized levels. One concern, however, is the steeper slope at voltage levels lower than the peak: Cells receiving strong inhibition could deinactivate much quicker. However, I can counter this by limiting the level of hyperpolarization—through limits on the inhibition—within the cell.

3.6 Discussion

In this chapter I described my silicon implementation of the thalamic T channel current. I morphed the Hodgkin-Huxley variables involved in I_T—one for activation and one for inactivation—using a *log-domain* representation in voltage. I demonstrated that through my approach, I was able to capture both the sigmoidal steady-state properties of HH variables in addition to a dependence of the time constant on the membrane voltage.

A back gate approach was use to take into account the difference in degrees of magnitude in time constants between the m and h variables. Rather than increasing the size of the capacitor, I used the back gate to artifically increase the capacitance by ≈ 5 times (assuming $\kappa \approx 0.8$). Though that was the intent, other factors, such as leak currents in the design, limited the maximum time constant to levels faster than biology. To compensate in the following chapters, I am required to scale all time constants within the system accordingly. The limitations due to leakage can be decreased through transistor sizing (using longer transistors) in the layout stage of chip design.

Another problem, possibly more serious, is *mismatch* within the series mirrors (transistors P2-P5 and N7-N8 in Figure 3.11). Though a mirror may be designed with unity gain, the output of the mirror, in reality, is scaled by a random variable because of mismatch. Thus, each successive mirror increases the variance of this gain. How does this affect the inactivation circuit? From Equation 3.30, the inactivation variable $h = I_m^-/(I_m^- + I_m)$. The current in the numerator is the output of the series mirrors, and the mismatch gain appears as a random variable multiplying h. Thus, rather than h approaching unity as the cell hyperpolarizes, h will approach this gain.

Like the leakage currents, mismatch can be reduced through transistor sizing. While leakage goes down with transistor length, mismatch is inversely proportional to the square root of the transistor area[105].

Overall, though, the circuits worked well in capturing the temporal and steady-state dynamics of each HH variable, though not without flaws. For activation, the peak of the time constant curve was sufficiently shifted to more depolarized voltages such that at deactivation voltages, $\approx$ 80mV, the temporal dynamics of activation in the the silicon model would be much quicker. This, however, is unlikely to affect the results from the silicon model, since at these voltages the slow deinactivation makes the much faster deactivation dynamics unimportant. The main concern for the inactivation variable was the steeper slope in the time constant at voltages more negative to the peak. However, any effect here can be limited by controlling the level of hyperpolarization that deinactivates I_T.

How does this model improve on previous designs? The most obvious improvement is the incorporation of a membrane voltage dependent time constant for each of the gating particles. This opens the door to capturing some of the richer dynamics seen in neuron models. The other improvement within my model is in the efficiency of the design, which I measure in terms of total number of transistors[7]. To capture the activation and inactivation dynamics of the T channel, I used 23 transistors: 13 for inactivation, 3 for activation, 3 for the channel output and 4 for generating V_m^-. The model used by Simoni et al.[128] has 44 transistors: 16 each for activation and inactivation and 12 for the output. This is a considerable difference in size, largely due to the modular nature of their model. In addition, the time constants for both of

[7]I am ignoring capacitors as all models use two capacitors—one for activation and one for inactivation—within their circuits

their variables are fixed, so including more circuitry to model the membrane voltage dependence would make their designs even larger.

A T current model using the same principles as in [85] would consist of 20 transistors, 8 each for activation and inactivation and 4 additional transistors for the output. This is slightly smaller in size than my circuit. However, in addition to the concerns with this circuit mentioned in Section 3.2.2, the circuit also implements a fixed time constant for both activation and inactivation. Adding additional transistors to include this would then increase the size of their circuit.

Overall, my design captures the temporal dynamics of the T channel, while keeping the design smaller in size than existing models. My model was not perfect; in addition to the minor flaws described above, there is also room for other improvements, such as duplicate HH variables. While these issues are not important for my model, they may be more important in models of other membrane conductances. Fortunately, with the lower number of transistors in my design, these modifications can be made while still keeping circuit size down.

Chapter 4

Relay Neuron Model

In the previous chapter, I introduced my silicon model for the low threshold calcium channel. The next step is to merge this model with a silicon neuron and study how I_T affects the response properties of the cell. This is the focus of the current chapter.

First, I present the silicon neuron, consisting of a cell body (with the T channel) and a synapse. Following that, I use two techniques to characterize the response of the cell to investigate changes in the response of the neuron due to I_T. The first technique is the frequency response of the cell using input currents. This technique has been applied to real neurons, allowing me to validate the performance of my silicon cell. The second technique uses nonlinear analysis methods to extract the system function using the properties of the output response to a random input stimulus. These nonlinear methods are often useful in situations where knowledge of the system is either limited, or too complex to solve analytically. The result is a set of kernels, which capture synaptic, membrane and I_T dynamics.

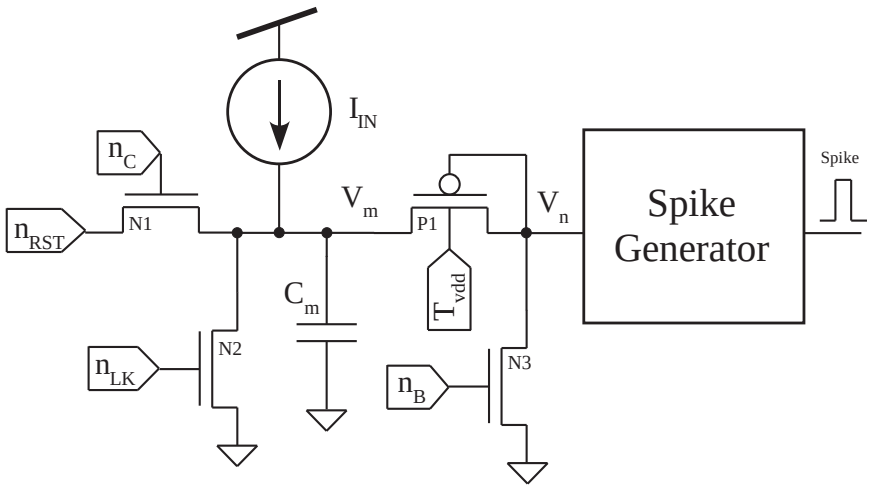

Figure 4.1: Neuron Circuit

The neuron circuit is composed of two modules: a capacitor C_m that models sub-threshold neuron dynamics and a spike generator that is active only when V_m is sufficiently high. Transistor N1 acts as a passive membrane conductance that, absent any input, pulls the membrane voltage to n_{RST}. Transistor N2 is a membrane leak that adjusts the resting membrane potential down from n_{RST}. See text for details.

4.1 Neuron Circuit

The complete neuron circuit incorporates both the cell and the synaptic circuits. The synapse circuit presented here is the foundation for all synapses: slow, fast, excitatory and/or inhibitory. The details of the synaptic interactions between cells within each chapter will be discussed within the respective chapter.

4.1.1 Cell Circuit

The T channel circuit from the previous chapter is not constrained to a specific neuron model. The output of the model is a current, but this is because of the model medium: The *transistor current* can be used to represent either the *channel conductance* or the *channel current*. The actual representation depends on the choice of the neuron.

Many neuromorphic models have used the simple (non-leaky) integrate and fire (IF) circuit as the basis of their neural processing. Inputs into the neuron—whether from a synapse or a membrane channel—are currents, rather than conductances. Spike generation is abstracted to a voltage threshold crossing, followed by a reset to Gnd, rather than the complex dynamics of activation and inactivation of Na^+ channels and the delayed rectifier K^+ channels. Without membrane conductances, the membrane voltage rises linearly, from reset to threshold, in response to a constant input current. Thus, above its *rheobase*[1], the response frequency of the cell is linear with input current. This makes the IF neuron a suitable model for the *spiking* relay neuron (i.e., for input currents above the rheobase), which exhibit a linear frequency-input current response (see Figure 2.5(a)). Subthreshold dynamics, however, require something akin to a membrane leak to vary the membrane voltage with the input current. This is important as the membrane voltage trajectory affects the dynamics of voltage-dependent membrane channels, like the T channel.

Taking these issues into account, Figure 4.1 shows the circuit for my silicon relay neuron. The spike generator is an IF neuron: Output spikes are generated at a rate proportional to the input current into the membrane, represented by the voltage V_n. The IF circuit, by itself, is not suitable for voltage-dependent membrane channels,

[1]The rheobase is the smallest stimulus magnitude that elicits an action potential from a neuron.

mainly because after spike generation, V_n is reset all the way to Gnd. If we use the same membrane voltage mapping as in Figure 3.15(b) (i.e., from silicon to real voltage space), this repolarization in the silicon neuron would be equivalent to a real neuron repolarizing to < -100mV. This would dramatically alter the activation and inactivation dynamics of the T channel during a burst, as the channel would begin to deactivate and deinactivate. Real thalamic cells, however, repolarize to much higher membrane voltages (Figure 2.4), minimizing the influence of spikes on I_T.

One solution to this problem is to modify the IF circuit to reduce the voltage range of V_n. This is not simple: The current levels involved in spike generation and reset are orders of magnitude greater than synaptic and membrane currents, due to its role as the interface between the analog membrane circuits and the digital off-chip communication. Thus, any modification would need to be resilient to large current spikes. A simpler solution is to isolate the subthreshold dynamics from the spike generator, and activate the latter only when the cell depolarizes. That is the role of the diode (transistor P1 in Figure 4.1): the membrane voltage V_m at the source terminal of the diode needs to be sufficiently high (i.e., depolarized) for current to enter the spike generator. After the IF circuit generates a spike, the reset current rapidly lowers V_n. Since V_n and V_m are the gate and source voltages (respectively) of transistor P1, lowering V_n increases the current in P1, which decreases V_m. However, the rate at which V_m decreases is much slower than V_n for a couple of reasons: 1) the current level through P1 is much smaller than the reset current due to the smaller gate-source voltage difference; 2) the total capacitance at the node for V_m is larger than the capacitance at the node for V_n (by design). As a result, V_m resets only a small amount after each spike (Figure 4.2), while V_n resets to Gnd. The current through transistor N3 keeps V_n below V_m.

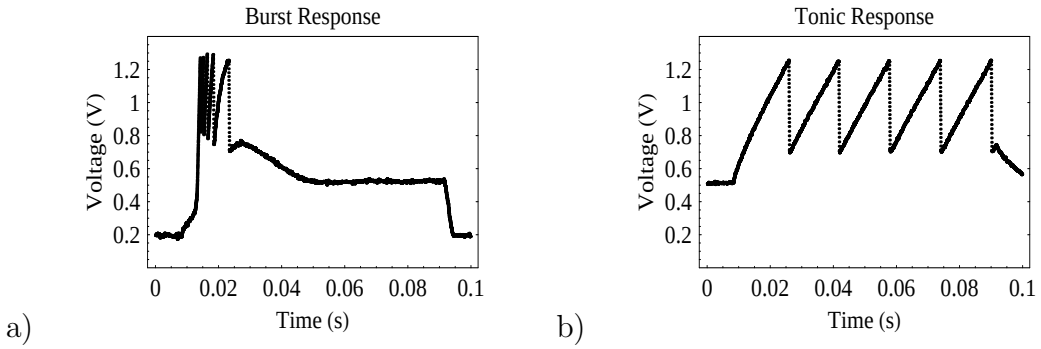

a) b)

Figure 4.2: Silicon Response Modes

The two figures plot V_m for the two response modes of the relay cell: a) Burst; b) Tonic. The initial voltage level controls the initial state of I_T, and thus the response mode. For bursts, the cell begins in a hyperpolarized state ($\approx$ 200mV) to deinactivate I_T, while for a tonic response, V_m begins depolarized ($\approx$ 500mV) to inactivate I_T.

The subthreshold circuit consists of the capacitor C_m and a passive membrane current (transistor N1). Absent any other input current, transistor N1 pulls V_m toward the resting potential n_{RST}. When the total input current is negative (i.e., largely inhibitory), V_m, acting as the source terminal, drops until the current in transistor N1 matches the input. An additional leak transistor (transistor N2) provides the means to adjust the resting potential through a separate synapse, similar to the metabotropic synapses found in thalamic cells (Section 2.1). The leak functions like an inhibitory input: Increasing n_{LK} lowers the resting membrane potential from n_{RST}. For positive input currents, V_m becomes the drain terminal for N1. The rheobase of the cell is actually the sum of the currents through transistors N1-3; once the input surpasses this threshold, V_m—along with V_n—rises towards threshold and the cell spikes.

Figure 4.2 plots V_m for the silicon cell illustrating its two response modes. From

an initial hyperpolarized membrane voltage (Figure 4.2(a)), a step increase in the input current causes the cell to burst. Once I_T inactivates, the cell stops spiking and V_m settles at a depolarized level. If the initial membrane voltage is sufficiently high (Figure 4.2(b)), I_T begins inactivated and the same step in the input results in a tonic response. V_m rises linearly to threshold from reset, and so the firing rate of the cell is proportional to the magnitude of the input current.

4.1.2 Synapse Model

The synapse circuit (Figure 4.3), designed by John Arthur in Kwabena Boahen's lab, is a transistor representation of a simple kinetic synapse model that relates to biophysical mechanisms of transmitter release and binding to receptors[26]. The circuit can be divided into two subcomponents: Figure 4.3(a) represents the transmitter release and uptake in the synaptic cleft while Figure 4.3(b) models the dynamics of transmitter binding.

4.1.2.1 Synaptic Cleft

Following the arrival of a presynaptic spike at an axon terminal, neurotransmitter is released into the synaptic cleft by the fusion of transmitter-filled vesicles to the terminal membrane. The transmitter remains in the cleft while it binds to receptors on the postsynaptic site, only to be removed through various processes, such as reuptake by the axon terminal or diffusion out of the cleft.

In the transistor model, a pre-synaptic spike arrives at the source of transistor P1, dumping a quanta of charge (transmitter) onto the 'cleft' capacitor C_T. The voltage

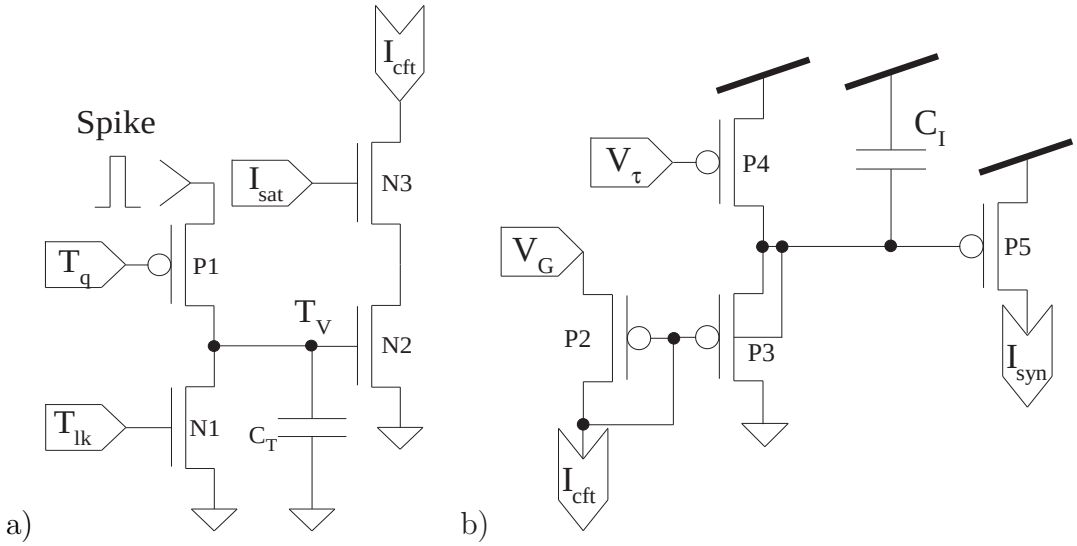

Figure 4.3: Synapse Circuit

The synaptic model represents transmitter release, uptake and channel dynamics. a) This circuit represents the neurotransmitter processes within the synaptic cleft. Transistor P1 controls the quantity of transmitter released into the cleft, which integrates onto the capacitor. The total transmitter within the cleft is represented by the current through transistor N2. Transistor N1 leaks charge from the capacitor, representing the uptake of transmitter. Transistor N3 represents the number of binding sites. b) Transistors P2-5 act as a low-pass filter, which models the ion channel dynamics of opening and closing, the time constant of which is controlled by transistor P4. The source voltage V_G controls the gain on the input current I_{cft}.

T_q at the gate of transistor P1 controls the amount of transmitter released after each input spike. Once transmitter enters the cleft, current (I_{cft}) begins to pass through the two series output nFETs (Appendix A.2), described by

$$I_{cft} = \frac{I_{Tmtr}\, I_{sat}}{I_{Tmtr} + I_{sat}}. \tag{4.1}$$

I_{sat} represents the total number of receptor binding sites, and thus sets the maximum level of I_{cft}. I_{Tmtr} is the current within transistor N2 set by the voltage T_V. In typical mode of operation, following the arrival of a presynaptic spike, $I_{Tmtr} \gg I_{sat}$ and thus $I_{cft} \approx I_{sat}$. Uptake (or diffusion) of transmitter is set by the leak transistor N1, which draws charge at a constant rate off of C_T, causing I_{Tmtr} to decay exponentially towards zero. Once $I_{Tmtr} < I_{sat}$, the output I_{cft} decays exponentially with I_{Tmtr}. Functionally, the output of the synaptic cleft circuit is a pulse of height I_{sat} whose width, Δ, is controlled by the leak transistor N1.

4.1.2.2 Channel Dynamics

The receptor binding—or channel opening—is modelled using a current low-pass filter (Figure 4.3(b)). The dynamics are described by

$$\tau \frac{dI_{syn}}{dt} + I_{syn} = \gamma\, I_{in} \tag{4.2}$$

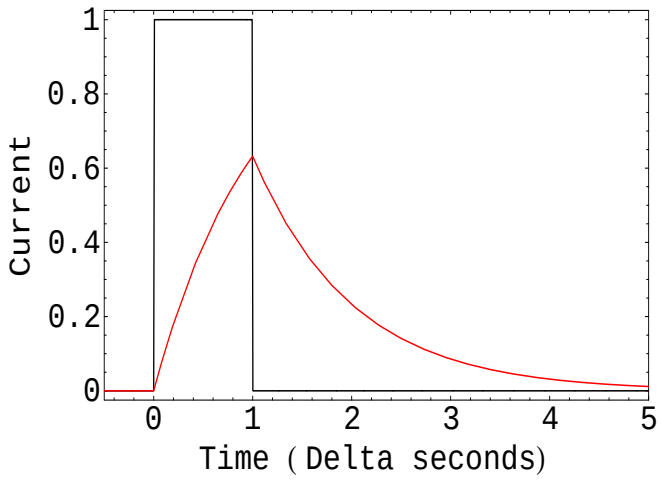

Figure 4.4: Synapse Output

Depiction of the synapse circuit output. Black curve represents the transmitter current I_{cft}. The red curve shows the output current, as it rises during the pulse and afterwards decays. Time axis is relative to the time constant of the synapse, and assumes a pulse duration of τ. The current has been normalized to peak cleft current I_{sat}. The gain γ is assumed to be one.

where $\tau = C_T\ U_T/I_{lk}$ and γ is a gain introduced through the source bias V_G. Thus, after the arrival of a presynaptic spike and release of transmitter into the cleft, the input pulse from the cleft circuit into the low-pass results in the following synaptic current,

$$I_{syn}(t) \quad = \quad \gamma\ I_{sat}\left(1 - e^{-\frac{t}{\tau}}\right). \tag{4.3}$$

After the pulse ends, assuming an ideal pulse,

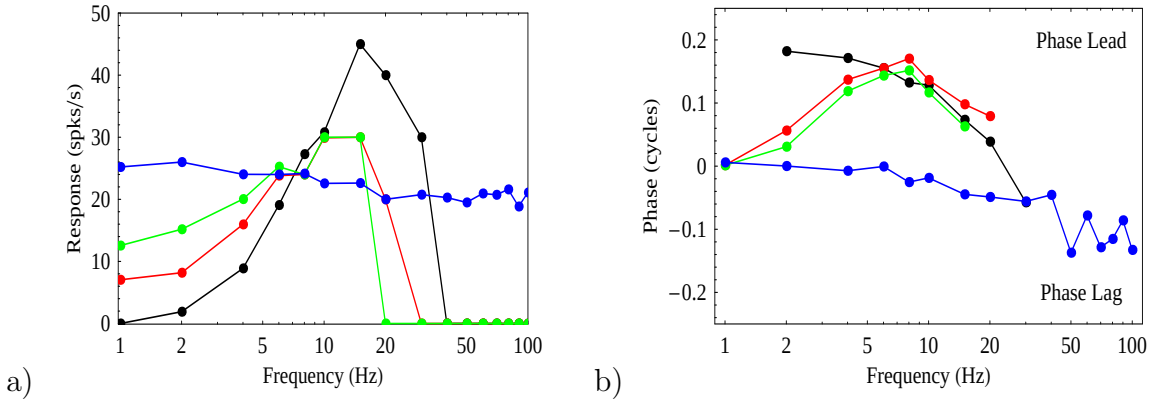

Figure 4.5: Frequency Response

Frequency response of the cell for different firing states: burst (black), tonic (blue) and two burst-tonic (red and green). The mean response (a) and phase (b) are extracted through the Fourier transform of the output peri-stimulus time histogram (PSTH), each trial corresponding to a single cycle[130]. The response mode of the cell is adjusted through the mean current level of the input sinusoid.

$$\begin{aligned} \mathrm{I_{syn}}\left(t\right) &= \gamma\, \mathrm{I_{sat}} \left(1 - \mathrm{e}^{-\frac{\Delta}{\tau}}\right) \mathrm{e}^{-\frac{\mathrm{t}}{\tau}} \\ &= \mathrm{I_{pk}}\, \mathrm{e}^{-\frac{\mathrm{t}}{\tau}}, \end{aligned} \tag{4.4}$$

where $\mathrm{I_{pk}}$ is the largest current reached at the end of the transmitter binding saturation period (the pulse). The dynamics are demonstrated in Figure 4.4.

4.2 Frequency Response

Figure 4.5 shows the frequency response of the silicon cell using input current. Real thalamic cells express a change in their mean response from bandpass in burst mode to all-pass in tonic mode (Figure 4.6); Figure 4.5(a) shows a similar evolution for the silicon cell. In a pure burst mode (black), *any* response in this state is dependent on I_T as input current is insufficient to overcome the rheobase of the cell. Thus, the dynamics of inactivation define the level of the response. At high frequencies, the cell spends insufficient time at hyperpolarized levels for I_T to deinactivate. At low frequencies, the rise in V_m is too slow and I_T inactivates before it can activate. The peak response occurs at about 15Hz, approximately five times larger than for a real cell (Figure 4.6(a)), due to the five-fold drop in the inactivation time constant for the silicon model (Figure 3.12).

In a pure tonic mode (blue), the mean input current is raised such that the T channel is always inactive, and so the response, which is all-pass, is dependent solely on the input current. At low frequencies, the cell responds with multiple spikes on top of the sinusoid peak. As the frequency increases, the number of spikes within each cycle decreases. At frequencies greater than the mean response, the cell no longer is capable of generating spikes at every cycle, but responds subharmonically.

In between the two extreme states (plotted in red and green), the cell transitions between the two states, demonstrating properties from both modes. At low frequencies, there is a gradual increase in the tonic response with the mean input current, as the number of tonic spikes at the peak of the sinusoid increases. At the middle frequencies, where the T channel dynamics were predominant in the burst mode ($\approx 5 - 30$Hz), the burst response diminishes with increasing mean input current as

there is less deinactivation of I_T, due to the higher membrane voltages in the troughs of the sinusoid. The higher frequencies do not demonstrate any response, not even a tonic response as seen at the lower frequencies. The current levels in these two intermediate states are too low to integrate to threshold during the input peak, even subharmonically.

Figure 4.5(b) plots the response phase. At the higher frequencies, the burst response lags the input but quickly switches to leading the input as the frequency decreases. The phase asymptotes to about +0.2 cycles, as the frequency decreases further. This response is easily understood: Once the input surpasses the rheobase, there is a latency to the I_T burst, due to membrane integration and to I_T activation. For low frequencies, this latency is negligible compared to the input period, and so as the frequency drops, the phase asymptotes to the position in the phase where the input sinusoid overcomes the rheobase. As the frequency increases, the latency becomes more and more significant, moving the burst towards the peak of the input and eventually past it.

The tonic response always lags, since its dynamics are solely input dependent. Only at low frequencies, where there is approximately equal response before and after the input peak, does the tonic phase approach zero. However, like the burst case, there is an initial integration that introduces a response latency. At low frequencies, it is negligible, but as the period shortens, the latency becomes significant, causing a greater phase lag.

The phase of the two intermediate states follow the phase of whichever state (burst or tonic) is dominant. At the low frequencies, where the tonic response is the strongest, the phase of both intermediate states meet the tonic phase curve. As the

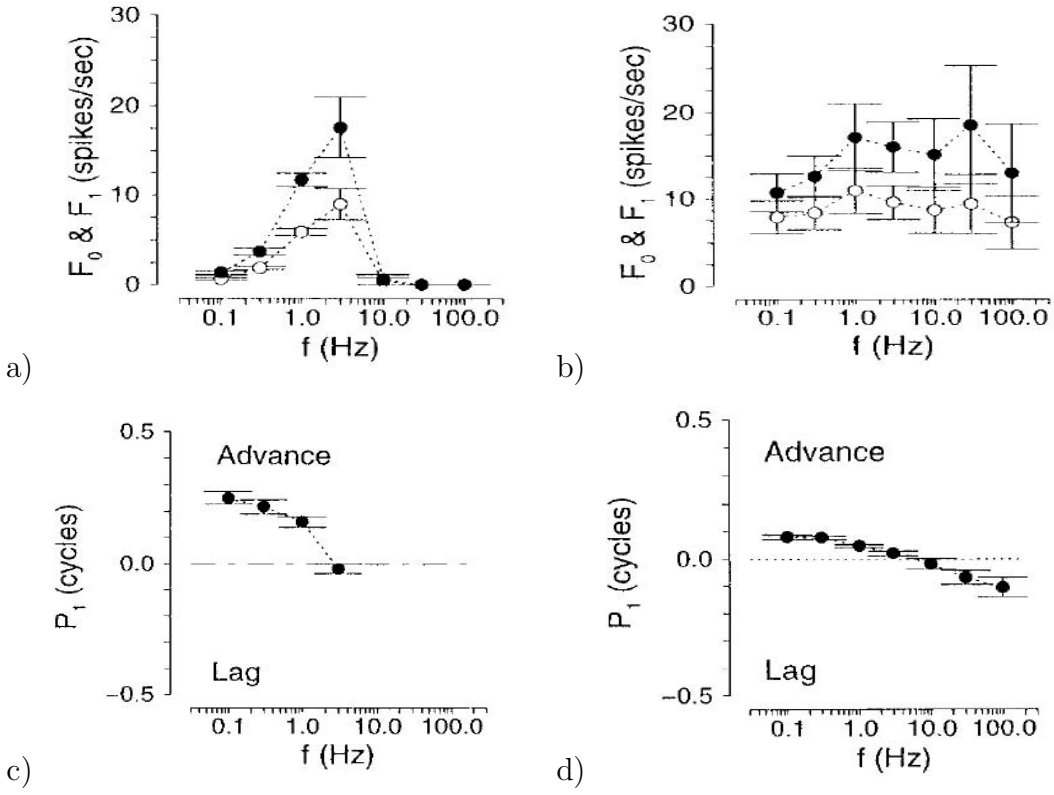

Figure 4.6: Frequency Response of Real Cells

The top row plots the frequency response of a thalamic cell in (a) burst and (b) tonic modes. Both plots show the mean (F_0, open circles) and the fundamental component (F_1, filled circles) of the response. The bottom row plots the phase for (c) burst and (d) tonic modes. From [130].

input frequency increases, the phases diverge from the tonic curve and meet the burst phase curve where the T channel dominates the activity.

For real cells (Figure 4.6(c,d)), the phase response in burst mode is similar: leading—and asymptoting—in phase at low frequencies, but shifting towards a phase lag at higher frequencies. In tonic mode, rather than starting at zero phase for low frequencies as in my response (Figure 4.5(b)), real cells begin with a phase lead and shift towards a phase lag as the frequency increases. The discrepancy is explained through a slight frequency adaptation existing in real neurons, which results in a stronger initial response—and thus a phase lead—at the low input frequencies.

4.3 Nonlinear Analysis

For nonlinear systems, methods have been developed to characterize the system operation where linear techniques break down. This section first provides a background on some of those techniques, and then applies them to my neuron circuit under conditions with and without the T channel.

4.3.1 Volterra Series

A single input system can be represented mathematically by the expression

$$y(t) \;=\; \mathrm{H}[\,x(t)\,].$$

The system operator $\mathrm{H}\left[\, x\left(t\right) \,\right]$ defines a mapping from a time-varying input $x\left(t\right)$ to a continuous time-varying output $y\left(t\right)$. In this form, no information is given about the operation itself. This is often the case: the internal mechanisms are either ignored, due to complexity, or simply not known. The goal is to quantify what the system is doing.

Under certain conditions[2], the operation $\mathrm{H}\left[\, \ldots \,\right]$ can be expanded into a power series:

$$y\left(t\right) \;=\; \sum_{n=1}^{\infty} \int_{-\infty}^{\infty} \cdots \int_{-\infty}^{\infty} \mathrm{h_n}\left(\sigma_1, \cdots, \sigma_n\right)\; x\left(t-\sigma_1\right) \cdots x\left(t-\sigma_n\right)\; \mathrm{d}\sigma_1 \cdots \mathrm{d}\sigma_n \tag{4.5}$$

This is the *Volterra series*, the *functional* analog of the Taylor series expansion of a function. The operator $\mathrm{h_n}\left(\sigma_1, \ldots, \sigma_n\right)$ is called the n^{th} order Volterra kernel, and the highest kernel order defines the order of the system.

These kernels are the system processing elements; that is, these kernels define how the input is mapped into different elements of the output. What do these kernels represent? Imagine a pure first order system:

$$y\left(t\right) \;=\; \int_{-\infty}^{\infty} \mathrm{h_1}\left(\sigma\right)\; x\left(t-\sigma\right)\; \mathrm{d}\sigma \tag{4.6}$$

This is easily recognizable as the convolution integral, or a linear system with memory.

[2]Time invariance and finite memory

The output $y(t)$ is a linear combination of the past history of $x(t)$, defined by the kernel $\mathrm{h}_1(\sigma)$. That is, $\mathrm{h}_1(\sigma)$ 'weighs' how sections of $x(t)$ affect $y(t)$. What about the higher order kernels? Looking at a pure second order system:[3]

$$y(t) = \iint_{-\infty}^{\infty} \mathrm{h}_2(\sigma_1, \sigma_2)\ x(t-\sigma_1)\ x(t-\sigma_2)\ \mathrm{d}\sigma_1\ \mathrm{d}\sigma_2. \tag{4.7}$$

Here, $\mathrm{h}_2(\sigma_1, \sigma_2)$ defines how two different sections of the stimulus—separated in time by $(\sigma_2 - \sigma_1)$—interact and contribute to the output $y(t)$. Thus, extending to higher orders, the n^{th} order kernel $\mathrm{h_n}$ defines the interaction and contribution of n different sections of the stimulus.

Given knowledge of all the system kernels, the exact output for any given stimulus can be computed, using Equation 4.5. However, calculating the kernels is often the crux. The difficulty in the task lies in separating the contributions from each kernel to the output.

4.3.2 Wiener Series

The Wiener series is an attempt to address this problem. Like the Volterra series in Equation 4.5, the Wiener series is a sum of functionals (called Wiener G-functionals) of increasing order:

[3]For notational simplification, the range of integration of some integrals has been omitted. All integrations, unless noted, are over the range $(-\infty, \infty)$.

$$y(t) \;=\; \sum_{n=0}^{\infty} \mathrm{G_n}\left[\,\mathrm{k_n}, x(t)\,\right].$$

However, for gaussian white noise at the input, the G-functionals are constrained by the condition

$$\mathrm{E}\left[\;\mathrm{G_n}\left[\,\mathrm{k_n}, x(t)\,\right]\;\mathrm{G_m}\left[\,\mathrm{k_m}, x(t-\sigma)\,\right]\,\right] = 0, \tag{4.8}$$

for all σ, and $m \neq n$. $\mathrm{E}[\,\ldots\,]$ is the expectation, or the average, over time. Equation 4.8 enforces orthogonality between functionals of a different order through the statistical properties of the random input. Thus, this condition defines[4] the form of the functional as

$$\mathrm{G_n}\left[\,\mathrm{k_n}, x(t)\,\right] \;=\; \iint_{-\infty}^{\infty} \mathrm{k_n}\left(\sigma_1, \ldots, \sigma_n\right)\; x\left(t-\sigma_1\right)\ldots x\left(t-\sigma_n\right)\; \mathrm{d}\sigma_1 \ldots \mathrm{d}\sigma_n,$$

where $\mathrm{k_n}$ is called the n^{th} order Wiener kernel. Each kernel provides the best estimate for interactions to that degree. Thus, a Wiener series provides essentially the 'best fit' to nonlinearities up to the highest degree of the series, and each additional kernel that is included in the representation improves on the accuracy of the result.

[4]See appendix A.3 in [112] for a quick overview of the kernel orthogonalization process.

How are the individual kernels extracted? The input stimulus $x(t)$ can itself be represented as a first order functional, with a Wiener kernel of $\delta(\sigma)$. Thus, taking the expectation of the output-input product:

$$\begin{aligned}
\phi_{yx}(\sigma) &= \mathrm{E}[\, y(t)\, x(t-\sigma)\,] \\
&= \mathrm{E}\left[\left(\sum_{n=0}^{\infty} \mathrm{G_n}[\, \mathrm{k_n}, x(t)\,] \right) x(t-\sigma) \right] \\
&= \sum_{n=0}^{\infty} \mathrm{E}[\; \mathrm{G_n}[\, \mathrm{k_n}, x(t)\,]\; x(t-\sigma)\;].
\end{aligned}$$

Using Equation 4.8 and the fact that $x(t) \equiv \mathrm{G_1}[\, \delta(t), x(t)\,]$, all but one of the terms in the summation can be eliminated. Thus,

$$\begin{aligned}
\phi_{yx}(\sigma) &= \mathrm{E}[\; \mathrm{G_1}[\, \mathrm{k_1}, x(t)\,]\; x(t-\sigma)\;] \\
&= \mathrm{E}\left[\left(\int_{-\infty}^{\infty} \mathrm{k_1}(\sigma_2)\, x(t-\sigma_2)\, \mathrm{d}\sigma_2 \right) x(t-\sigma) \right] \\
&= \int_{-\infty}^{\infty} \mathrm{k_1}(\sigma_2)\; \mathrm{E}[\, x(t-\sigma_2)\, x(t-\sigma)\,]\, \mathrm{d}\sigma_2 \\
&= \int_{-\infty}^{\infty} \mathrm{k_1}(\sigma_2)\; \mathrm{P}\, \delta(\sigma_2 - \sigma)\, \mathrm{d}\sigma_2 \\
&= \mathrm{P}\, \mathrm{k_1}(\sigma) \\
\therefore \mathrm{k_1}(\sigma) &= \frac{1}{\mathrm{P}}\, \phi_{yx}(\sigma),
\end{aligned}$$

where P is the power of the white noise input. The same procedure can be applied for n^{th} order kernels simply by taking the cross-correlation of the output and n input

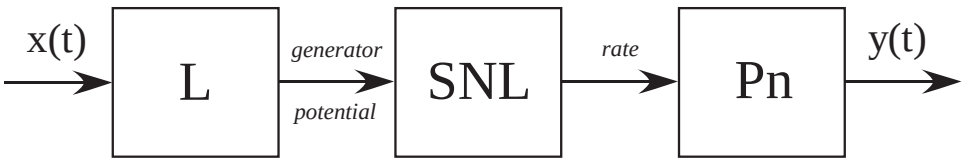

Figure 4.7: Neuron Kernel Model

A typical model applied in the analysis of neuron response. The system is a cascade of modules: an initial linear kernel (L) representing linear dynamics of membrane integration; a static nonlinearity (SNL) to capture any nonlinearities from the membrane dynamics and/or from spike generation; and a Poisson process (Pn) that generates spikes ($y(t)$) from the rate function (the output of the static nonlinearity).

functions, each shifted independently.

White noise analysis has been applied extensively over the past few decades to many sensory systems, especially visual (for a brief review, see [115]). The advantage of a technique like this, in addition to being simple (procedurally) to perform, is that it bypasses many of the details of the transduction process (e.g., of light to current for vision) and results in a set of kernels that are intuitive—at least in the first order case—to the researcher. In addition, the extension of the single-input model above to multiple inputs allows the vision researcher to expand the white noise stimulus spatially to study the spatiotemporal response: the "receptive field" of the cell.

But some neurons tend to function nonlinearly, and simple linear analysis may be insufficient to capture all the properties of the cell response. However, calculation of higher order kernels, though in theory quite simple, is often difficult in practice given the large amount of data required. One common solution is to cascade a linear kernel

with a static nonlinearity (Figure 4.7). Computation of the static nonlinearity is quite straightforward: for a given input, the output of the linear kernel (calculated using Equation 4.8) is compared to the actual output to view where the response moves away from linearity. This technique is useful for capturing complex nonlinearities such as rectification or saturation.

But how are neuron responses modelled since the Wiener series requires a continuous output signal while the output of a neuron is discrete spikes? The assumption in these models, which has been observed in cortical cells[132], is that the neuron acts as an inhomogeneous poison process. The probability of a spike is based on a continuous rate function, which becomes the continuous output signal being modelled. Typically, a representation of the rate function can be achieved by generating a *peri-stimulus time histogram* from multiple trials of the same input. However, due to the random nature of the spike generation, repeated trials are not necessary: The kernels can be calculated using spike data from a (sufficiently long) single run.

A slight variation on this approach is to model a membrane variable, such as membrane voltage [156] or membrane current[67], rather than the neuron rate. In these cases, the linear kernel is calculated in a similar fashion (i.e., input-output correlations), with the difference being that the output variable is directly measured (e.g., membrane voltage) rather than calculated by making assumptions on the properties of spike generation.

This model has been used successfully to study temporal contrast adaptation in both salamander ganglion[67, 13] and bipolar cells[111], to study contrast sensitivities in ON and OFF ganglion cell pathways[156] as well as in the study of Na^+ inactivation (input variance adaptation) in the salamander retinal ganglion cell[68] and to study

the speed of contrast adaptation[7].

4.3.3 Poisson Series

Nonlinear analysis is not limited to gaussian white noise as input, rather orthogonality of the system kernels can be achieved with any random stimulus. Using gaussian white noise, however, has a number of advantages. First, the independent nature of the statistics of white noise simplifies the kernel computation process (see [112] for a detailed explanation). Most importantly, gaussian white noise is a decent representation of the stimuli for the system, as it possesses equal power at all input frequencies and theoretically can represent all possible inputs. However, the kernels calculated with one stimulus pattern will not be the same as the kernels calculated using another, as they vary with the statistics of the probing stimulus. Thus, for systems that use stimuli that differ dramatically—in terms of statistics—from gaussian white noise, a more 'natural' stimulus—natural in terms of the system context—may be more useful.

For isolated neural systems, away from sensory inputs, trains of action potentials can potentially be more useful than gaussian white noise[73]. Using input spikes to probe the response of the cell lumps the synaptic processing into the membrane and provides a system response from input spike train to cell output.

The spike train equivalent to gaussian noise is a zero-mean input poisson spike train $x_p(t) = \sum_i \delta(t - t_i) - \lambda$, where λ is the poisson rate. The system representation is similar to the Wiener series:

$$
\begin{aligned}
y(t) &= \mathrm{z}_0 + \int \mathrm{z}_1(\sigma)\ x_p(t-\sigma)\ \mathrm{d}\sigma \\
&\quad + \iint_{\sigma_1 \neq \sigma_2} \mathrm{z}_2(\sigma_1, \sigma_2)\ x_p(t-\sigma_1)\ x_p(t-\sigma_2)\ \mathrm{d}\sigma_1\ \mathrm{d}\sigma_2 + \ldots . \qquad (4.9)
\end{aligned}
$$

The kernels are also calculated using input-output cross-corretions:

$$
\begin{aligned}
\mathrm{z}_0 &= \mathrm{E}[\, y(t)\,] \\
\mathrm{z}_1(\sigma) &= \frac{1}{\lambda}\, \mathrm{E}[\, y(t)\ x_p(t-\sigma)\,] \\
\mathrm{z}_2(\sigma_1, \sigma_2) &= \frac{1}{2}\frac{1}{\lambda^2}\, \mathrm{E}[\, y(t)\ x_p(t-\sigma_1)\ x_p(t-\sigma_2)\,]
\end{aligned}
$$

Neural spike trains, however, possess a positive, non-zero mean, due to the fact that a spike train is a series of events, with zero input otherwise. Thus, to calculate the kernels above correctly, the cross-correlations above need to be re-organized to represent the actual spike train $x(t) = \sum_i \delta(t - t_i) = x_p(t) + \lambda$. Thus, substituting $x_p(t) = x(t) - \lambda$:

$$
\begin{aligned}
\mathrm{z}_0 &= \mathrm{E}[\, y(t)\,] \\
\mathrm{z}_1(\sigma) &= \frac{1}{\lambda}\, \mathrm{E}[\, y(t)\, x(t-\sigma)\,] - \mathrm{z}_0 \\
\mathrm{z}_2(\sigma_1, \sigma_2) &= \frac{1}{2}\left(\frac{1}{\lambda^2}\, \mathrm{E}[\, y(t)\, x(t-\sigma_1)\, x(t-\sigma_2)\,] - \mathrm{z}_1(\sigma_1) - \mathrm{z}_1(\sigma_2) - \mathrm{z}_0\right)
\end{aligned}
$$

The kernels $\mathrm{z_n}$, however, are only useful for the system defined in Equation 4.9, where the input spike train has a zero mean. It is desirable to reach a final form of

$$\begin{aligned} y(t) &= \mathrm{g_0} + \int \mathrm{g_1}(\sigma)\ x(t-\sigma)\ \mathrm{d}\sigma \\ &\quad + \iint_{\sigma_1 \neq \sigma_2} \mathrm{g_2}(\sigma_1, \sigma_2)\ x(t-\sigma_1)\ x(t-\sigma_2)\ \mathrm{d}\sigma_1\ \mathrm{d}\sigma_2 + \ldots \end{aligned} \tag{4.10}$$

where the kernels $\mathrm{g_n}$ are specific to the non-zero mean input. These kernels can be calculated by substituting $x_p(t) = x(t) - \lambda$ into Equation 4.9 and grouping terms of the same order together. For the first order term:

$$\begin{aligned} \int \mathrm{z_1}(\sigma)\ x_p(t-\sigma)\ \mathrm{d}\sigma &= \int \mathrm{z_1}(\sigma)\ [x(t-\sigma) - \lambda]\ \mathrm{d}\sigma \\ &= \int \mathrm{z_1}(\sigma)\ x(t-\sigma)\ \mathrm{d}\sigma - \lambda \int \mathrm{z_1}(\sigma)\ \mathrm{d}\sigma \end{aligned}$$

Two terms are apparent: a linear term and a constant term. Continuing with the second order (Note: $x(t, \sigma_1) \equiv x(t - \sigma_1)$):

$$\begin{aligned} \iint \mathrm{z_2}(\sigma_1, \sigma_2)\ x_p(t, \sigma_1)\ x_p(t, \sigma_2)\ \mathrm{d}\sigma_1 \mathrm{d}\sigma_2 &= \iint \mathrm{z_2}(\sigma_1, \sigma_2)\ x(t, \sigma_1)\ x(t, \sigma_2)\ \mathrm{d}\sigma_1 \mathrm{d}\sigma_2 \\ &\quad -2\lambda \int \left[\int \mathrm{z_2}(\sigma_1, \sigma_2)\, \mathrm{d}\sigma_2 \right] x(t, \sigma_1)\ \mathrm{d}\sigma_1 \\ &\quad +\lambda^2 \iint \mathrm{z_2}(\sigma_1, \sigma_2)\, \mathrm{d}\sigma_1 \mathrm{d}\sigma_2 \end{aligned}$$

The expansion of the second order kernel leads to a constant term, a linear term and a second order term. Thus, if we group the expressions above into their respective orders:

$$\begin{aligned}
\mathrm{g}_0 &= \mathrm{z}_0 - \lambda \int \mathrm{z}_1(\sigma_1)\, \mathrm{d}\sigma_1 + \lambda^2 \iint \mathrm{z}_2(\sigma_1, \sigma_2)\, \mathrm{d}\sigma_1\, \mathrm{d}\sigma_2 \\
\mathrm{g}_1(\sigma_1) &= \mathrm{z}_1(\sigma_1) - 2\lambda \int \mathrm{z}_2(\sigma_1, \sigma_2)\, \mathrm{d}\sigma_2 \\
\mathrm{g}_2(\sigma_1, \sigma_2) &= \mathrm{z}_2(\sigma_1, \sigma_2)
\end{aligned}$$

For each additional order included into the system, the lower order kernels are modified by removing some of these order effects. Thus, a first order system will best try to match the output in the linear kernel. Adding a second order kernel then removes any second order effects that may have been captured in the first order 'best-fit'. Each additional order modifies the response of all the lower order terms.

Kernel interpretation for a spike train stimulus, given its discrete nature, is much more intuitive than for gaussian white noise. The linear kernel is the response of the system to each individual input spike. The second order kernel, which is not very intuitive in the continuous input case, demonstrates the response of the cell to two spikes *on top of* the sum of the individual linear kernels (Figure 4.8). Explained another way: the second order kernel is the response of the system to the *interspike interval* of input spikes. Extending to higher orders, the n^{th} order kernel represents the effect on the output of the system from all combinations of n spikes.

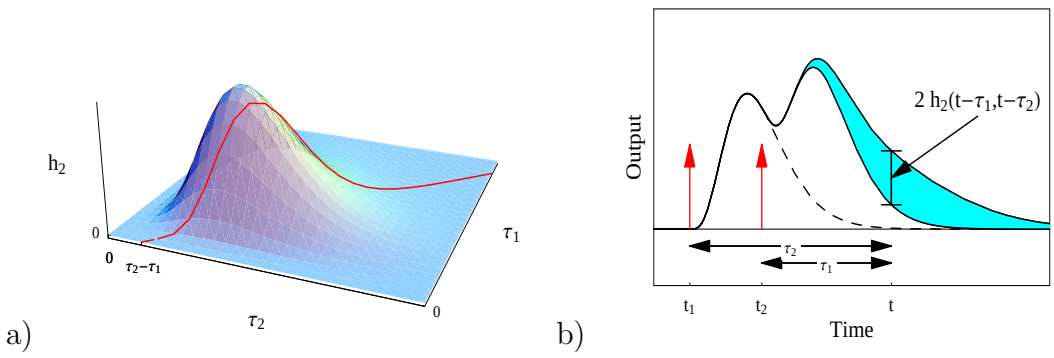

Figure 4.8: Second Order Kernel Interpretation

a) A sample 2^{nd} order kernel (arbitrary output units). The interspike interval $\sigma_2 - \sigma_1$ between pairs of input spikes defines the second order effect (shown in red). b) A sample output response to two input spikes (red arrows). In a linear system, the output would be the sum of the response of individual linear kernels (black solid line, shaded white). The *interspike-interval* defines the second order effects, and mainfests itself as an addition to the linear response (shaded in cyan).

4.3.4 The Model

Figure 4.9 shows the abstract system model of the silicon relay neuron. The input and the output of the system are spikes, part of the motivation for using spike trains instead of Gaussian white noise for kernel calculation. H [. . .] represents the synaptic, membrane, and T channel dynamics, the output of which feeds into an IF neuron.

The nonlinear techniques described above assume a continuous output signal. When these techniques have been applied before on neurons (Figure 4.7), there is an implicit assumption the neuron functions as a Poisson spike generator; that is, the probability of a spike in a small window of time is proportional to the output rate. This random nature of the spikes eventually—over the whole stimulus interval—

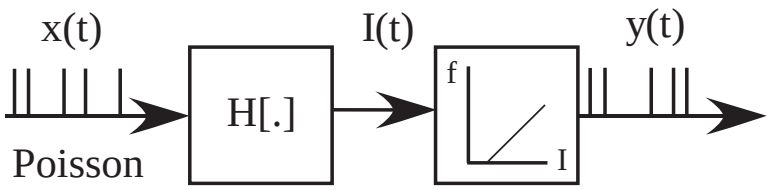

Figure 4.9: Model of the Silicon Neural System

H[. . .] represents the synaptic, channel and membrane dynamics of the silicon relay neuron. The output of this operation is a current that feeds into a simple integrate and fire (IF) neuron. The input and outputs of the system are spike trains.

captures the relationship between the input signal and the output rate, which is then captured by the kernels.

Unfortunately, this assumption is not valid for my system. The output of my silicon cell is very deterministic: The same input will produce identical spike trains[5]. Since a continuous rate curve cannot be modelled through the binning of the output spikes, or through repeated trials, then a rate function must be generated from the actual output data (Figure 4.10).

The premise of the procedure in Figure 4.10 is that the output rate is a reflection of the input current into the IF neuron (I(t) in Figure 4.9). The output spike train is converted into a series of pulses, with the area of each pulse equal to one. The width of the pulse is not simply the interspike interval between output spikes, rather it is between each response spike and the closer of: 1) previous response spike or 2) previous stimulus spike at least some minimum interval away. Using only the

[5]There may be some inherent noise in our silicon chip, but hardly sufficient amounts to induce randomness

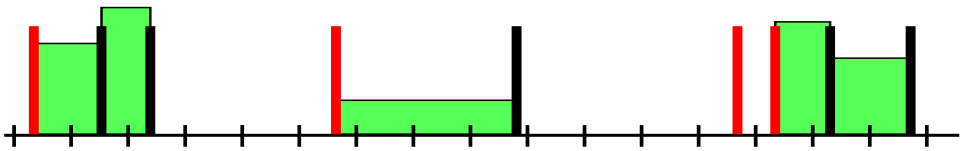

Figure 4.10: Rate Function Generation

Converting the output spike train to a spike rate. Each qualified interspike interval is replaced with a pulse (green) whose integral over the ISI is one. A qualified interspike interval is defined as the time between a response spike and the closest previous spike, either a stimulus of minimum distance (red) or another response (black). Within bins where the spike occurs, the 'rate' becomes a weighted combination of the pre- and post-spike rates, with the weight dependent on the position of the spike within the bin.

output interspike interval is not accurate, as the input current is averaged over the whole interspike interval rather than where it actually appears. For example, the contribution of an input spike to a single output spike, preceded by a long interspike interval, would be averaged out over the entire interspike interval. This technique that I adopt accounts for this situation. However, given the random nature of the input Poisson spikes, it is necessary to include a restriction on the minimum interval between acceptable stimulus-response pairs to prevent narrow 'rate' pulses with large heights. The minimum interval is chosen as the smallest *output* interspike interval within the whole data set. This is effectively saying that the largest synaptic current due to a single spike cannot occur immediately after the spike due to a synaptic rise time (Appendix 4.1.2.2).

Once the kernels have been calculated, the model performance can be tested by generating a spike train and comparing it to the actual output of the silicon chip.

The kernels have units of rate, as in firing rate of the cell, and thus the convolution of the kernels with a sample spike train (according to Equation 4.10) produces a time-varying rate function. To generate the output spike train, I integrate the model rate function (recall that the rate function is a representation of the input current into the IF neuron) until a threshold (one) is surpassed. The unit threshold corresponds to the use of unit area pulses in the generation of the rate function from the actual spike train (Figure 4.10). Thus, if the rate function reaches a predicted rate of over 1000Hz, then a spike is guaranteed within a bin for binsizes greater than 1ms.

4.3.5 Results

The synaptic parameters for the excitatory inputs were set to values based on biological observations. The time constant matches observed decay time constants of AMPA receptors, approximately 5ms for cortical synapses[49, 22, 25]. Assuming 100% overlap of retinal and geniculate receptive fields, the efficacy of retinogeniculate synapses is approximately 30%[145], where efficacy represents the percentage of retinal spikes that cause a geniculate spike.

The data in this chapter, so far, has been presented in *real-time*; that is, the data is presented as it has been recorded, with the time constants that are faster than biology (see Chapter 3). For the remainder of this chapter and the following chapters, I will scale all my results with a *hypertime factor* of 10, so that the results are plotted on a timescale similar to biology. Note that I am using a different silicon chip—with different transistor and capacitor sizes—than from the previous chapter, where the hypertime factor was only 5.

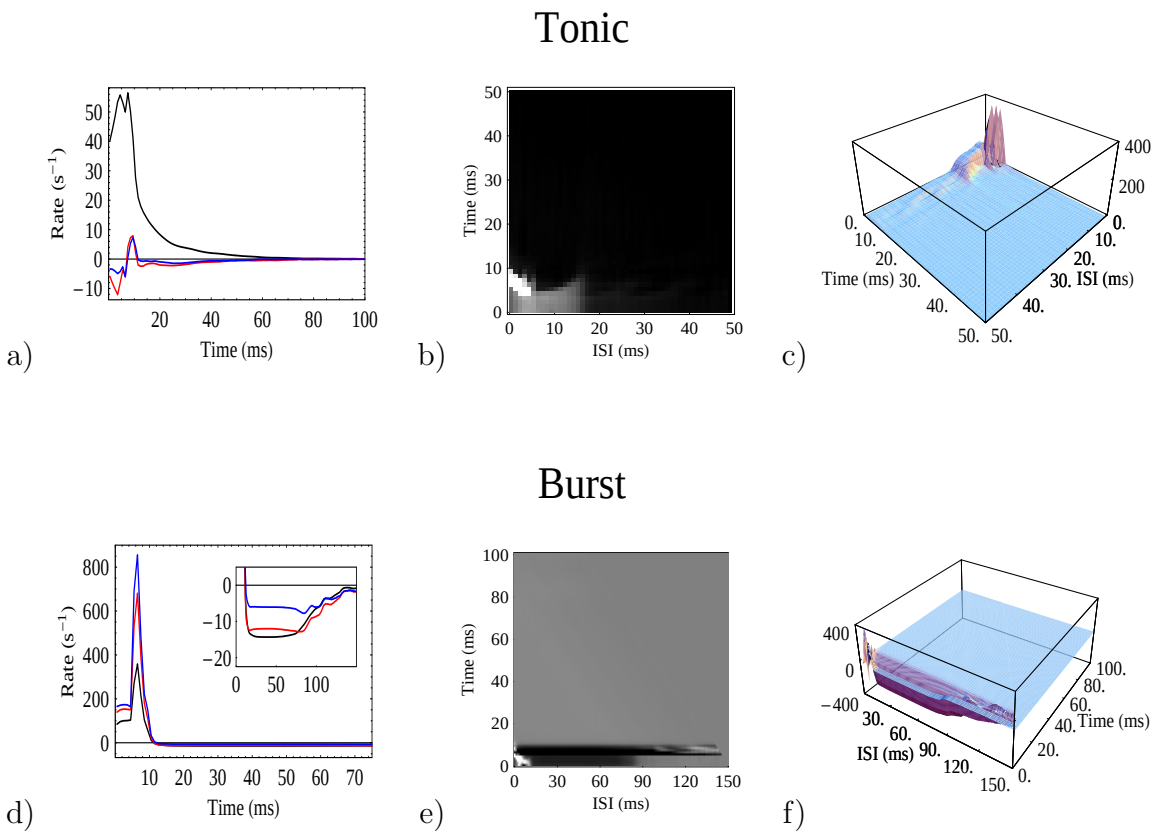

Figure 4.11: Poisson Kernels

Poisson Kernels for 10Hz input Poisson stimulus. The top and bottom rows show the tonic and burst kernels, respectively, for the TC cell. The left column shows K_1 for 1st (black), 2nd (red) and 3rd (blue) order models. The inset in (d) shows the post-peak negative trough. The middle and right columns show K_2 of a third order model, in the form of density and 3D plots respectively. In the tonic density plot (b), the grayscale value (0–1) is linear from 0–200Hz, and values outside this range are cut-off. In the burst density plot, the same grayscale range maps to -200–200Hz. Note the different axes ranges between the tonic and burst kernels. The units on the z-axis of the 3D plots are rate (Hz).

Figure 4.11 shows the first (K_1) and second (K_2) order kernels of both burst and tonic modes for a 10Hz Poisson stimulus. In tonic mode (Figure 4.11(a-c)), the only dynamics present in the system $H[\ldots]$ are synaptic and membrane. This is easily seen in K_1 of a first order model (black curve in Figure 4.11(a)): the average post-spike response is a rise to a peak followed by a decay to zero, mimicking synaptic dynamics (Figure 4.4(a)).

When the order of the model is increased to two or three, K_1 disappears:[6] The output becomes much more dependent on the interaction between multiple input spikes. This is not surprising, since I chose the synaptic weights to necessitate multiple input spikes for output activity. K_2, then, reflects this interaction (Figure 4.11(b,c)). For two, almost synchronous, input spikes, there exists a tall peak, indicating the occurrence of two output spikes. As the interspike interval of the inputs grows, the peak disappears as the cell now responds with one spike. Eventually, as the interspike interval becomes too large ($>$ 15ms apart), there is no longer any significant interaction between the input pair.

Lowering the resting potential of the membrane voltage increases the likelihood of I_T deinactivation, resulting in substantial changes in the kernels (Figure 4.11(d-f)). K_1 shows two dramatic changes: a much taller, tighter peak followed by a negative trough. The larger peak is the result of the burst nature of the cell: the firing rate during bursts is substantially higher than during regular tonic mode. The negative trough represents the channel inactivation and the time necessary for I_T to

[6]It is not clear why K_1, for higher order models, shows a negative bump followed by a positive one. I suspect the reason lies within the generation of the higher order kernels, where the interspike interval is always rounded down to the start of a bin. This causes a slight phase lead in K_2 of a higher order model relative to K_1 of a first order model. Thus, when generating K_1 for the higher order model (Appendix 4.3.3), this phase difference would show up as an initial negative bump followed by a positive one. Decreasing the bin size should reduce this effect, which appeared to be the case (data not shown).

deinactivate. After a burst, it is very unlikely a burst will follow within approximately 100ms.

Increasing the model order does not eliminate K_1, as in the tonic case; rather, there is an enhancement of the burst peak. K_2, like its tonic counterpart, also demonstrates a peak at small ISIs, but in this mode it likely represents both synaptic and T channel effects. However, as the ISI increases, the peak quickly changes into a deep trough, extending out to approximately 100ms. The width of this trough, and position in time, match the peak in K_1.

Thus, the kernels interact in the following manner: The response to each input spike (K_1) is, by default, a burst, but the strength of the burst is adjusted by K_2, which captures the dynamics of channel inactivation. This helps explain the change in the peak of K_1 as the model order increases. For a first order model, K_1, being the *average* response after each spike, includes both burst and non-burst events. In the higher order models, the non-burst events are captured through the modulation of K_1 by the higher order kernels.

How do the kernels change with the input Poisson rate? The tonic kernels for an input rate of 20Hz (Figure 4.12(a-c)) do not show a substantial change from Figure 4.11(a-c). K_1 retains the same shape, only scaled accordingly to account for the higher output rate. For K_2, the most significant changes occur at higher ISIs where, in Figure 4.11(c), the response was negligible. These minor changes are most likely higher order system kernels polluting the response, due to the increased likelihood in the input of multiple, short ISIs. However, the fact that K_2 does not show dramatic changes is an indication that the second order model captures well the tonic response.

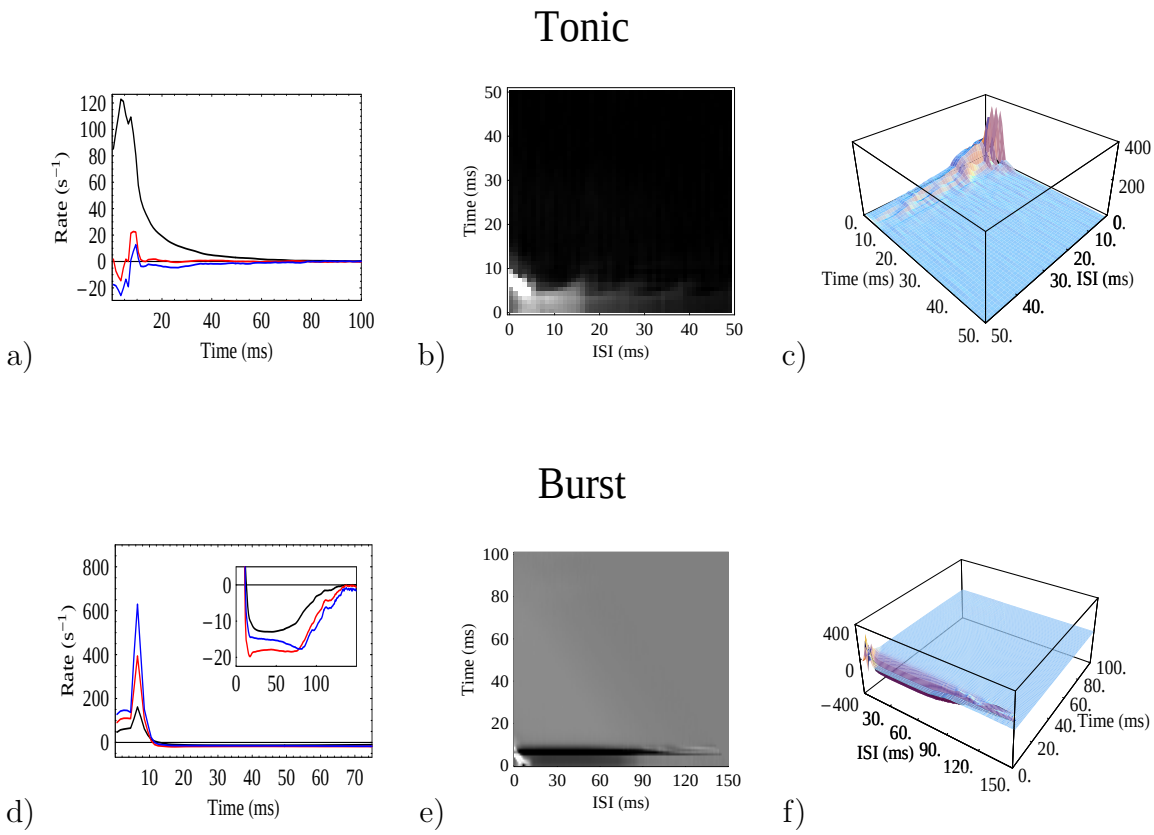

Figure 4.12: 20Hz Poisson Kernels

Similar kernels as in Figure 4.11, except using a stimulus rate of 20Hz.

In burst mode (Figure 4.12(d-f)), the higher input rate causes a decrease in the kernel properties associated with I_T: namely, a decrease in the peak in K_1 and the troughs in both K_1 and K_2. By increasing the input frequency, the cell's membrane voltage is more often depolarized than with the 10Hz stimulus, thus decreasing the occurrence of bursts in the output response.

As discussed in Section 4.3.4, the accuracy of the system model can be tested by generating a spike train using the kernels and comparing it to the actual output from the silicon chip. Figure 4.13 shows the comparison of the predicted spike trains

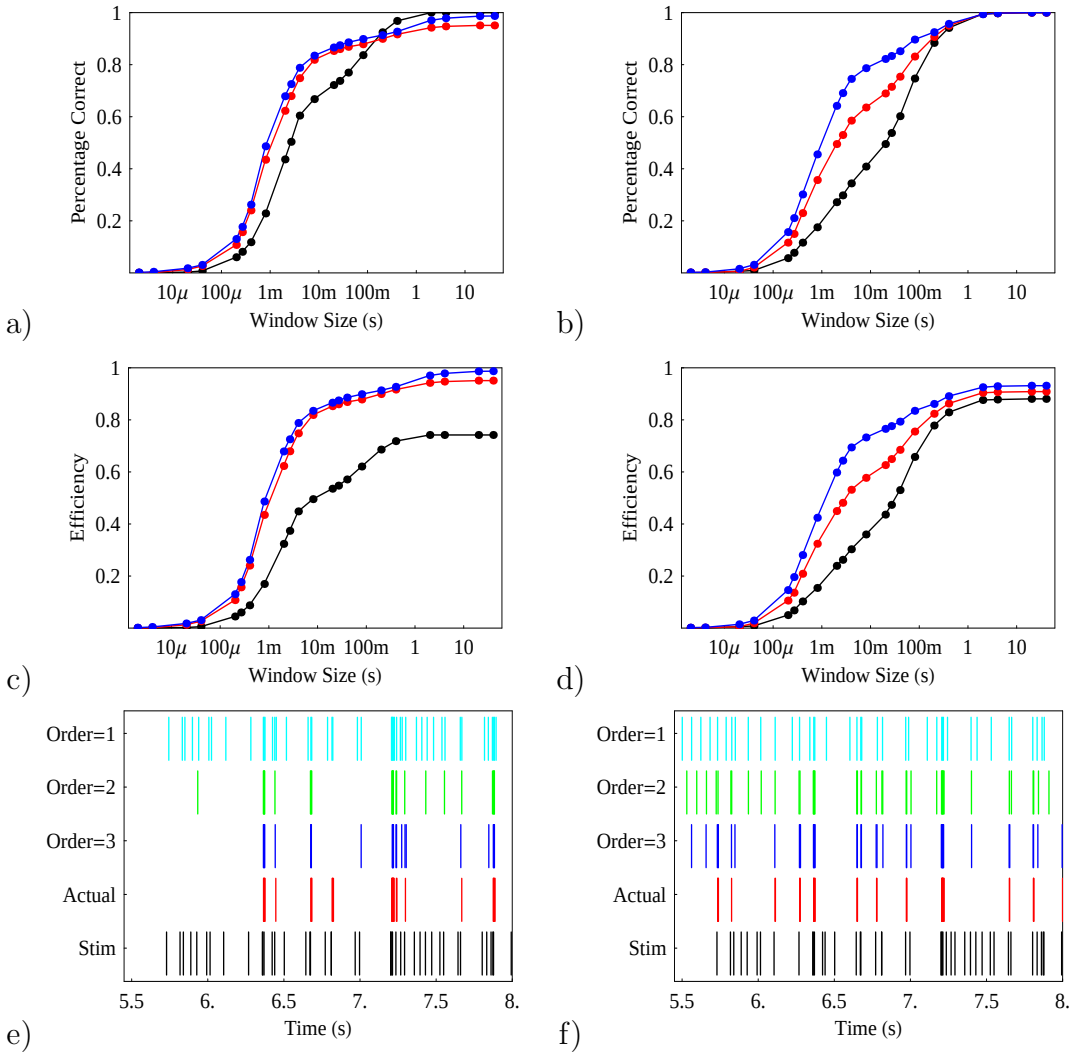

Figure 4.13: Model Performance

a,b) Percentage of actual spikes accurately predicted for a silicon cell in (a) tonic and (b) burst mode. First, second, and third order models (black, red and blue respectively) are plotted versus window size. c,d) Efficiency of the models for (c) tonic and (d) burst modes. Efficiency takes into account over-predicting (i.e., including too many prediction spikes) that may distort the results in (a) and (b). e,f) Sample raster plots for stimulus, actual response and model response of all three orders for the cell in (e) tonic and (f) burst mode. Spike trains were compared using a distance metric based on spike times, defined in [147].

to the real data for both tonic and burst modes. The top row in Figure 4.13 plots the percentage of correct spikes in the predicted train (i.e., number of correct model spikes divided by the number of actual output spikes) versus a window size (i.e, maximum distance for being considered correct)[7]. In the tonic case, there is an obvious improvement in the model output from first to second (approximately 60% versus 83% at 10ms), but hardly any improvement from second to third. This suggests again that the second order kernel captures much of the synaptic dynamics of the system. In the burst mode, obviously due to the nonlinearities introduced by I_T, each increase in model order increased the output accuracy, by roughly 20% per order (at 10ms).

The second row plots the efficiency of each model; that is, the measure includes a penalty for excess spikes, by dividing the number of correct spikes by the sum of the number of actual output spikes and the number of spike 'deletions' (i.e., excess spikes). Using this measure, it is clear that, in tonic mode, the first order model only performed as well as it did simply by over-predicting the number of output spikes, as is seen in Figure 4.13(e). The higher order models do not show significant change while shifting the measure from percentage correct to efficiency, suggesting they were capable of capturing the temporal dynamics of the synaptic response. In the burst case, all three orders slightly overestimated the output spike train; however, the overpredictions decreased with increasing model order.

[7]The window size corresponds to the cost of shifting a spike in the distance metric of [147].

4.4 Discussion

This chapter focusses on my relay neuron circuit, consisting of the circuits for the T channel, cell and a single excitatory synapse. The goal was to study the changes in the response of the isolated relay neuron caused by I_T, and compare them to results from biology. For that, I used two different techniques.

The first technique involved calculating the frequency response to input current sinusoids. The mean current level of the input set the degree of burstiness of the response by shifting the resting potential of the cell. Four response modes were measured: a pure burst mode, a pure tonic mode, and two hybrid burst-tonic modes. During pure burst mode, the cell exhibited a bandpass response defined by the dynamics of the inactivation variable. For high frequencies, the membrane voltage was not hyperpolarized long enough to deinactivate I_T, while at low frequencies I_T inactivated before it could activate. The peak response occurred at approximately 15Hz. The tonic mode, by contrast, demonstrated an all-pass response, while the two hybrid responses consisted of components of the two extreme modes: a (smaller) peak from the burst response and low frequency components from the tonic response.

Similar experiments have been performed on real cells using both visual[100] and current[130] stimuli. The peak in the burst bandpass response, in both of these experiments, occurred at approximately 3Hz. This factor of five difference between the silicon bandpass response and the real neuron response is due to the silicon inactivation time constant that is five times smaller (Figure 3.12). Although the results from my chip do not demonstrate anything new, they do show that my neuron model exhibits characteristics similar to real cells.

For the second analysis technique, I applied an adaptation of the Wiener Series to calculate a set of kernels using input spikes, as opposed to white noise. I quantified the ability of these kernels to capture the system response by generating a spike train—using the kernels—and comparing it to the actual output from the silicon chip.

As expected, the burst mode is more nonlinear than the tonic mode, evidenced by the fact that a second order model captured the tonic response better than a third order model captured the burst response (approximately 83% vs. 74% efficiency at 10ms resolution, respectively). Increasing the tonic model to third order did little to improve the results of the model, suggesting the second order kernel was able to capture most of the synaptic and membrane dynamics within the cell. Not so with the burst model, which showed significant improvements from first to second to third order (approximately 38%, 59% and 74% at 10ms respectively) in regenerating the output spike train.

Any inability to fully recreate the output may have a couple of sources. First, the technique of converting the output spike train to a rate function may be inadequate due to its imprecise and discontinuous (i.e., pulse) nature. The accuracy of my conversion relies on the ability to properly match the contribution of the input spikes to each output. Without any knowledge of the input dynamics, this would be difficult. But kernel analysis is typically used for cases where the internal dynamics are unknown, making my approach for generating the rate function impractical. A couple other methods were considered: one used only the output spikes to generate an output rate function (as opposed to both output and input spikes in my analysis) and the other assumed the neuron functioned as a Poisson spike generator. The problems with both of these were already addressed previously in Section 4.3.4. The first

approach ignores the contribution of the input spike to the output rate, since the rate function is only computed using output spikes. Kernels calculated using the second approach demonstrate sharp peaks where the spikes occur, even multiple peaks for a burst, rather than a continuous function. This is due to the deterministic nature of my neuron, as opposed to the random nature of the Poisson spike generator.

The second source of error may be due to insufficient model order. In the burst case this is very possible, given the improvement in the model's efficiency with increasing order. Generating kernels higher than third order, however, becomes difficult due to the amount of experimental data that is needed.

When modelling a system using an order that is too low, the higher order kernels not represented will 'pollute' the lower order kernels. This was clear through the near-disappearance of K_1 in tonic mode as the model order was increased from one. However, the 'pollution' depends on the presence of the higher order response in the actual output. A problem with these nonlinear techniques is their dependence on the statistics of the probing stimulus. If the order of the model matches the order of the system, then the processing can be captured precisely in these kernels (assuming an accurate continuous output function). However, the generated kernels would only be valid for that specific input, since the operation of the system is computed using the components of the output. For example, from the burst results in Figure 4.11 and Figure 4.12, it is clear that as the input rate increased, the effects of the bursting decreased due to the increased likelihood of the membrane voltage being depolarized. Had I used an input rate sufficiently high, so that the membrane voltage remained constantly depolarized, the burst kernels would be very close to the tonic kernels; any difference would likely be due to the increased leak current to hyperpolarize the resting membrane potential. There would be no indication of the effects of the

bursting, since no bursts occurred in the output due to the inactivation of I_T.

Since the statistics of the input stimulus provide the context for the kernels, it would be easy to conclude that it is important to use the proper stimulus in probing the system response. However, this would complicate the calculations tremendously, as it is the statistics of the Poisson spike train that make the kernel computation very simple procedurally. If one chooses to use Poisson spike trains, then care must be taken in the interpretation of the results. I chose two input frequencies, 10Hz and 20Hz, such that the mean interspike interval—100ms and 50ms respectively—occurred outside and within the deinactivation range for I_T, to demonstrate the burst nature and the changes in the burst response due to the higher input. However, had I no knowledge of internal dynamics, I would have had to use a series of input rates to comprehend the full range of the system function.

A direct comparison to biological results is not possible as the exact technique has not been applied to geniculate cells. However, a comparable calculation to K_1 of a first order model is the *spike-triggered average*. The spike-triggered average (STA) represents the average input stimulus *before* each output spike; as such, it often involves a random continuous signal input (as opposed to spikes). Typically, in the visual system, the random stimulus is visual white noise. In my computations, K_1 is the average output *after* each input spike. The similarity in both rests within their computation: Both involve the correlation of the output and the input[19, 36], though normalized by opposing spike rates (i.e., either the mean of the input rate (for K_1) or the output rate (for STA)). Most importantly, however, is the fact that the firing rate of the input ganglion cell varies with the light intensity; as such, the kernels should qualitatively be similar, though reversed in time. Note that the vertical scales may be different, since the STA is measured in input units (e.g., amps for current stimuli)

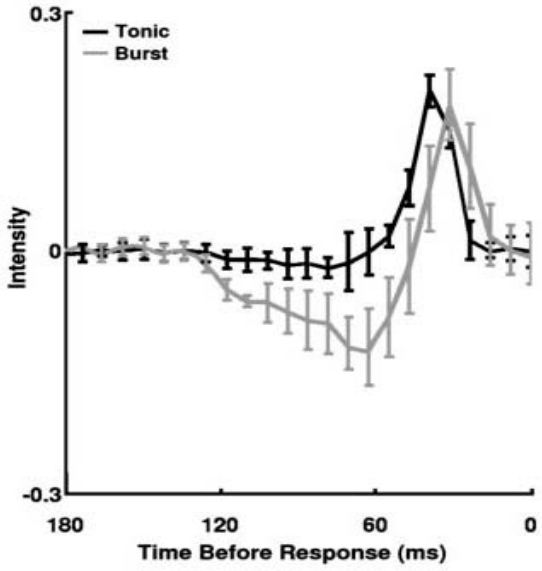

Figure 4.14: Spike-Triggered Average

Spike-triggered averages for the burst and tonic spikes of a relay neuron from an adult cat. The input stimulus was visual white noise. From [78].

while K_1 in my model is in units of the output (rate).

Figure 4.14 shows the STAs for burst and for tonic spikes from a cell in the cat LGN. Both STAs are similar to my kernels: a single peak in the tonic mode and a biphasic curve—a sharp peak followed by a negative trough approximately 100ms in length—in the burst mode. The trough in both instances represents the deinactivation of I_T necessary for the presence of the burst. However, the location of the peaks in the STA occur farther away from the temporal origin than in my kernels (approximately 30ms versus $<$ 10ms respectively). This is simply the result of the stimulus: the delays in the STAs are due to the retinal processing between the visual stimulus and the geniculate layer, while my inputs are directly into the cell. Another

difference involves the relative location of the peaks: the burst peak in the STA leads the tonic peak by approximately 5-10ms, while in my kernels the peaks occur roughly at the same location. This is likely due to my artificial output rate function, which represents the input current into an IF neuron (Figure 4.9). The STA focusses on the output spike itself, while my model focusses on the input that *integrates* to the output spike. While this difference would be negligible in the burst case (given the high-frequency of the burst response), it would be significant for the lower frequency tonic mode, introducing a temporal shift closer to the origin for the tonic kernel.

One other difference between my results and the STAs involve the experimental procedure. For the STAs, the output spike train is divided into burst events (i.e., first spike in a burst) and tonic spikes before computing the average. In my experiment, I biased the response mode to either tonic or burst, and then used all events for the calculation of the kernels. In the tonic case, it is unlikely any bursts appeared; in the burst mode, there is a possibility that some of the spikes are actually tonic events, present due to inactivation of I_T. However, I do not consider this to be a significant factor in the calculations given the huge difference between the computed kernels. Other studies have computed the impulse response for geniculate cells that demonstrate both a peak and an inhibitory dip[145], but in those situations there was no separation of burst and tonic events, and so it is possible the kernel contained components of both modes.

What do these results say about the processing in the single cell? Unfortunately, not much that was not already known. Both the frequency response results and the kernels demonstrate that the response of the cell can be dramatically adjusted by shifting the resting membrane potential. Some have suggested that the LGN acts as a 'tunable filter'[100, 130, 139], where the resting potential is modulated to achieve

the 'desired' processing. What controls the resting potential? Both cholinergic inputs from the parabrachial region and glutamatergic inputs from the cortex (which activate metabotropic receptors) can shift the resting membrane voltage through changes in a K^+ membrane leak, thus switching the cell between burst and tonic modes[84, 95, 39].

However, as discussed in Chapter 2, a problem with these theories is that, both the cholinergic inputs and the slow cortical glutamatergic inputs work at long time scales. Only a few cortical spikes are necessary to shift the membrane potential for a few seconds, and a longer spike train depolarizes the cell upwards of 20s[95]. However, fixation periods between saccades during visual scene perception, whether on dynamic[75] or static scenes[48], are much shorter (approximately 300ms), and so any long lasting depolarization of cells would prevent those cells from participating in subsequent post-saccadic scene analysis. It seems more likely that the cholinergic and the slow cortical glutamatergic inputs help signify a shift in the behavioral state of the system from sleep to awake[92, 95].

It is clear that the activation of the T channel has a dramatic effect on the response of the cell. The burst response is much stronger than the tonic response to visual stimuli, providing a more salient signal to cortical cells. But with the relay cells depolarized, this signal requires enough inhibition to change the kernel response from the tonic kernel to the burst kernel. This, then, creates a dependence of the burst on the presence of inhibitory action from the reticular nucleus, which is the focus of the next chapter.

Chapter 5

TC-RE Pair

In the previous chapter, I studied the influence of I_T on the response properties of a silicon relay neuron. The TC cell, however, does not work in isolation, but is one component in a large interconnected network, consisting of cells from the lateral geniculate nucleus and the perigeniculate/reticular nucleus.

Reticular (RE) cells are GABAergic and form inhibitory synapses within the geniculate layer. For TC cells—depolarized in the awake mammal—this feedback inhibition could be an important factor in the presence of bursts. Since both areas are retinotopically organized, each spatial location is represented by a set of cells in both layers. Therefore, in this chapter, I will use a pair of cells, one from each layer, to investigate how their interactions may lead to bursting and how cortical inputs influence the dynamics.

After a brief description of the setup, I begin by probing the dynamics of the cell pair to retinal Poisson spike trains, demonstrating the presence of burst events.

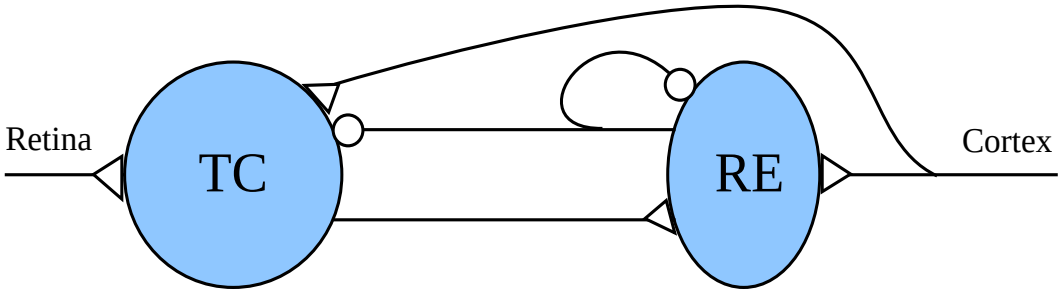

Figure 5.1: TC-RE Pair

Synaptic setup within the TC-RE system. Triangles represent excitatory synapses; circles, inhibitory. See text for details.

Following that, I spend a significant portion of the chapter designing a model that captures the cells' outputs, in response to both retinal and cortical afferents. I use the model to help shed some light on the role of the T channel in processing input stimuli. In the Discussion, I discuss the results in the context of experiments on real cells.

5.1 System Setup

Figure 5.1 shows the setup for the two cell mini-system, the organization of which has been discussed in Chapter 2. The TC and RE cells form an excitatory-inhibitory closed loop: the TC cell excites the reticular cell which, in turn, sends inhibition back to the thalamus[66]. Reticular cells also send inhibition to other reticular cells [2, 5], here represented as an inhibitory autapse. There are two inputs into the system: retinal axons, which drive only the TC cells, and cortical axons, which excite both cell types.

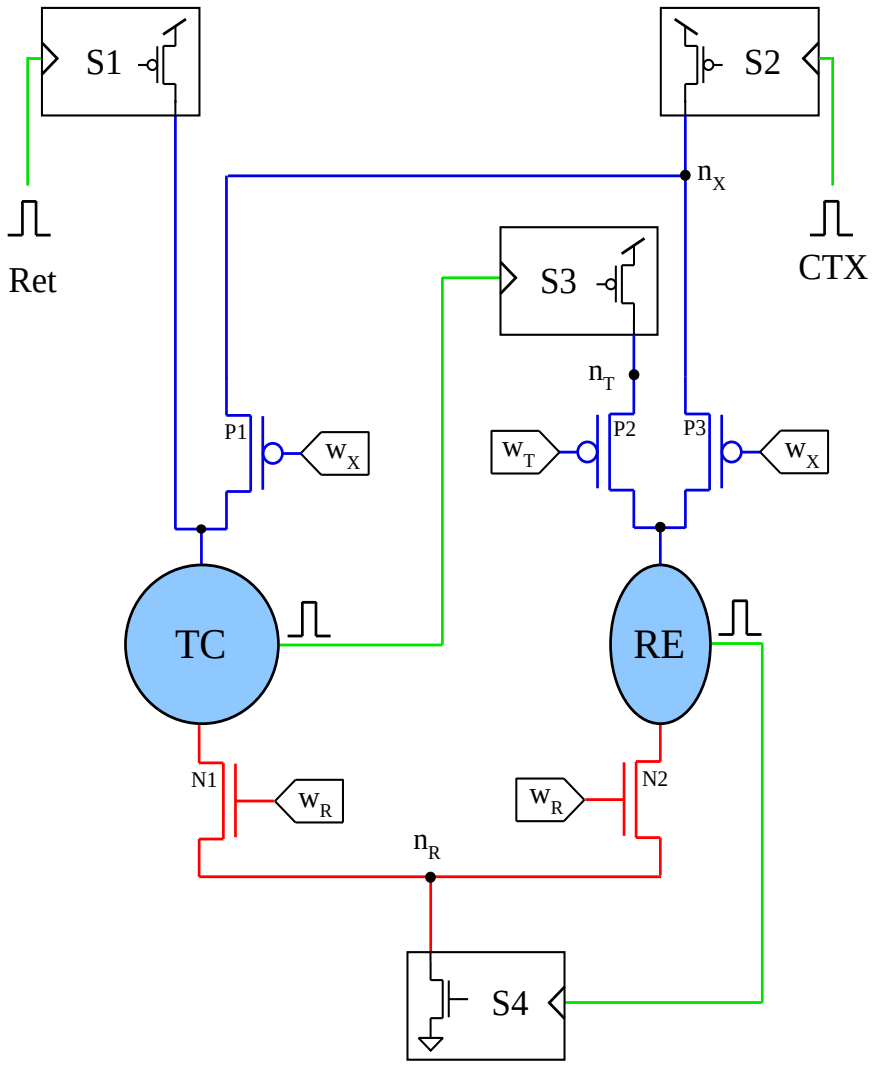

Figure 5.2: System Circuit

Circuit block diagram of the TC-RE system. This figure shows a more detailed diagram of Figure 5.1. The blocks S1-4 represent the synaptic circuit from Figure 4.3. Green lines represent axons, either afferent (retinal or corticothalamic) or internal (thalamic or reticular). Blues lines represent excitatory input into either cell, while red represents inhibitory input. Transistors P1-3 and N1-2 are part of the diffusor circuit used for network connectivity to the different layers (see Chapter 6). Nodes n_R, n_X, and n_T are the network nodes within the diffusors. The transistor types in the inhibitory synaptic circuit (S4) are reversed; that is, all PMOS transistors are NMOS and vice versa.

Figure 5.2 provides a more detailed circuit diagram of the synaptic connections within the system. Blocks S1-4 represent the synapse circuit presented in Section 4.1.2, with separate voltage biases defining the amplitude and time constant of the output current for each synapse. For the retinal synaptic parameters, I keep the values used in the previous chapter (see Section 4.3.5). For the remaining excitatory time constants, I use the same voltage levels since all the excitation in my circuit represents fast, ionotropic receptors.

The outputs of the cortical and the thalamoreticular synapses (S2 and S3 in Figure 5.2) both pass through an additional transistor (transistors P1-P3) before entering either cell. These transistors are part of the diffusor circuit used for network connectivity (see Chapter 6), and, here, limit (saturate) the synaptic input. Thalamic inputs demonstrate a saturation in their excitation of reticular cells[69], and so bias w_T sets the limit on the maximum input current. The limit on cortical synaptic inputs reflect the fact that cortical inputs are weaker than retinal ones. Inputs into thalamic nuclei are often classified as either *drivers* or *modulators*[122, 123]. Drivers define the response of thalamic cells: Retinal afferents are responsible for the receptive field of geniculate cells. Modulators influence the response of thalamic cells; for example, corticogeniculate feedback enhances the inhibitory surround of geniculate cells[17]. Thus, I set the voltage bias w_X sufficiently weak so as to prevent spiking through the cortical inputs over the range of input cortical frequencies (0-40Hz).

Inhibition from the reticular cells to thalamic cells is mediated through both $GABA_A$[141, 148] and $GABA_B$[140] receptors. However, my synaptic circuit possesses only one inhibitory synapse. To set the inhibitory time constant, I began initially at a voltage bias equal to the fast, ionotropic excitatory receptors for a time constant approximately 5ms, representing fast $GABA_A$ inhibition[104, 22, 25]. In

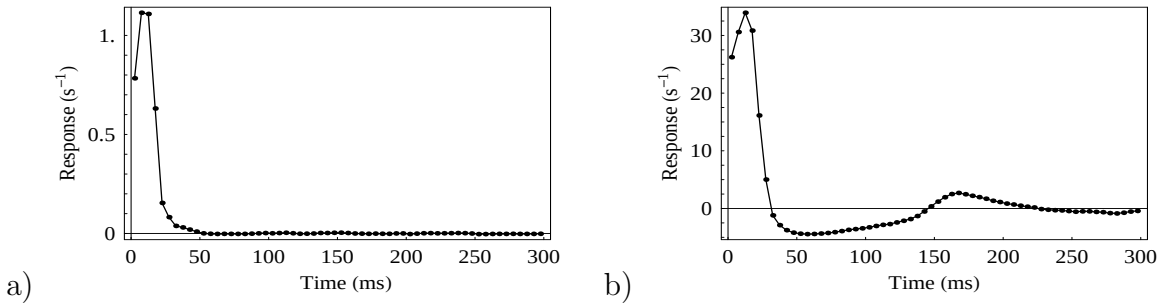

Figure 5.3: 1st Order Kernels

K_1 of a first order model for retinal Poisson spike trains of a) 1Hz and b) 40Hz.

this state, the duration of inhibition from a *strong* reticular output was insufficient to deinactivate I_T. Thus, I slowly increased the time constant (and magnitude) of inhibition until I saw an I_T response. The final time constant for inhibition ended up at approximately twice the magnitude of the fast $GABA_A$ synapses, representing a mixture of $GABA_A$ and $GABA_B$.

The resting potential of both the relay and reticular cells are set sufficiently high (depolarized) to inactivate I_T—in accordance to observed results for an awake animal[52, 134]—but sufficiently low to not generate a rebound burst absent an input. As in the kernel computations in the previous chapter, the hypertime factor is approximately 10.

5.2 Probing the Response

I begin by probing the response of the system to Poisson spikes trains at the retinal inputs. Figure 5.3(a) shows the first order kernel for the TC cell to a 1Hz Poisson

spike train. The kernel is similar in shape to the first order kernel of an isolated relay neuron in tonic mode (Figure 4.11(a)): At this input frequency, the response is dominated by retinal synaptic dynamics.

If I increase the input frequency to 40Hz (Figure 5.3(b)), the kernel displays some interesting new features. Rather than a simple scaling of the kernel (as in the previous chapter), the kernel develops a negative component followed by an additional positive bump. The negative dip cannot exist because of post-burst I_T inactivation, as in the burst mode kernels from the previous chapter (Figure 4.11(d)), because the ability of the cell to respond is not dependent on I_T. The post-peak dip must be the result of the inhibitory feedback from the RE cell, being the only other negative element in the system.

For the post-inhibitory bump, synaptic dynamics are ruled out due to its temporal location, (i.e., the synaptic input would have decayed by this point). It also cannot be caused by additional retinal afferents, as that would imply a correlation within the retinal spike train, not possible with Poisson spikes. Therefore, the only remaining source of excitation in the system is I_T.

Figure 5.4 plots both spike data sets from Figure 5.3 as *joint-interval histograms*. For an input of 1Hz, the data is centered about a mean interspike interval of about 100-200s. The output rate of the cell is so low because of the need for multiple input spikes at the synapse, and the probability of two spikes occurring within a few milliseconds at 1Hz is quite small.

At 40Hz, the histogram undergoes dramatic changes in its structure. Most of the response has fallen into three clusters, along the red lines in Figure 5.4(b). The lines

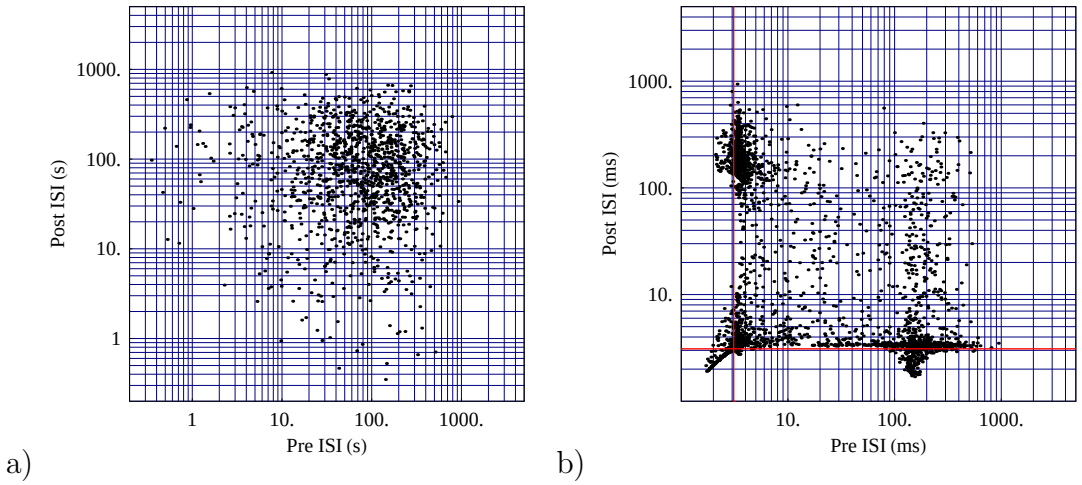

Figure 5.4: Joint Interval Histograms

The data from Figure 5.3 is plotted in a Joint-Interval Histogram for a) 1Hz input and b) 40Hz input. Each point represents a spike, with its coordinates defined by its pre- and post-interspike intervals. Note the unit change on the axes between plots.

represent (approximately) the minimum interspike interval (ISI) caused by synaptic input. All the points that fall on the inside of these lines (i.e., closer to the axes) represent the additional excitation by I_T, and thus represent spikes within a burst. The points at the bottom right of Figure 5.4(b) are the initial spikes within a burst: The long, pre-spike ISI relates to the deinactivation of I_T while the short, post-spike ISI relates to I_T activation. The cluster at the bottom left represents the spikes within the burst, each spike falling between successive short ISIs. The spikes at the top left are the last spikes in a burst, the long interspike interval following the spike the result of the return inhibition from the RE cell.

To characterize the output response of the TC cell, I define a criteria for classifying burst and non-burst events, based on the data in Figure 5.4 and similar to the criteria

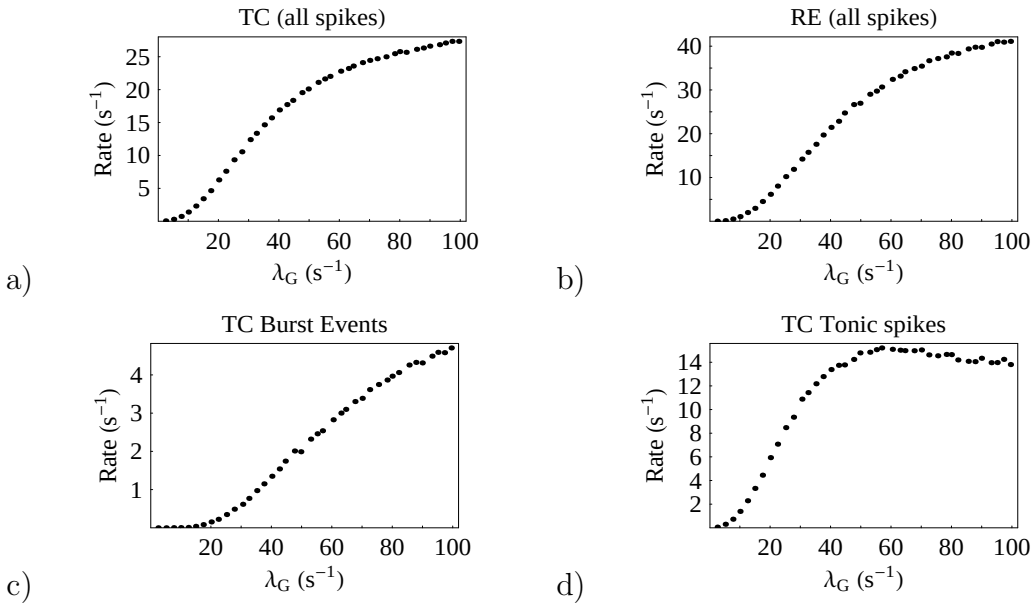

Figure 5.5: System Response to Retinal Input

These plots show the frequency of events for the TC-RE pair in response to retinal input.

in [83]. The initial spike in a burst is distinguished by its surrounding interspike intervals: a long period of quiescence (in this case, $>$ 100ms) followed by a very short interspike interval ($<$ 3ms). Once the start of the burst has been identified, all successive spikes within 10ms of each other are considered part of the burst, to account for expanding ISIs as I_T inactivates. All remaining spikes not classified as part of a burst are then considered tonic spikes.

Figure 5.5 plots the output frequency versus input Poisson rate of the TC and RE cells, as well as the division of the TC data into burst and tonic modes, using this criteria. At low input rates, the relay neuron responds only in tonic mode. Bursts cannot exist due to lack of inhibition from the RE cell. As the input rate rises, eventually the retinal input is able to propagate through the geniculate filter

and the reticular cell begins to fire. This increases the likelihood of the occurrence of sufficient inhibition to deinactivate I_T, and soon, around an input rate of 20Hz, bursts begin to emerge. After this point, burst frequency increases with the input rate, until eventually the bursts begin to dominate the output spike train, causing a decline in the tonic activity.

5.3 Modelling the Retinal Input Response

To model the activity of both neurons, I begin by defining the output state of the TC cell—at any given time—as being either burst or tonic. This division makes sense since the input/output relationship is dramatically different between the two modes. In tonic mode, the output rate of the cell is strongly dependent on the input rate. In burst mode, however, the burst response is very consistent and less dependent on the input: An extended period of inhibition deinactivates I_T and a second input triggers a burst. RE spikes are classified according to the TC cell state: Spikes caused by TC cell bursts are defined as RE bursts while spikes caused by tonic TC inputs are defined as RE tonic spikes.

Thus, I define the activity of each of the cells as follows:

$$\begin{aligned} f_{TC} &= f_{Ts|nb}(\lambda_G)\ \ (1 - P_b) + N_{Tb}\, f_{b|b}\, P_b \\ f_{RE} &= f_{Rs|nb}\left(f_{Ts|nb}\right)\ \ (1 - P_b) + N_{Rb}\, f_{b|b}\, P_b, \end{aligned}$$

where $f_{Ts|nb}$ and $f_{Rs|nb}$ are the responses of the relay and reticular cells (respectively) in tonic mode (shortened to f_{Ts} and f_{Rs} from hereon in), λ_G is the retinal (Poisson) input rate, P_b is the probability of a burst, N_{Tb} is the average number of TC cell spikes in a burst, N_{Rb} is the average number of RE spikes in response *to a TC burst* and $f_{b|b}$ is the frequency of burst events given the cell is in burst mode. Since the structure of the bursts does not change, $f_{b|b} = 1/\Delta_b(\lambda_G)$, where $\Delta_b(\lambda_G)$ is the interburst interval (IBI): the pre-burst inhibition plus the burst itself. Thus, $f_b = P_b/\Delta_b(\lambda_G)$, and

$$f_{TC} = f_{Ts}(\lambda)\ (1 - P_b) + N_{Tb}\, f_b \tag{5.1}$$

$$f_{RE} = f_{Rs}(\lambda)\ (1 - P_b) + N_{Rb}\, f_b. \tag{5.2}$$

5.3.1 Burst Mode

Figure 5.6(a) plots the first order kernel for burst events for the 40Hz input. The initial peak represents bursts that occurred immediately after the input spike; that is, the input spike *triggered* the burst following I_T deinactivation. The negative section after this peak represents a period of time where bursts are less likely to occur, due to the fact that I_T is incapable of sufficiently deinactivating in the time after the arrival of the input (which depolarizes the cell). The smaller peak represents bursts occurring subsequent to a deinactivation period following the input spike. In other words, the input spike belongs to a sufficiently strong retinal input that propagates to the reticular cell and generates enough feedback inhibition to deinactivate I_T. This suggests there are two components to a burst response: a *primer* and a *trigger*.

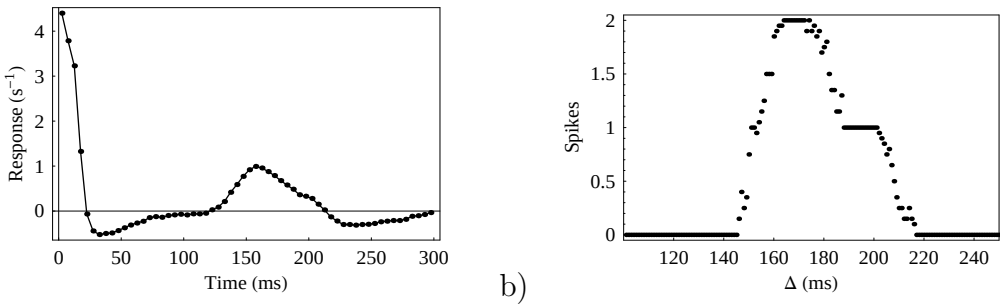

Figure 5.6: Burst Response

a) First order kernel for burst events. The first peak represents bursts that are triggered immediately by the input spike at t=0ms. The negative portion following the peak represents periods where bursts are unlikely to occur, due to insufficient deinactivation from the time of the input spike. The smaller, wider, bump represents bursts that occur after I_T deinactivation, suggesting the input spike belongs to retinal input that causes enough RE inhibition within the TC cell to deinactivate I_T. b) Average response (over 20 trials) versus retinal trigger position after an initial input (at t=0ms) that deinactivates I_T. If the spike arrives too early, the excitation is lost in the reticular inhibition. If the spike arrives too late, then I_T will have inactivated.

Once I_T has been deinactivated, the timing of the trigger is very important, as demonstrated in Figure 5.6(b). At t=0ms, a strong retinal input deinactivates I_T via RE inhibition. The cell responds only when the trigger—a single spike—arrives within a small window after I_T has deinactivated. If the trigger arrives too soon, the spike is lost in the feedback inhibition; too late, and I_T inactivates.

I define the probability of a burst event as dependent on the mutual occurrence of two independent events:

$$P_b = P_R P_T. \tag{5.3}$$

where P_R is the probability of inhibition that sufficiently deinactivates I_T and P_T is the probability of a retinal input arriving within the trigger window. Even though the inhibition derives from reticular axons, it is the activity in the thalamic layer that drives the reticular cells, and so I define P_R in terms of the probability of sufficient activity in the TC cell layer. This level of activity occurs in two forms: either as a TC cell burst or—absent a burst—a high-frequency response to a strong retinal input. Equation 5.3 becomes

$$P_b = (P_b + P_P (1 - P_b)) P_T,$$

where P_P is the probability of sufficient TC cell activity by retinal inputs. Rearranging,

$$P_b = \frac{P_P P_T}{1 - (1 - P_P) P_T}. \tag{5.4}$$

P_T, as defined above, is the probability of a retinal input arriving within the trigger window. I also define P_P in a similar manner; that is, as a probability based on the arrival of the sufficient retinal inputs within a defined window. Thus,

$$\begin{aligned} \mathrm{P_P} &= \mathrm{P}\,[\,\mathrm{N_r}, \Delta_\mathrm{r}, \lambda_\mathrm{G}\,] \\ \mathrm{P_T} &= \mathrm{P}\,[\,\mathrm{N_g}, \Delta_\mathrm{g}, \lambda_\mathrm{G}\,] \end{aligned}$$

where $\mathrm{P}\,[\,\mathrm{N}, \Delta, \lambda\,]$ is the probability of seeing N or more spikes in a time window Δ with a Poisson spike train of rate λ. Mathematically,

$$\mathrm{P}\,[\,\mathrm{N}, \Delta, \lambda\,] = 1 - \sum_{i=0}^{\mathrm{N}-1} \frac{(\lambda\Delta)^i}{i!}\, \mathrm{e}^{-\lambda\Delta}. \tag{5.5}$$

The time window Δ captures the temporal dynamics involved for the event: for $\mathrm{P_P}$, Δ depends on the synaptic time constant, while for $\mathrm{P_T}$, Δ depends on the dynamics of the T channel (as seen in Figure 5.6(b)). N represents (approximately) the minimum number of retinal spikes necessary for the event to occur. This value defines the shape of the probability curve, or how 'sharp' the dependence of the probability is on the input frequency. For $\mathrm{N} = 1$, the probability rises as $(1 - \exp\,[-\lambda\,\Delta])$, as the exponential interspike interval distribution means—even at low frequencies—there is a probability of seeing an ISI less than Δ. As N increases, the variability between ISIs is averaged out among the spikes. As $\mathrm{N} \to \infty$, $\mathrm{P}\,[\,\mathrm{N}, \Delta, \lambda\,]$ becomes a Heaviside function at the input frequency $\lambda = 1/\Delta$.

This representation is only an approximation of the dynamics. A more accurate description would involve a separate Δ for each integer number of input spikes, since more spikes would increase the duration of excitation from the synapse and result in a larger 'window'. However, for the sake of simplicity, I define the probability using

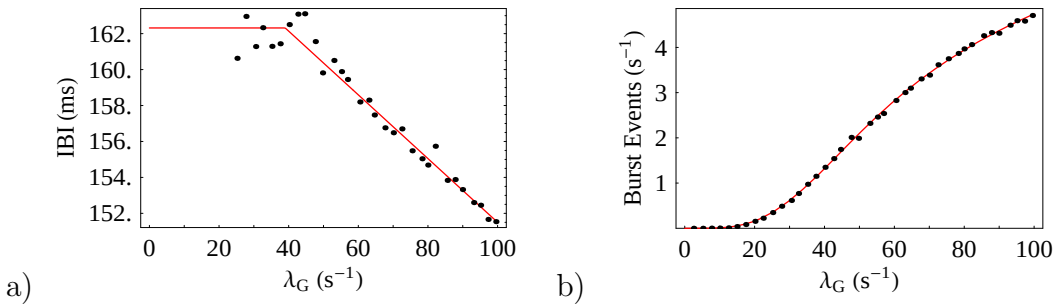

Figure 5.7: Modelling Burst Frequency

a) Change in the interburst interval versus input frequency (fit parameters). b) Data fit to burst frequency. The fit parameters are $N_r = 3.51$, $\Delta_r = 55.7$ms, $N_g = 1$ and $\Delta_g = 13.4$ms.

only a single Δ.

Defining P_P in terms of the retinal input rate λ_G may be confusing since it is the reticular spikes that cause inhibition in the TC cell. However, the output of the RE cell is not Poisson, and as such the calculation of probabilities using reticular activity is much more difficult. Instead, I use the randomness of the retinal inputs to simplify the calculation since it is the retinal inputs—via the TC cell—that drive the reticular activity.

Using Equation 5.4, the equation for the burst rate is

$$f_b = \frac{1}{\Delta_b(\lambda_G)} \frac{P[N_r, \Delta_r, \lambda_G] P[N_g, \Delta_g, \lambda_G]}{1 - (1 - P[N_r, \Delta_r, \lambda_G]) P[N_g, \Delta_g, \lambda_G]}.$$

As mentioned previously, $\Delta_b(\lambda_G)$ is the interburst interval (IBI), which includes the deinactivation period and the length, in time, of the burst. Assuming that the shape

of the inhibition remains consistent within a burst event, the change in average input current—due to the input rate (see Section 5.3.2 below)—affects the point at which the cell rebounds from its hyperpolarized level. Figure 5.7(a) plots data showing interburst interval versus input frequency. At higher input rates, the IBI changes linearly with λ_G. At lower frequencies, the IBI remains constant because of the inactivation dynamics of I_T.

Once I have calculated the dependence of the interburst interval on the input, I fit Equation 5.4 to the data (Figure 5.7(b)). What do the fit values represent? Loosely translated, the probability of a burst is dependent on the occurrence of three or more retinal spikes ($N_r = 3$) within a window of 55ms, followed by one or more spikes ($N_g = 1$) within a trigger window of 13ms. Recalling that it requires two close spikes to define a burst, this trigger window width is comparable to the results in Figure 5.6(b).

5.3.2 Tonic Mode

The next step is to calculate the tonic response function of both the TC and RE cells ($f_{Ts}(\lambda)$ and $f_{Rs}(\lambda)$ respectively). The data in Figure 5.5(d) does not represent f_{Ts}, rather it represents the mean response for the *whole* stimulus period, as opposed to the mean response for the total time in the tonic state. However, since I have already solved for P_b, I can use the tonic term in Equation 5.1 to explicitly calculate the data for $f_{Ts}(\lambda)$. Through a similar procedure for RE cell, I can calculate $f_{Rs}(\lambda)$, and then $f_{Rs}(f_{Ts})$. The tonic data for both cells are plotted in Figure 5.8.

To represent the synaptic dynamics, I need to calculate the average output synap-

tic current for a given Poisson input rate. I make two assumptions in this procedure: 1) The output of the synaptic cleft circuit (Section 4.1.2.1) is an ideal pulse; 2) The width of that ideal pulse is less than most interspike intervals. With these assumptions, synaptic dynamics are linear (Equation 4.2), and I can calculate the average output current by determining the total output charge per input spike. I begin by integrating the output current during and after the pulse:

$$\begin{aligned}
\mathrm{Q_{spk}} &= \mathrm{Q_{\Delta}} + \mathrm{Q_{P}} \\
&= \int_{s=0}^{\Delta} \mathrm{I_{\Delta}}\left(s\right) \mathrm{d}s + \int_{s=\Delta}^{\infty} \mathrm{I_{P}}\left(s\right) \mathrm{d}s \\
&= \int_{s=0}^{\Delta} \mathrm{P}\left(1 - \exp\left[-\frac{\mathrm{s}}{\tau}\right]\right) \mathrm{d}s + \int_{s=\Delta}^{\infty} \mathrm{P}\left(1 - \exp\left[-\frac{\Delta}{\tau}\right]\right) \exp\left[-\frac{\mathrm{s}-\Delta}{\tau}\right] \mathrm{d}s \\
&= \mathrm{P}\left(\Delta - \tau\left(1 - \exp\left[-\frac{\Delta}{\tau}\right]\right) + \tau\left(1 - \exp\left[-\frac{\Delta}{\tau}\right]\right)\right) \\
&= \mathrm{P}\,\Delta
\end{aligned}$$

Therefore, for a Poisson spike train of rate λ,

$$\hat{\mathrm{I}}_{\mathrm{syn}} = \Delta\,\mathrm{P}\,\lambda \tag{5.6}$$

Thus, the average output current of the synapse is proportional to the input Poisson rate. I use this equation to represent the retinal synapse, since the output feeds directly into the membrane of the neuron (Figure 5.2). But the output of the thalamoreticular synapse and the cortical synapses pass through a series transistor

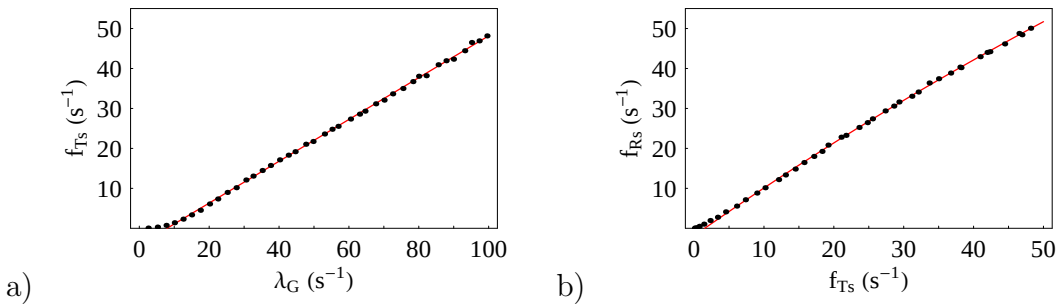

Figure 5.8: Tonic Mode Frequency Transfer Functions

a) Output TC frequency versus input frequency. Fit parameters for Equation 5.8: $\beta_{gt} = 0.523$ and $\theta_T = 4.16$Hz. b) Output RE frequency versus input TC frequency. Fit parameters for Equation 5.9: $\beta_{tr} = 1.23$, $\alpha_{tr} = 2.97$ms, $\theta_R = 1.86$Hz.

that limits the current levels (Figure 5.2). Thus, for these synapses, I insert Equation 5.6 into Equation A.3:

$$\begin{aligned} \hat{I}_{syn} &= \frac{\Delta P \lambda I_{lim}}{\Delta P \lambda + I_{lim}} \\ &= \Delta P \frac{\lambda}{\Delta \frac{P}{I_{lim}} \lambda + 1} \\ &\equiv \beta \frac{\lambda}{\alpha \lambda + 1} \end{aligned} \tag{5.7}$$

For each of the IF neurons, the output frequency is proportional to the input current. Using the above relationships for input Poisson rate to synaptic current, I represent the output tonic frequency of each cell as a function of its input frequencies:

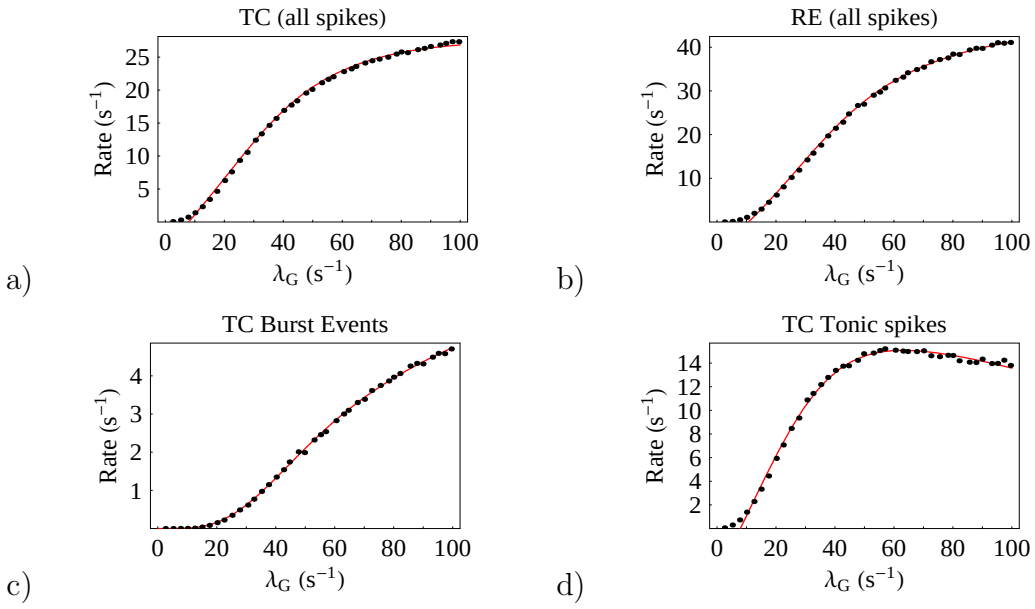

Figure 5.9: Model Fit

Data and fits to the retinal input response. Complete fit parameters: $N_r = 3$, $\Delta_r = 55.7$ms, $N_g = 1$, $\Delta_g = 13.4$ms, $N_{Tb} = 2.80$, $N_{Rb} = 5.73$, $\beta_{gt} = 0.523$, $\theta_T = 4.16$Hz, $\beta_{tr} = 1.23$, $\alpha_{tr} = 2.97$ms, and $\theta_R = 1.86$Hz.

$$f_{Ts} = \beta_{gt}\,\lambda_G - \theta_T \tag{5.8}$$

$$f_{Rs} = \beta_{tr}\,\frac{f_{Ts}}{\alpha_{tr}\,f_{Ts}+1} - \theta_R, \tag{5.9}$$

where θ is the rheobase of the cell (in units of Hz), and β_{gt}, β_{tr}, and α_{tr} are synaptic parameters (Equations 5.6 and 5.7). The fits to the tonic data are also plotted in Figure 5.8.

With equations calculated for both response modes, Figure 5.9 plots the complete

fit to the original data in Figure 5.5.

5.4 Modelling the Cortical Modulation

The influence of the cortical feedback is also probed using Poisson inputs; but since cortical inputs are incapable of driving the cells (see Section 5.1), I probe the influence of the cortical spikes using Poisson inputs at both the retinal and cortical synapses. To capture the full range of response, I perform two experiments: 1) I fix the retinal rate and sweep the cortical rate (column 1 in Figure 5.10); 2) I fix the cortical rate ($\lambda_X > 0$) and sweep the retinal rate (column 2 in Figure 5.10).

Like the retinal input, the cortical input also affects the number of bursts in the system (Figure 5.10(a)), but in a much weaker fashion due to its weaker synapses. There are two ways the cortical spikes influence bursting: 1) by enhancing the initial retinal input that deinactivates I_T, either through interactions in the TC cell or the RE cell; 2) by helping in triggering I_T. Thus, in the burst model, I include the feedback into Equation 5.4 as follows:

$$\begin{aligned} P_P &= P[N_{r1}, \Delta_r, \lambda_G]\ (\ 1 - P[1, \Delta_r, \lambda_X]\ )\ + \\ &\qquad P[N_{r2}, \Delta_{rx}, \lambda_G]\ P[1, \Delta_{rx}, \lambda_X] \qquad (5.10) \\ P_T &= P[N_{g1}, \Delta_g, \lambda_G]\ (\ 1 - P[1, \Delta_g, \lambda_X]\ )\ + \\ &\qquad P[N_{g2}, \Delta_{gx}, \lambda_G]\ P[1, \Delta_{gx}, \lambda_X], \qquad (5.11) \end{aligned}$$

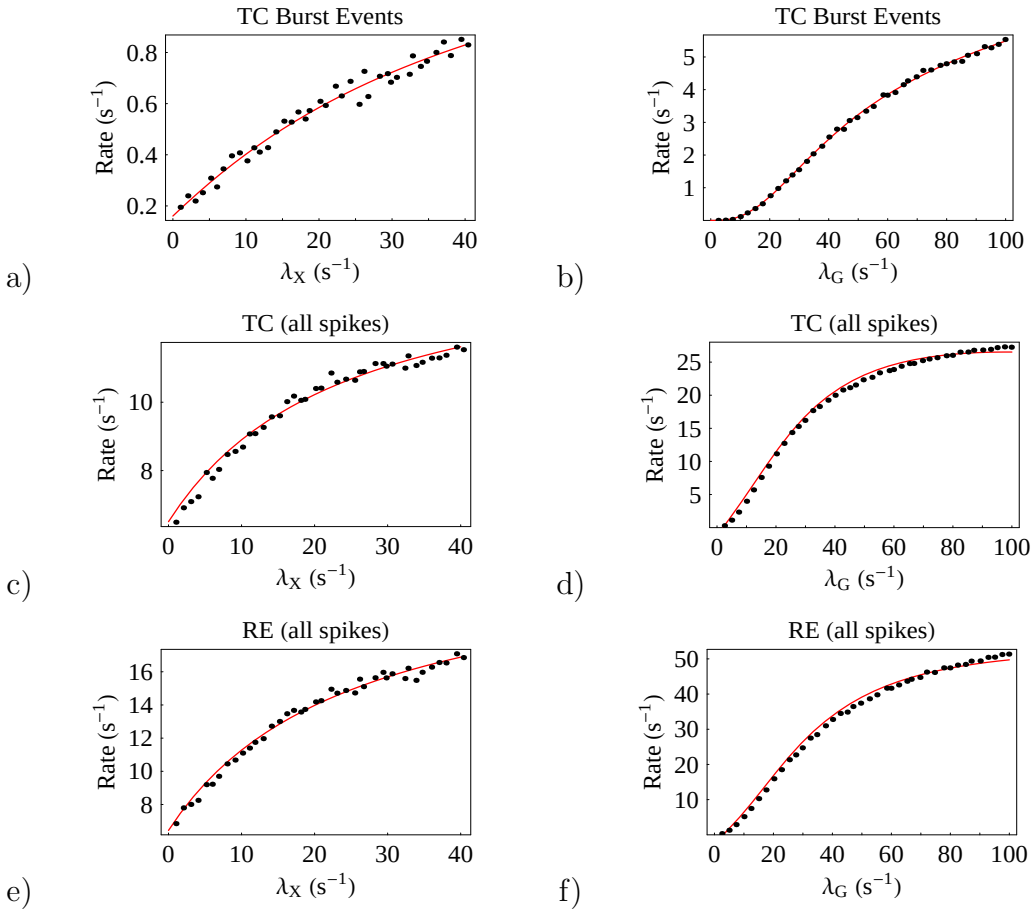

Figure 5.10: Cortical Feedback Response

These plot show the data relating to the effects of cortical feedback. In the first column (a,c,e), the retinal input is kept constant at $\lambda_G = 20$Hz and the cortical Poisson rate is swept to 40Hz. The second column fixes the cortical input rate ($\lambda_X = 30$Hz) and repeats the initial experiment of sweeping the retinal inputs. a,b) Burst response versus λ_X and λ_G. The fit parameters for Equations 5.10 and 5.11 in Equation 5.4 are $N_{r2} = 2.14$, $\Delta_x = 58.7$ms, $N_{g2} = 0.566$, $\Delta_{gx} = 14.4$ms. c,d) TC spike response (both burst and tonic spikes). e,f) RE spike response (all spikes). The fit parameters for Equations 5.13 and 5.14 are $\beta_{gxt} = 0.00049$, $\beta_{txr} = 0.00160$.

where $\mathrm{P}[\,\mathrm{N}, \Delta, \lambda\,]$ is defined by Equation 5.12 (see below). The first term represents the actions of the retinal input without any cortical input, and so the parameters for $\mathrm{P}[\,\mathrm{N_{r1}}, \Delta_{\mathrm{r}}, \lambda_{\mathrm{G}}\,]$ and $\mathrm{P}[\,\mathrm{N_{g1}}, \Delta_{\mathrm{g}}, \lambda_{\mathrm{G}}\,]$ are from the previous section. The second term represents the combined action of both inputs. Were the cortical synapses stronger, there would be an additional independent cortical term. However, since the coupled term sufficed, the independent cortical term was assumed to be negligible.

The original equation for $\mathrm{P}[\,\mathrm{N}, \Delta, \lambda\,]$ (Equation 5.5) defined the probability of an event as the occurrence of an integer number of spikes (or more) within a temporal window. With the addition of cortical inputs, the minimum number of retinal spikes depends on the number of cortical inputs. Thus, the values for $\mathrm{N_{r2}}$ and $\mathrm{N_{g2}}$ will likely not be constrained to integer values, but as an average over all the possible cortical inputs. Thus, to measure the cortical influence, I use the continuous form of Equation 5.5[110]:

$$\mathrm{P}[\,\mathrm{N}, \Delta, \lambda\,] = 1 - \frac{\Gamma[\,\mathrm{N}, \lambda\Delta\,]}{\Gamma[\,\mathrm{N}]}, \tag{5.12}$$

where $\Gamma[\,n, x\,] = \int_x^\infty t^{n-1} \exp[-t]\ \mathrm{d}t$ is the *incomplete Gamma function*, and $\Gamma[\,n\,] = \Gamma[\,n, 0\,]$ is the *complete Gamma function*. In this form, $\mathrm{N} \in \Re$.

Figure 5.10(a) and Figure 5.10(b) show the fits to the data. The fit parameters show that the cortical feedback reduces the threshold for the retinal inputs, as demonstrated by the lower number of spikes for the trigger ($\mathrm{N_{g2}} = 0.566$) and the initiation ($\mathrm{N_{r2}} = 2.14$) versus the retinal-only input case ($\mathrm{N_{g1}} = 1$ and $\mathrm{N_{r1}} = 3$ respectively).

For the tonic regime, the cortical feedback is incorporated into Equations 5.8 and

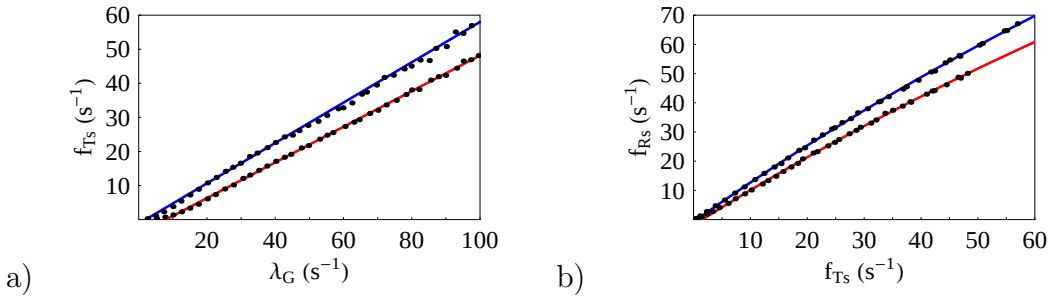

Figure 5.11: Slope Changes during Tonic Mode

a) TC cell response versus retinal input rate. b) Slope change for RE cell to TC cell input. For both plots, the red curve plots the response without cortical feedback, while the blue curve plots the response with cortical feedback intact, but fixed.

5.9 as follows:

$$f_{Ts} = \beta_{gt}\,\lambda_G + \beta_{xt}\frac{\lambda_X}{\alpha_{xt}\,\lambda_X + 1} + \beta_{gxt}\,\lambda_G\frac{\lambda_X}{\alpha_{xt}\,\lambda_X + 1} - \theta_T \quad (5.13)$$

$$f_{Rs} = \beta_{tr}\frac{f_{Ts}}{\alpha_{tr}\,f_{Ts} + 1} + \beta_{xr}\frac{\lambda_X}{\alpha_{xr}\,\lambda_X + 1} + \beta_{txr}\frac{f_{Ts}}{\alpha_{tr}\,f_{Ts} + 1}\frac{\lambda_X}{\alpha_{xr}\,\lambda_X + 1} - \theta_R. \quad (5.14)$$

Two additional terms are included into Equations 5.13 and 5.14: a simple cortical term and a term expressing a nonlinear interaction between the inputs. The simple cortical term, like the retinal inputs, reflects the cortical synaptic input into the IF neuron. The nonlinear term is not initially obvious, however, from Figure 5.11, it is clear that there is a change in the slope of the tonic response due to the addition of the cortical input.

This is surprising considering the inputs into the chip are separate synapses and the cell is a simple integrate and fire neuron. It is not clear, at the moment, the reason for this change in slope; further work would be required to verify this. However, for

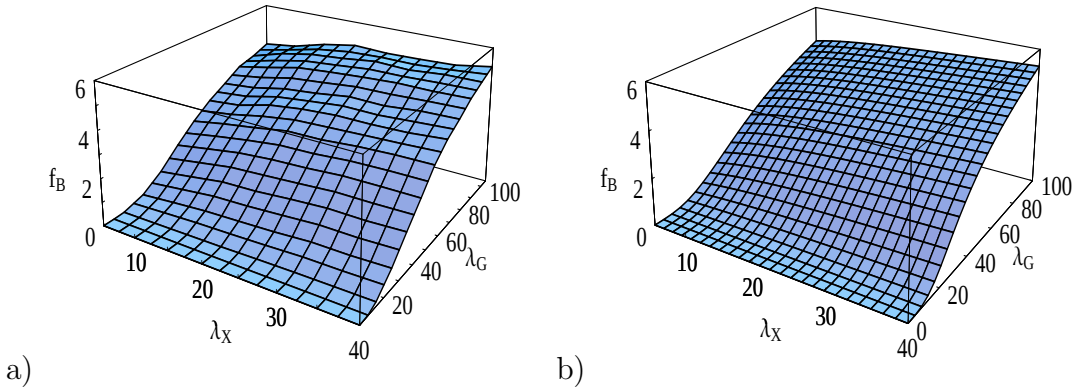

Figure 5.12: 2D Burst Rate Plot

Burst frequency over the full range of input retinal and cortical frequencies: a) data from chip; b) model fit to the data in (a).

simplicity, the extra term representing the product of the inputs is sufficient to capture the effects.

With these equations, I fit the rest of the data in Figure 5.10. Figure 5.12 shows a three-dimensional plot of the response—both data from the chip and the model fit—over the whole range of retinal and cortical frequencies.

5.5 Interpreting the Model

For retinal inputs, the response of the two cell system (Figure 5.9) shows that bursts are more likely to occur at higher rates, where greater TC activity translates into increased inhibition from RE cells for I_T deinactivation. This is further demonstrated in Figure 5.13(a), which plots the probability of each of the response modes with respect to the input Poisson rate. At low frequencies, the cell responds completely

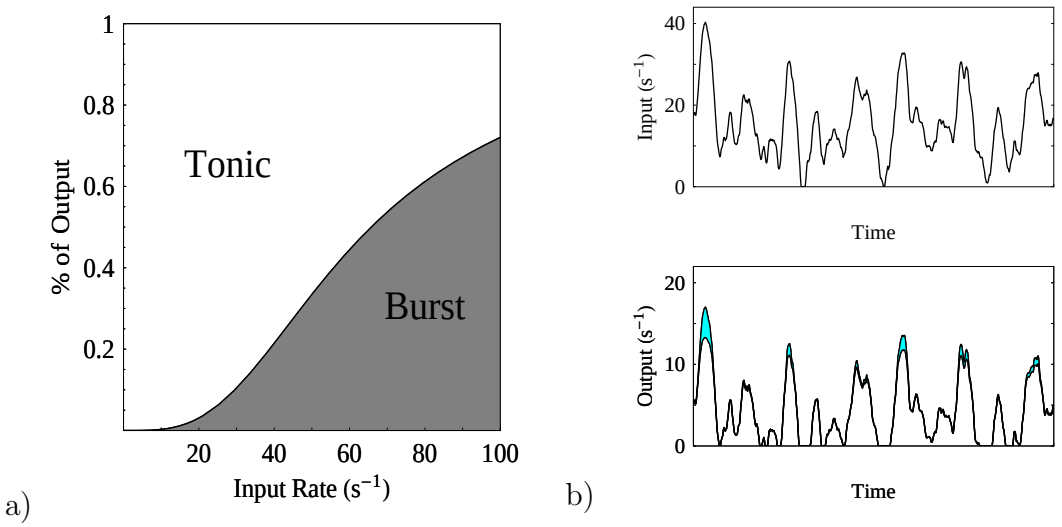

Figure 5.13: TC Cell Response

a) Proportion of time the output spike train is in burst or tonic mode with respect to the input rate. b) TC cell output rate (bottom) to a generated retinal input rate (top). Input generated by filtering Gaussian random noise (mean and variance of 15Hz) with a biphasic linear kernel. The TC cell output is calculated using Equation 5.1. The shaded portion in cyan represents the proportion of the output spike train that is burst.

in tonic mode. As the input rate increases, so does the probability of bursts. This suggests that bursts signal strong features in the input.

Figure 5.13(b) demonstrates this with a simple example. The top figure plots the input into the system: a random, filtered rate function $\lambda_{\mathrm{G}}(t)$. The bottom figure plots the output $\mathrm{f}_{\mathrm{TC}}(\lambda_{\mathrm{G}})$, generated using Equation 5.1, with the cyan and white regions representing the probability of the output for burst and tonic modes (respectively), based on Figure 5.13(a). For most of the response, the cell remains in tonic mode; only at the strong peaks is there a possibility of a burst.

What advantage does I_T add to the response? In terms of mean response, not much. Figure 5.14 shows, up to $\lambda_G = 50$Hz, that the silicon cell and a cell responding only in tonic mode have similar output functions. The difference, however, lies in the structure of the response. Recall that I_T requires hyperpolarization; the burst response, therefore, would be high-frequency clusters of spikes around longer periods of silence. The tonic response—assuming the same number of spikes—would be more spread out and of a much lower frequency. Even if the RE inhibition helped shape the temporal shape of the tonic cell spikes, the response still would not be able to achieve the higher frequencies that I_T can (Figure 5.4(b)).

How does the cortical feedback influence the response? Increasing the cortical rate clearly increases the number of bursts in the cell's output (Figure 5.15(a)). But the effect is more than a simple linear shift in the response, which might be expected if the burst increase was only the result of increased excitation in the TC cell. The cortical input also changes the sensitivity of the burst output to retinal inputs (Figure 5.15(b)).

Figure 5.16 plots the same set of figures as in Figure 5.13, except with the addition of a cortical input at a fixed rate of 40Hz. As already demonstrated in Figure 5.15, the cortical input increases the probability of bursting in response to the retinal input, shown in magenta in Figure 5.16(a). In general, the addition of the cortical input raised the excitability of the system, seen through a general increase in mean output response (Figure 5.16(b)). Peaks in Figure 5.13(b) that demonstrated some probability of bursting now had a greater likelihood of bursting. In addition, weaker inputs that passed through initially in tonic mode now demonstrated a probability of bursting. The cortical input, then, acts to enhance the response of the system, not only through an increase in the tonic firing rate, but also in an enhancement by

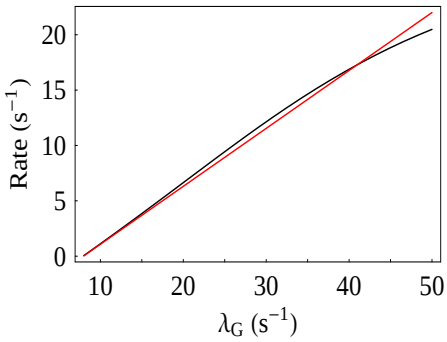

Figure 5.14: Mixed Mode Versus Tonic Response

This figure plots Equations 5.1 and 5.8, comparing the mean response of a cell possessing I_T (black) with a cell only in tonic mode (red).

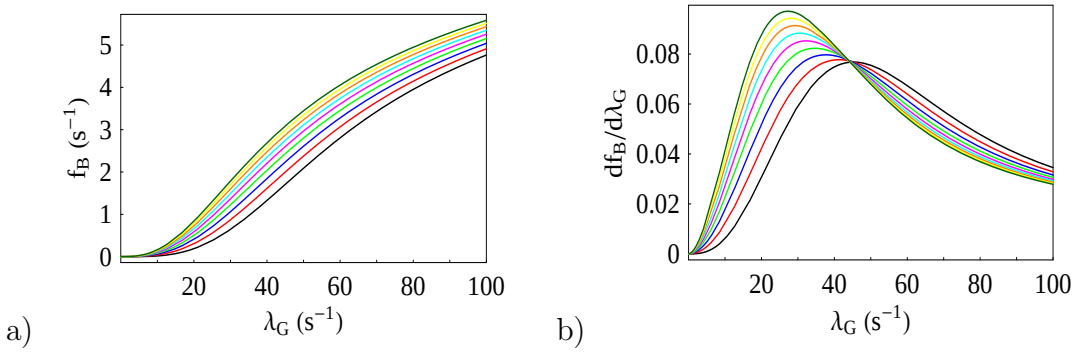

Figure 5.15: Cortical Modulation of Bursts

a) Burst event frequency versus retinal input rate λ_G for different cortical rates. λ_X varies from 0Hz (black) to 40Hz (dark green) in steps of 2.5Hz. b) Derivative of f_b with respect to λ_G.

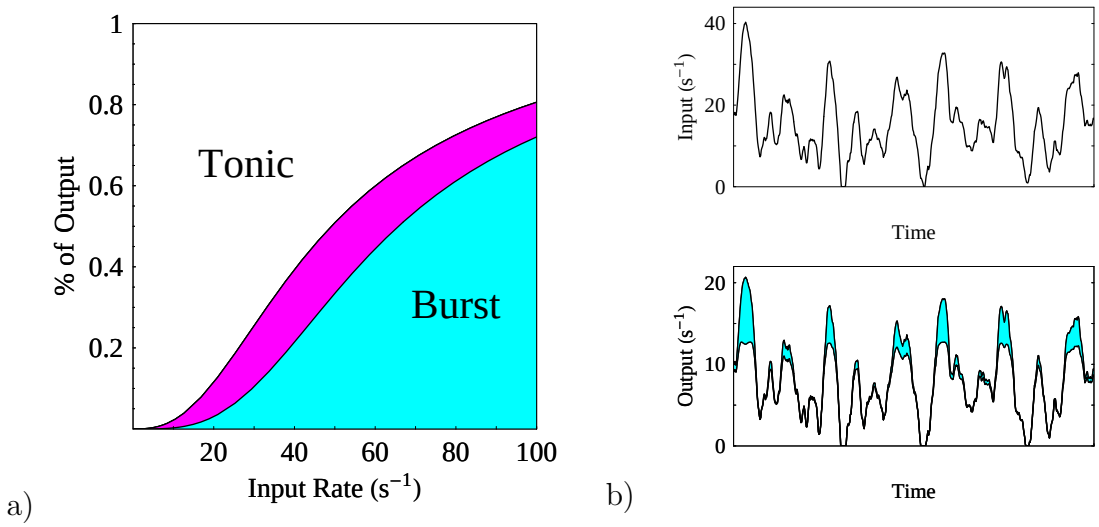

Figure 5.16: TC Cell Response With Cortex

Same setup as in Figure 5.13, with the addition of a fixed cortical rate $\lambda_X = 40$Hz. a) Division of the output spike train into burst and tonic modes with respect to the input retinal rate. Cyan represents the burst division from Figure 5.13; magenta represents the increase in the burst probability due to cortical enhancement. b) New TC cell output rate (bottom) to the same generated retinal input rate (top) from Figure 5.13. The output response of the silicon model (Equation 5.1). The shaded portion in cyan represents the proportion of the output spike train that is burst.

recruiting I_T.

5.6 Discussion

In this chapter, I studied the interaction between two silicon neurons, representing cells from the lateral geniculate nucleus and from the reticular nucleus. I had two goals: 1) I wanted to probe how the feedback inhibition from the RE cell influenced

the role of the T channel; 2) I wanted to study how the cortical feedback can affect the dynamics between the two cells. To accomplish this, I used Poisson spike trains of varying frequency at both the retinal and cortical synapses.

Bursting behavior in the TC cell was strongly dependent on sufficient inhibition from the RE cell. Absent any cortical inputs, the TC cell provided the only source of excitation for the RE cell, and thus the inhibition occurred only after a strong retinal input. In addition, a second input—a trigger—was necessary to release the burst. This trigger was temporally constrained to a small window in time: too soon, and the trigger would be lost in the feedback inhibition; too late, and I_T will have inactivated.

At low input frequencies, insufficient RE activity kept the TC cell in tonic mode. As the input rate increased, so did the output rate of the TC cell, and thus the reticular rate. Eventually, enough feedback inhibition deinactivated I_T and the TC cell exhibited both tonic and burst responses. As the input rate increased further, the TC cell entered more of an oscillatory response as the cell elicited successive bursts.

Cortical inputs, synapsing to both cells, affected burst generation by increasing the level of input current, and thus the excitability, of the system in three places:

1. In the TC cell, during the initial, pre-inhibitory input.
2. In the RE cell, during the response to the TC cell.
3. In the TC cell again, during the trigger phase.

Since the cortical synapses were much weaker than retinal synapses, they could only enhance the response of the cells to retinal inputs as opposed to driving the cells themselves. Thus, they had the effect of reducing the threshold of activation in each

of these stages. As a result, the cortical input shifted the probability of bursting to lower retinal frequencies.

With the probability of bursting increasing with input intensity, I_T acts as a nonlinear amplification of strong inputs. Though the mean output rate was similar between a TC cell with and without I_T (Figure 5.14), the structure of the spike train in both instances would be significantly different. With I_T, the spikes are grouped into higher frequency bursts surrounded by periods of quiescence corresponding to the RE inhibition. Without I_T, the cell is incapable of attaining the high frequencies achievable with I_T, and so the spikes are more 'spread out' in their response. This may have dramatic effects on the cortical cells. For depressing synapses, such as thalamic synapses to GABAergic interneurons in the rabbit somatosensory cortex[137], the mean rate of the thalamic cells kept the synapses in a constant state of depression. Thus, the inhibitory period, crucial for I_T deinactivation, helps the synapse recover from depression, making the cell respond strongly to the initial spike in the burst. For synapses demonstrating facilitation, such as in simple cells in the cat[144], spikes arriving within 15ms of the previous spike are more effective at eliciting a response, making bursts very effective at driving these cortical cells. Bursts are also more reliable responses at unreliable synapses[79]. In addition, high-frequency trains of spikes are better than single spikes at activating widespread recurrent activity in cortical layers[9].

I_T need not cause an all-or-none burst; characterizing the response in terms of bursts was necessary as it was the only way I could extract response changes of I_T at the spike level[83]. But different levels of I_T could exist corresponding to different amplitude or duration of inhibition from the RE cell. Smaller I_T response would mean smaller synaptic enhancement at the cortical level, either in a decreased removal of

synaptic depression—because of a smaller deinactivation duration—or decreased facilitation due to less spikes in the burst (or even lower frequency within the burst). What's interesting is that the burst response affects both synapse types simultaneously. A tonic response could also take advantage of both these synaptic effects also by following a quiet period with a strong tonic response. However, that requires two separate effects—silence followed by strong input—whereas I_T automatically links the length of the silence with the strength of the following enhancement.

Another role for this temporal linkage is also suggested by the structure of the burst model (Equation 5.3). There, the probability of a burst is determined by the probability of two signals: an inhibitory input that deinactivates I_T and a positive input that activates it. Another way to consider this: a burst indicates the presence of these two successive events. In the data in this chapter, the source for the two signals was (primarily) the retinal inputs; thus, as the input rate increased, the probability of each event also increased, raising the number of bursts. However, the axonal divergence between the TC and RE layers, as well as influence of the cortical input, means the two signals may be completely independent of one another (i.e., from different sources). As such, the presence of a burst could signal the correlation between these two signals.

This linkage is the result of a couple of assumptions within my setup. First, that the TC cell rests sufficiently depolarized such that I_T is inactivated. This requirement forces the burst to depend on the presence of sufficient inhibition from the reticular nucleus. The other assumption involves the lack of rebound from inhibition. Many studies have focussed on the rebound burst, assuming that once deinactivated, the cell automatically causes a burst after the inhibition has been removed[131, 141, 116]. Rebound bursts depend on a number of factors. The first is the level of deinactivation:

Lower levels of deinactivation may mean I_T is too weak to overcome the rheobase of the cell. The second factor is whether—or how far—the resting potential is in the activation range of the T channel (Figure 3.1). The final factor is the level of the passive conductance within the cell membrane. Increasing the membrane conductance, to mimic *in vivo* conditions, reduces the possible range of rebound bursts within thalamic cells[28].

These assumptions differentiate my model from other models of I_T processing in the awake thalamus. Many models assume external control of the resting potential of thalamic cells[120, 78, 139, 130], possibly through either metabotropic receptors from the cortex[95, 39] or through inputs from the parabrachial region[84]. As seen in Chapter 4, shifting the resting potential of the cell dramatically alters the response properties of the cell, giving external control of the type of geniculate filter for the desired processing, such as detection of unattended strong stimuli[120], temporal decorrelation at the timescale of I_T dynamics[139], or temporal filtering[100, 130]. However, as already discussed in Chapter 2, the timescale of these resting potential interactions are too slow too account for rapid processing necessary in the human visual system.

The idea of the reticular nucleus deinactivating I_T in the thalamus to strengthen sensory signals to the cortex is not new. This is part of the premise for Crick's "searchlight hypothesis"[15]. In his theory, the reticular nucleus acts to guide the focus of attention to different areas of the retinotopic field, deinactivating I_T inside the searchlight and weakening signals outside of it. Once I_T inactivates, silencing the current area of attention, the searchlight moves to the next active area of visual space, repeating the process. Cortical input influences the position of the searchlight, and can also provide the context for the search. While Crick places more emphasis

on the role of the reticular nucleus in shifting attention, these ideas have similarities to those suggested by my results.

My results support the hypothesis that cortical feedback controls attention in analyzing the visual field. FMRI studies on the LGN in humans demonstrate increased neural responses to attended stimuli, attenuated responses to unattended stimuli, and increased baseline activity in the absence of visual stimulus[103]. These easily agree with the results I have demonstrated here. The cortical feedback clearly increased the response to the visual input (compare Figure 5.9(a) to Figure 5.9(d)). Since I only studied a single TC-RE pair, I was unable to demonstrate an attenuation of response to unattended stimuli. But it is easy to imagine that within a population of neurons, the attenuation could occur because of the spread of RE inhibition from the attended spatial area, or possibly because of the loss of cortical input due to limited attentional resources[76]. Increase in the baseline activity, in my system, would occur if I strengthened the corticothalamic synapses to allow the cortical inputs to cause spike activity in the TC cell.

There are a number of experimental results from interactions between real TC and RE/PGN cells that, at first glance, invalidate this model. I_T deinactivation through inhibition can occur through $GABA_A$[141, 148] and/or $GABA_B$[60, 16] receptors. Both require high-frequency input from the PGN—the $GABA_B$ response requiring a prolonged burst—either as a burst or a strong tonic response[116, 70]. However, TC cell inputs onto depolarized PGN cells demonstrate a reduced excitatory drive such that a TC cell burst registers as an extra spike in the PGN cell response in tonic mode [69]. A response to a TC tonic output would thus be even less. It would seem impossible for a real TC-RE pair to interact in the fashion demonstrated by my results, as a single TC cell cannot cause sufficient RE activity to deinactivate I_T in

itself.

However, a *population* of TC cells could produce a strong enough input drive to cause the RE cell to fire rapidly, which is possible considering the steep *f-I* curve of the reticular neurons[8]. Another possibility is that the RE activity is from a population of RE cells, which may then provide a prolonged $GABA_A$ activity or strong synchronous activity to cause a $GABA_B$ response in the TC cell[116]. Regardless of which population, and it is possible it could be both, the point is that the restrictions on the individual cells force the stimulus to have some *spatial* structure to it. This is the focus of the next chapter.

Chapter 6

TC-RE Network

The two cell system of the previous chapter provided some interesting insight into the occurrence of bursts in the relay neuron. In and of itself, that system was not representative of actual interactions between two real cells, for reasons brought up in the discussion. However, the response can be considered as encompassing the activity of the population.

Two components were necessary for the presence of a burst: sufficient inhibition to deinactivate I_T and sufficient depolarization to activate it. In the previous chapter, I modelled the inhibition as driven from the TC cell, and influenced by the cortical input. However, the network properties of the TC-RE layer add a *spatial* dimension to the whole situation. Thus, to understand the role of the T channel within the system, it is important to understand the response of the inhibitory component that deinactivates the channel.

The goal of this chapter is to discuss those results in the context of the LGN-PGN

network response to visual stimuli. Unfortunately, due to problems within the chip, related to the leakage currents discussed in Chapter 3, I am only able to perform simple population experiments. The first section presents some population results from my silicon chip, demonstrating the dependence of the burst response on the stimulus bar length, and the changes in the response due to varying patterns of cortical feedback. Following that I speculate on the function of the thalamocortical system (which includes the reticular nucleus) through the action of the various components, including I_T. Finally, I conclude with a few comments on the advantages of using a silicon model.

6.1 Chip Results

Figure 6.1 shows the network organization—both the physical layout and the synaptic organization—on the silicon chip. The chip consists of a hexagonal array (Figure 6.1(a)); each node of the grid consists of four relay cells and a reticular cell. Each relay cell excites the reticular cell, which, in turn, sends inhibition back to all of them. Retinal inputs form synaptic circuits (excitatory and inhibitory) with the relay cells to generate ON or OFF, lagged or nonlagged cells, although in my experiments I only use the nonlagged ON cells. Cortical inputs into the node excite all five cells equally.

Diffusor networks (Appendix A.3) implement axon divergence. The output of the diffusor is a spatially decaying exponential centered topographically at an input spike. Since both the thalamic and reticular layers are retinotopically organized, the strongest influence is between two cells sharing the same topographic location. Through voltage biases I can adjust the space constant of the exponential decay.

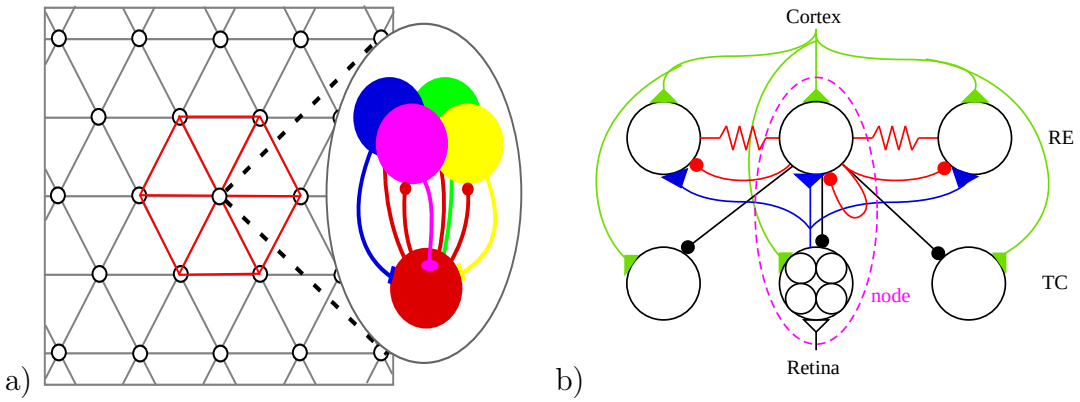

Figure 6.1: Network Connections

This figure shows the network connectivity built into the chip. a) The organization of the chip is a hexagonal grid, with each node consisting of 5 cell types: ON and OFF, lagged and nonlagged relay neurons plus a reticular cell. Diffusor networks (Section A.3) implement all spatial network connections. Each node within the 2D hex grid represents a node (e.g., n_i) in the 1D diffusor in Figure A.2. b) 1D layout of network connections, with triangles and circles representing excitation and inhibition respectively. The dashed circle indicates all of the cells within a single node in the 2D hex grid. There are four diffusor arrays within the chip: 1) Relay cell excitation of reticular layer (blue triangles); 2) reticular inhibition of both thalamic (black circles) and reticular (red circles) layers; 3) cortical excitation of both layers (green triangles); 4) gap junctions between reticular cells (red resistor symbols). Retinal inputs drive only the relay neurons at the same spatial location.

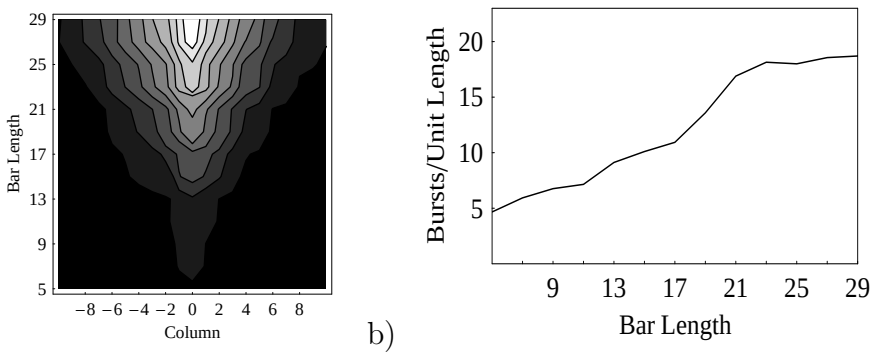

Figure 6.2: Influence of Reticular Population Activity on I_T Activation

a) Contour plot of horizontal spread of reticular activity from a central bar of varying length. Horizontal axis: Column position with respect to bar position (column 0). Vertical axis: Length of bar, with one unit of length equal to one neuron. The data was collected by presenting each bar length to 46 columns on the chip and measuring the spread in activity within each column. The input was a short 100ms spike train at 50Hz. The grayscale range (0-1) maps to total number of spikes in a column (0-25). b) Average number of bursts as a function of input bar length. Each neuron in the bar received independent Poisson spike trains with a rate of 40Hz.

Retinal inputs were the sole set of axons that did not pass through a diffusor before entering a cell layer. Since retinal axon convergence can be as low as one (see Section 2.1), I implemented a one-to-one retinal axon to TC cell connection. All other layer-to-layer connections (TC to RE, RE to TC and cortical afferents) use a diffusor circuit to implement axon fan-out.

Since PGN cells show increasing response with increasing stimulus size[35], I study the influence of the network on bursting by inputting a visual "bar" stimulus of varying lengths, but of a fixed width (one column in my neuron array). Given the divergence from the TC to RE and RE to TC cell layers, increasing the bar length

will increase the activity within the reticular population, which—since it generates more reticular inhibition—should increase the number of recorded bursts.

Figure 6.2(a) plots the reticular activity within each column of the chip around the location of the bar (column 0). I present the bar to each column within the chip (48 columns total) to reduce the effects of mismatch. As the length of the bar increases, measured in units of neurons, the level of activity in the reticular population also increases, spreading farther horizontally from the center. Not surprisingly, this greater inhibitory activity from the reticular network increases the likelihood of I_T deinactivation in the stimulated TC cells (Figure 6.2(b)), measured here as number of bursts per unit length of the bar.

How would cortical input influence the response? In the previous chapter, cortical inputs reduced the threshold for activation of bursts, increasing the number of bursts with the level of cortical input. Since the cortical feedback diverges into the reticular nucleus and lateral geniculate nucleus, the cortical feedback has the effect of increasing the excitability of multiple cells within the population, not just those at the same spatial location. This is demonstrated in Figure 6.3(a): The spread of the reticular activity with respect to bar length is much greater with the cortical feedback, as not only are the stimulated TC cells excited, the cortical fan-out influences the reticular network.

But the addition of the cortical inputs adds another dimension: the *shape* of the cortical feedback. Figure 6.3(b) plots the burst response per unit length of retinal bar to four different cortical configurations. The black curve shows the original data from Figure 6.2(b), absent cortical feedback. The green curve plots the response when the length of the cortical bar varies with the retinal input; that is, the number of cells

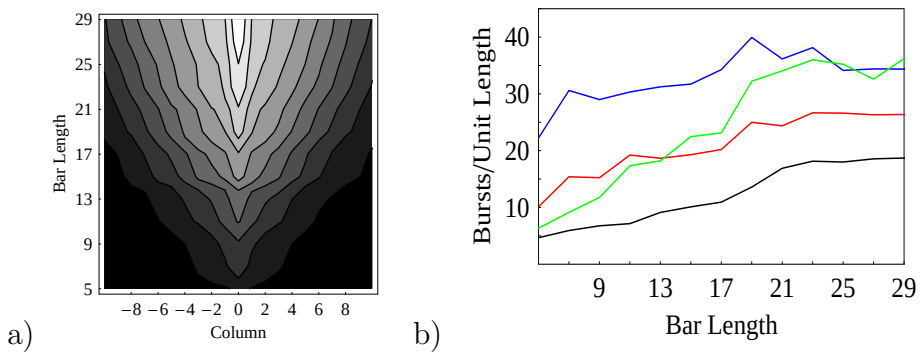

Figure 6.3: Cortical Influence on Reticular Population Activity

Same experiment as in Figure 6.2 with the addition of cortical 40Hz input Poisson spike train at the cortical synapses. a) The grayscale range (0-1) maps to the total number of spikes in a column (0-70). In this map, the length of the cortical bar varies with the retinal input. b) Average number of bursts as a function of input bar length. Each neuron in the bar received independent Poisson spike trains with a rate of 40Hz. The different colored lines represent different configurations for the cortical input. Black: no cortical input, retinal input only (Figure 6.2(b)). Red: Cortical bar length varies with retinal. Green: Cortical bar length fixed at 11 neurons. Blue: Cortical bar width fixed at 29 neurons

receiving cortical spikes matches the retinal input. In this situation, the number of bursts increased more rapidly with each increasing unit length, since there is now the additional influence of greater cortical feedback with each increase in bar size.

The other two curves in Figure 6.3(b) use a fixed cortical bar length. For the red curve, the cortical bar length is fixed at 13 neurons, approximately where the green and red curve meet, while the blue curve has a cortical bar spanning 29 cells. With each increasing bar length (from 0 (black) to 13 (red) to 29 (blue) cells), there was a general increase in the excitability of the system, but the response to retinal bar

lengths increased at approximately the same rate in all three situations.

Thus, greater amounts of cortical input, whether in the form of higher input rate of the previous chapter or greater input population activity here, increased the likelihood of bursts through an increase in the excitability of the reticular and relay neurons in the system. In the context of bursts as a measure of saliency, cortical feedback, acting as an attention mechanism, can increase the saliency of a weaker (smaller) stimulus.

6.2 Discussion and Conclusions

Studying I_T is difficult given its sensitivity to the resting membrane voltage of the cell. Anesthesia can increase the number of observed bursts in the thalamic response, through increased hyperpolarization of the membrane voltage[87, 86]. And as demonstrated in Chapter 4, shifts in the resting potential can alter the response properties of thalamic cells due to increased deinactivation of I_T. As a result, care must be taken in interpreting studies of I_T that use anesthetized animals[41, 83, 109, 113, 78].

Since it is not possible to record from the ion channel itself, the influence of I_T is often measured extracellularly through the presence of bursts within the spike train[83]. This classification of output spikes as bursts and non-bursts may be misleading, as the assumption often follows that the thalamus functions in two response modes[94, 83, 120]. However, when considering that the duration (Figure 3.2(b)) and level of hyperpolarization (Figure 3.3(b)) influences the size of the Ca^{++} spike[157], the burst response is but an extreme condition within a continuum of possible responses by the channel. So while I also used the same classification of bursts in my

previous chapter, my interpretation of the results consider I_T as capable of a variable response.

Figure 6.4 summarizes the role of the T channel, the reticular nucleus, and the cortical feedback on the response of the TC cell and the resulting influence within the cortex. Since TC and RE cell are depolarized in the awake state[52, 134], I_T is inactivated absent any input and requires inhibition for deinactivation to occur. Thus, the presence of I_T depends on the visual response properties of the inhibitory cells within the thalamus. I have chosen to study the role of reticular cells—as opposed to thalamic interneurons—given their interesting position between the thalamus and the cortex, merging ascending thalamocortical and descending corticothalamic information.

As discussed in Section 2.2, PGN cell possess large receptive fields relative to geniculate cells [35, 29, 54]. Since geniculate cells are the sole source of visual input[1], there is a large convergence from the geniculate layer. As such, perigeniculate cells increase their response with stimulus size[35]. In addition, PGN cells respond strongly to moving stimuli within their receptive fields, due to the continuous input from the relay neurons[35, 29]. Thus, the likelihood of bursting should increase in these two instances, as has been observed with increasing stimulus size[152] and suggested for moving stimuli[71, 72].

The burst response in my network also required a well-timed trigger to activate I_T after deinactivation, otherwise I_T inactivates and the influence is lost. These two components to the T channel response—the deinactivation and activation—suggests the role of the T channel as an enhancement of correlation between two (possibly) independent signals, with the level and temporal position of the enhancement de-

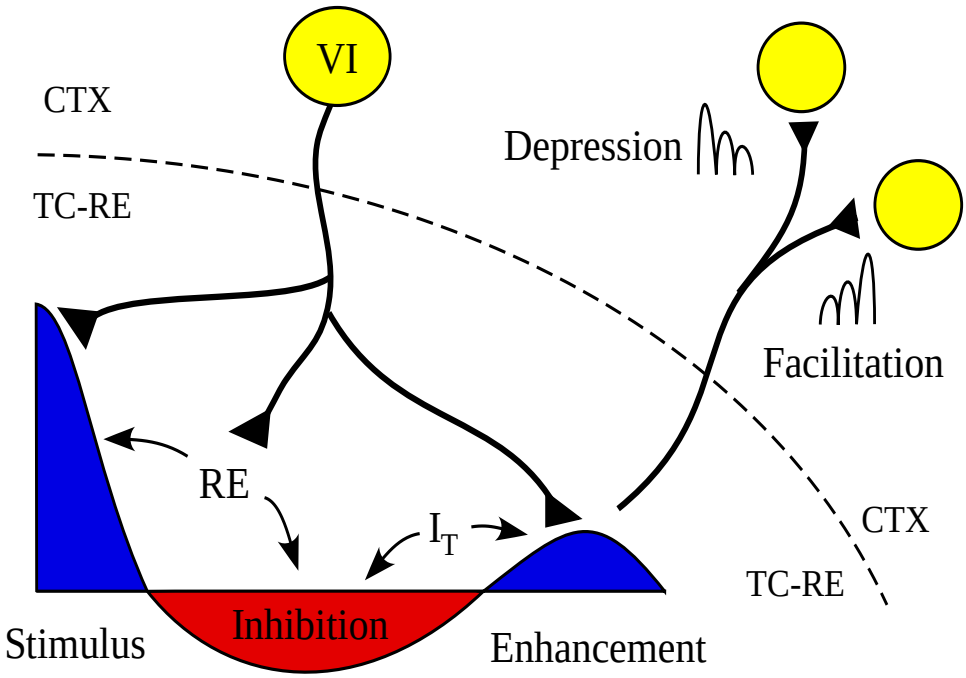

Figure 6.4: Thalamo-Reticulo-Cortical Interactions

This figure shows the influence of the reticular nucleus, the cortical feedback, and I_T on the response properties of the thalamic neuron. The thalamic response is presented as the first order kernel from Figure 5.3(b). See text for details.

pendent on the inhibition. Thus, as indicated in Figure 6.4, the role of the reticular nucleus is to translate the features within the stimulus to a level of inhibition in the relay cell. The T channel, then, translates the inhibition to a level of enhancement by I_T for another input signal.

I_T dynamics, as discussed in the previous chapter, influence the response at both depressing and facilitating synapses within the cortex[143]. Depressing synapses benefit from the deinactivation period (duration of the inhibition), which aids the synaptic recovery from its perpetually depressed state, strengthening the response to the initial spike within a burst[137]. Facilitating synapses benefit from the tighter spikes (smaller interspike intervals) because of I_T enhancement[144]. Thus, I_T dynamics link the gain at both synapses, even though they occur through different mechanisms. Even in the absence of depressing or facilitating synapses, bursts are also more reliable responses at unreliable synapses[79]. Regardless of the synaptic mechanism, high-frequency trains of spikes are better than single spikes at activating widespread recurrent activity in cortical layers[9].

I_T is also likely to help synchronize the response of TC cells to a stimulus. Reticular cells with overlapping receptive fields also overlap in their terminal axonal fields in the thalamus[106]. Thus, for a large stimulus, reticular inhibition that deinactivates I_T does so in multiple thalamic cells. The activation of I_T then ensures a greater degree of synchrony within these cells by reducing the effects of variability between them in the integration of synaptic inputs, generating a greater influence on cortical cells[129, 6, 143].

Cortical feedback influences the system in two ways: 1) it increases the response of TC and/or RE cells to the initial stimulus by increasing the total input current; 2)

it increases the response of the cells during the I_T enhancement phase. The cortical input acts as an attentive mechanism, increasing the response of the system such that smaller stimuli can achieve equal levels of inhibition/I_T-enhancement as larger stimuli without the cortical aid. These attention related influences have been observed in the LGN[103]. Many studies have suggested the importance of the reticular nucleus in attention (reviewed in [91]). Lesions of the reticular nucleus eliminated the attentional advantages of a visual cue preceding a target in reaction time tasks in rats[151]. In addition, specific sensory areas of the reticular nucleus, used by rats to attend to stimuli during active exploration, demonstrated higher levels of activity compared to other sensory areas not used[98].

One of the design flaws in my chip involves the strength of the cortical feedback onto thalamic and reticular cells. In my system, cortical synapses onto the reticular and thalamic cells were designed with equal weight. However, observations on synaptic numbers[81] and on the size of the cortical EPSCs between RE cells and TC cells[40] suggest the cortex has a greater influence on the reticular nucleus than the thalamic cells.

How would this affect my results? Obviously this would increase the influence of the cortex on the generation of bursts. In my experiments, the cortical feedback was set up as a modulatory influence; that is, the feedback was sufficiently weak to prevent spiking, or minimize spiking, in the TC cell, and (as a consequence) in the RE cell. Strengthening the cortical influence on reticular cell gives more control to the cortex in the deinactivation of I_T, possibly to the point of allowing the cortical inputs to "prime" I_T without the TC cell input. This is outside the scope, and capabilities, of my current system, since the synaptic weights are fixed within my chip. Some studies in the somatosensory system of rats suggest a role for the cortical

input in causing bursts during different behavioral states[32], while another theory on thalamic function suggest the inhibition from cortical feedback acts as a predictive element to sensory processing[131]. Although, computational studies on the role of corticothalamic input into the thalamo-reticular system suggest the influence of the cortical inputs to thalamic cells is predominantly excitatory, even with the stronger reticular synapses[21, 28].

How do my results apply to visual processing? During visual scene analysis, humans generate eye movements (saccades) approximately 3 times a second to shift the visual image such that various visual features are centered on the fovea[47, 48]. Visual processing occurs between saccades, where the visual image remains relatively stable. The sudden changes in the visual field by saccades cause changes in contrast levels within the visual field. Since reticular cells are responsive to contrast changes in their receptive field[35], they would likely become transiently active.

Figure 2.7 shows the post-saccadic[1] response of an ON center Y-cell to a large flashing square overlapping the receptive field[77]. The initial transient represents the initial viewing of the stimulus, presumably where initial acquisition and analysis of the new visual scene occurs, in line with observations that some visual processing occurs at higher levels in under 150ms [138]. The inhibitory period is the responding reticular inhibition, which then causes the secondary peak, through I_T, within the response.

As already discussed above, the reticular nucleus translates the stimulus size to inhibition, which then relates to the size of the I_T response. If all the cells responding

[1]The qualifier *post-saccadic* is technically accurate in the sense that the flashing square stimulus used to generate the responses in Figure 2.7 occurred shortly after a saccade. However, the stimulus onset was varied over 500ms, making it more likely that any effects of the saccade are averaged out. Thus, the response in Figure 2.7would most likely be similar in the absence of the saccade.

to the same stimulus receive the same level of inhibition, then the latency introduced by different object sizes (via inhibition) also serves as a way to solve the binding problem[37] through their synchrony[129].

The enhancement by I_T need not occur at the same spatial location as the original stimulus. Rather, through the axonal divergence between the thalamus and the reticular nucleus, a moving stimulus can 'prime' locations ahead in space, using I_T to synchronize responses of geniculate cells once the bar eventually crosses the receptive field[127, 71, 126].

The spatial extent of the inhibition preceding a moving stimulus would depend on the velocity of the stimulus. This then excludes the classical receptive field as a medium for this inhibition given its fixed spatial size. However, moving gratings outside the classical receptive field—in the *extra-classical* surround—are capable of inhibiting relay cells[150]. Interestingly, cells in magnocellular pathway, which are more sensitive to motion in the visual field, demonstrate greater extra-classical inhibition than parvocellular cells[150].

Given their larger receptive fields and their propensity to respond strongly to moving gratings, PGN cells are the likely source for this inhibition[29, 35]. It is unclear whether the driving source of this inhibition derives from relay neurons or from the cortex. Cortical feedback cells are direction selective and can influence the response of geniculate cells to moving gratings[101, 17, 126]. Ablating V1 reduces the effects of the extra-classical inhibition[150], but does not eliminate it. In line with the idea of attentional modulation, cortical feedback may control the level and/or extent of this inhibition in response to the moving stimulus.

Presumably, greater stimulus velocity requires more inhibition from reticular cells, since moving gratings generate greater activity in the perigenicualte nucleus than static gratings[35] (see also Figure 2.6(b)). What is interesting about this fact is that, to an observer, closer objects are both larger and move faster, two characteristics to which PGN cells naturally respond.

Low threshold calcium channels exist in numerous places within the brain: in the neocortex[38], in the inferior olive[82], within cerebellar purkinje cells[108], in hippocampal interneurons[33], and in many other areas[57]. The channel properties vary dramatically, both in their time constants and in their steady-state levels for activation and inactivation (reviewed in [57]). It is difficult to say whether the role of the T channel in those instances are similar to what my results suggest, since even minor differences in the resting potential of the cell with respect to steady-state levels can change the response dynamics. If, however, the channel is naturally inactivated, like those in the inferior olive[82], then the channel deinactivation becomes dependent on inhibition, linking the dynamics of the inhibitory input to any post-inhibitory input. The different temporal dynamics of the channels then define the different response of the channels: a shorter deinactivation period, for example, means less inhibition is needed. Understanding the role of the T channel, in these cases, should begin with a greater understanding of the inhibitory influences.

To conclude, I pose the question: Was there an advantage to using silicon as a medium for these models? Since I have not implemented a comparable computational model (in terms of network structure and interactions), I cannot do a direct comparison with my network. However, since computational models numerically solve a series of differential equations, one method of comparison would be to calculate the number of differential equations needed for my chip and estimate the simulation time based

on results from a computational model.

Each neuron (without synapses) on my chip requires three differential equations: 2 for I_T (activation and inactivation) and one for the membrane. Within a single node in the hexagonal array (Figure 6.1), there are approximately 9 differential equations for all of the synaptic interactions (6 for all retinal input interactions, and 1 each for TC excitation, RE inhibition and cortical input). That translates to 24 differential equations per node: 15 for all 5 cells within a node, plus 9 for all the synaptic dynamics. Since there are 1440 nodes within the neuron array, that translates to approximately 34,560 differential equations for the whole chip.

A simulation of a single cell model in NEURON[154]—with 29 compartments each consisting of 18-20 ion channels for a total of 5,568 differential equations—on a dual 2.5GHz G5 (with 2GB RAM) ran at 300-times slower than real-time. Assuming linear extrapolation, my chip would run about 1860 times slower than real-time as a computer model. In other words, there is a tremendous advantage to using the silicon in performing the experiments.

Even in the two-cell system of the previous chapter, the chip outperforms the computational model. The two-cell system consists of 8 differential equations: 3 for the TC cell with I_T, 1 for the RE cell, 4 for the different synaptic interactions. This translates to a simulation running about 2.3 times *faster* than real-time. However, recall that my chip was running in *hypertime*, approximately 10 times faster than real-time. This is just over 4 times faster than the equivalent computational model, making the silicon medium advantageous in experiments where large quantities of data are collected at low input rates, such as in many of the kernel computations within this work.

Appendix A

Common Transistor Circuits

This appendix describes two common transistor circuits used within my neuromorphic model.

A.1 Current Mirror

In analog circuit design, it is often necessary to invert a current before merging two separate circuits. The most common circuit for this task is the *current mirror* (Figure A.1(a)).

Circuit operation is very simple. Connecting the gate to the drain terminal of the input transistor moves the gate sufficiently to match the channel current with the input current. Since the input and output transistors share gate terminals, the output current then has the same magnitude—but now opposite sign—as the input.

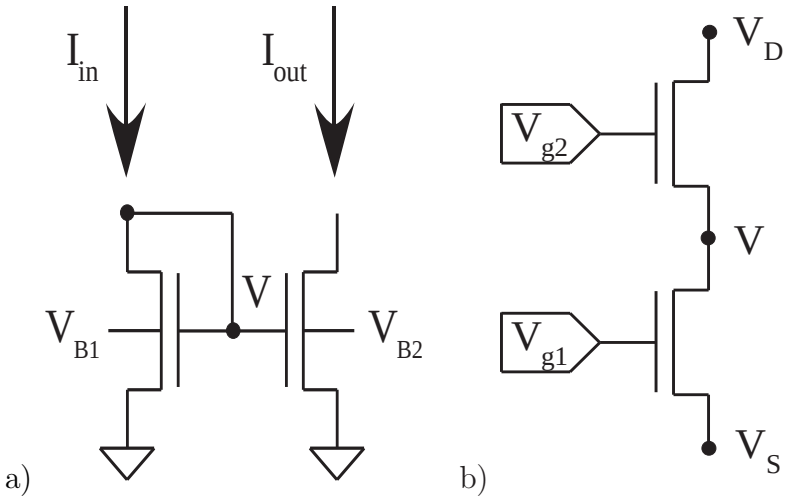

Figure A.1: Basic Transistor Circuits

a) Current Mirror. As its name implies, this circuit *mirrors* the input current. That is, a current source (sink) into the mirror is outputted as a current sink (source) with unity gain. The bulk voltages V_{B1} and V_{B2} can be used to adjust the gain in the mirror. (b) Series Transistors. Two transistors in series function the same as two conductors in series: the total conductance is equivalent to product of the conductances normalized by their sum. Similarly, the output current is the product of the currents in the individual transistors normalized by their sum. See text for details.

Gain in the mirror circuit is commonly implemented either through differences in the dimensions of the input and output transistors, or through differences in their source voltages. However, it is also possible to use the back gate for this purpose. From Equation 3.18,

$$
\begin{aligned}
I_{OUT} &= I_{ds0}\, e^{\kappa V} e^{(1-\kappa)V_{B2}} \\
&= \frac{I_{IN}}{e^{(1-\kappa)V_{B1}}} e^{(1-\kappa)V_{B2}} \\
&= I_{IN}\, e^{(1-\kappa)(V_{B2}-V_{B1})}
\end{aligned} \tag{A.1}
$$

Intuitively, lowering V_{B1} necessitates a higher gate voltage to match the channel current with the input, increasing the output current, and thus the gain. If I lower V_{B2} instead, then I decrease the channel current in the output transistor for a given gate voltage, thus lowering the gain.

A.2 Series Transistors

Another common transistor combination is the series placement of two (or more) transistors (Figure A.1(b)). Intuitively, the output of such a circuit will always be limited by the transistor with the smaller individual current (i.e., lower gate voltage).

The current through the transistors is defined as

$$
I = I_1 \left(e^{-V_S} - e^{-V}\right) = I_2 \left(e^{-V} - e^{-V_D}\right) \tag{A.2}
$$

where $I_1 = I_{ds0}\, e^{\kappa\, V_{g1}}$ and $I_2 = I_{ds0}\, e^{\kappa\, V_{g2}}$ and V is the voltage at the middle terminal (see Figure A.1(b)). Solving for e^{-V} and substituting back into Equation A.2,

$$
\begin{aligned}
e^{-V} &= \frac{I_1}{I_1 + I_2} e^{-V_S} + \frac{I_2}{I_1 + I_2} e^{-V_D} \\
I &= I_1 \left(e^{-V_S} - e^{-V} \right) \\
&= I_1 \left(e^{-V_S} - \frac{I_1}{I_1 + I_2} e^{-V_S} - \frac{I_2}{I_1 + I_2} e^{-V_D} \right) \\
&= I_1 \left(\frac{I_2}{I_1 + I_2} e^{-V_S} - \frac{I_2}{I_1 + I_2} e^{-V_D} \right) \\
&= \frac{I_1 \, I_2}{I_1 + I_2} \left(e^{-V_S} - e^{-V_D} \right) \qquad \text{(A.3)}
\end{aligned}
$$

The output current is then the product of the individual currents normalized by their sum [20]. Since the output current is proportional to the product of the inputs, it is often used as a *current correlator*.

A.3 Diffusor Circuit

Figure A.2 shows the diffusor circuit, which I use to extend synaptic input spatially to implement synaptic fan-out within a network. The output current at each node i is defined by

$$
I_i = I_{ds0} \, e^{\kappa \, V_w} \left(e^{-V_i} \right) \qquad \text{(A.4)}
$$

The current within the horizontal transistors P2 is defined by

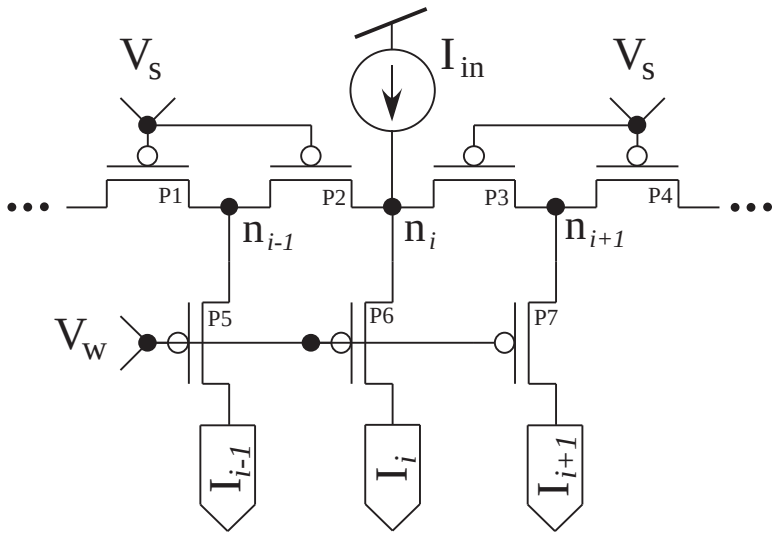

Figure A.2: Diffusor Circuit

Diffusor circuit for implementing network connections within the chip. The input current is the output of the synapse described in Section 4.1.2. The biases V_w and V_s define the space constant of the diffusor circuit. Each diffusor output current I_i enters the membrane of a spatially distinct neuron.

$$I_{P2} = I_{ds0}\, e^{\kappa\, V_s} \left(e^{-V_i} - e^{-V_{i-1}} \right) \tag{A.5}$$

Substituting Equation A.4 into Equation A.5:

$$
\begin{aligned}
\mathrm{I_{P2}} &= \mathrm{e}^{\kappa\ \mathrm{V_s}} \left(\mathrm{e}^{-\kappa\ \mathrm{V_w}}\ \mathrm{I}_i - \mathrm{e}^{-\kappa\ \mathrm{V_w}}\ \mathrm{I}_{i-1} \right) \\
&= \mathrm{e}^{\kappa\ (\mathrm{V_s} - \mathrm{V_w})} \left(\mathrm{I}_i - \mathrm{I}_{i-1} \right) \\
&= \alpha \left(\mathrm{I}_i - \mathrm{I}_{i-1} \right)
\end{aligned}
$$

where $\alpha = \exp\left[\kappa\ (\mathrm{V_s} - \mathrm{V_w}) \right]$. Ignoring (for the moment) the fixed input current $\mathrm{I_{in}}$ (Figure A.2), Kirchoff's current law for node n_i requires

$$
\begin{aligned}
0 &= \alpha\ (\mathrm{I}_i - \mathrm{I}_{i-1}) + \alpha\ (\mathrm{I}_i - \mathrm{I}_{i+1}) + \mathrm{I}_i \\
&= \mathrm{I}_i - \alpha\ (\mathrm{I}_{i-1} - 2\ \mathrm{I}_i + \mathrm{I}_{i+1})
\end{aligned}
$$

Substituting $\mathrm{I}_i = \lambda^i$:

$$
\begin{aligned}
\lambda^i - \alpha\ \left(\lambda^{i-1} - 2\ \lambda^i + \lambda^{i+1} \right) &= 0 \\
\alpha\ \lambda^{i-1} \left(\lambda^2 - \left(2 + \frac{1}{\alpha} \right) \lambda + 1 \right) &= 0
\end{aligned}
$$

Ignoring the simple solution and solving the quadratic for λ:

$$
\lambda_{+,-} = \left(1 + \frac{1}{2\,\alpha} \right) \pm \sqrt{\frac{1}{\alpha} + \frac{1}{4\,\alpha^2}}
$$

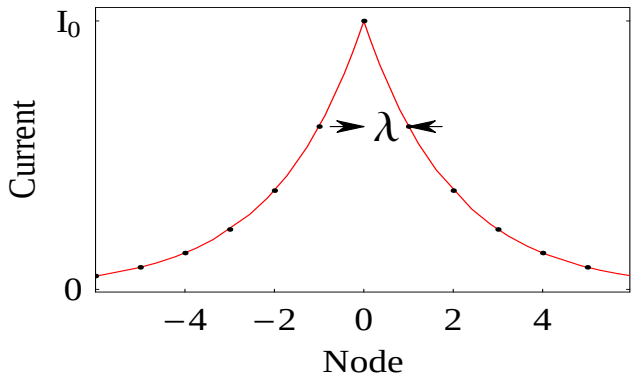

Figure A.3: Diffusor Output

Sample output current plotted versus the distance from the center. The output decays exponentially, with a space constant λ. Note that $I_{in} = \sum_i I_i$.

What this suggests, then, is that the current changes exponentially from node to node. Since $\lambda_- = 1/\lambda_+ < 1$, the output current is either rising or falling exponentially with increasing i. The transistor biases V_w and V_s define α—the ratio of the input current that flows horizontally (spatially) versus vertically (into the cell)—which defines the space constant for the exponential.

Introducing an input current into node n_i:

$$I_{in} = I_i - \alpha \left(I_{i-1} - 2\, I_i + I_{i+1} \right)$$

Since the diffusor is a passive circuit, $I_{in} = \sum_i I_i$. In addition, the location of the input defines the center of the decaying exponential (Figure A.3):

$$\mathrm{I}_j = \mathrm{I}_0 \, \lambda^{|j-i|}$$

where $\lambda = \lambda_-$ and $\mathrm{I}_0 = \mathrm{I}_i$. Solving for I_0:

$$\begin{aligned} \mathrm{I}_{\mathrm{in}} &= \mathrm{I}_i - \alpha \, (\, \mathrm{I}_{i-1} - 2 \, \mathrm{I}_i + \mathrm{I}_{i+1} \,) \\ &= \mathrm{I}_i - \alpha \, (\, \lambda \, \mathrm{I}_i - 2 \, \mathrm{I}_i + \lambda \, \mathrm{I}_i \,) \\ &= \big(\, 1 + 2 \, \alpha \, (1 - \lambda) \, \big) \, \mathrm{I}_i \\ \therefore \mathrm{I}_0 &= \frac{1}{1 + 2 \, \alpha \, (1 - \lambda)} \, \mathrm{I}_{\mathrm{in}} \end{aligned}$$

where $\lambda = \lambda_-$. Substituting λ_-:

$$\mathrm{I}_0 = \frac{1}{\sqrt{4 \, \alpha + 1}} \, \mathrm{I}_{\mathrm{in}}$$

Thus,

$$\mathrm{I}_j = \frac{1}{\sqrt{4 \, \alpha + 1}} \, \mathrm{I}_{\mathrm{in}} \, \lambda^{|j-i|}$$

For the hexagonal grid used within my networks (Figure 6.1), the diffusor circuit

forms a two-dimensional decaying exponential, centered at the synaptic input.

Bibliography

[1] G. Ahlsen and S. Lindstrom. Excitation of perigeniculate neurones via axon collaterals of principal cells. *Brain Res*, 236(2):477–81, 1982.

[2] G. Ahlsen and S. Lindstrom. Mutual inhibition between perigeniculate neurones. *Brain Res*, 236(2):482–6, 1982.

[3] G. Ahlsen and S. Lindstrom. Corticofugal projection to perigeniculate neurones in the cat. *Acta Physiol Scand*, 118(2):181–4, 1983.

[4] G. Ahlsen, S. Lindstrom, and F. S. Lo. Excitation of perigeniculate neurones from x and y principal cells in the lateral geniculate nucleus of the cat. *Acta Physiol Scand*, 118(4):445–8, 1983.

[5] G. Ahlsen, S. Lindstrom, and F. S. Lo. Interaction between inhibitory pathways to principal cells in the lateral geniculate nucleus of the cat. *Exp Brain Res*, 58(1):134–43, 1985.

[6] J. M. Alonso, W. M. Usrey, and R. C. Reid. Precisely correlated firing in cells of the lateral geniculate nucleus. *Nature*, 383(6603):815–9, 1996.

[7] S. A. Baccus and M. Meister. Fast and slow contrast adaptation in retinal circuitry. *Neuron*, 36(5):909–19, 2002.

[8] T. Bal and D. A. McCormick. Mechanisms of oscillatory activity in guinea-pig nucleus reticularis thalami in vitro: a mammalian pacemaker. *J Physiol*, 468:669–91, 1993.

[9] M. Beierlein, C. P. Fall, J. Rinzel, and R. Yuste. Thalamocortical bursts trigger recurrent activity in neocortical networks: layer 4 as a frequency-dependent gate. *J Neurosci*, 22(22):9885–94, 2002.

[10] K. A. Boahen. A retinomorphic vision system. *Ieee Micro*, 16(5):30–39, 1996.

[11] K. A. Boahen. Point-to-point connectivity between neuromorphic chips using address events. *IEEE Transactions on Circuits and Systems II: Analog and Digital Signal Processing*, 47(5):416–434, 2000.

[12] A. R. Casti, A. Omurtag, A. Sornborger, E. Kaplan, B. Knight, J. Victor, and L. Sirovich. A population study of integrate-and-fire-or-burst neurons. *Neural Comput*, 14(5):957–86, 2002.

[13] D. Chander and E. J. Chichilnisky. Adaptation to temporal contrast in primate and salamander retina. *J Neurosci*, 21(24):9904–16, 2001.

[14] B. G. Cleland, M. W. Dubin, and W. R. Levick. Sustained and transient neurones in the cat's retina and lateral geniculate nucleus. *J Physiol*, 217(2):473–96, 1971.

[15] F. Crick. Function of the thalamic reticular complex: the searchlight hypothesis. *Proc Natl Acad Sci U S A*, 81(14):4586–90, 1984.

[16] V. Crunelli and N. Leresche. A role for gabab receptors in excitation and inhibition of thalamocortical cells. *Trends Neurosci*, 14(1):16–21, 1991.

[17] J. Cudeiro and A. M. Sillito. Spatial frequency tuning of orientation-discontinuity-sensitive corticofugal feedback to the cat lateral geniculate nucleus. *J Physiol (Lond)*, 490(Pt 2):481–92, 1996.

[18] E. Culurciello, R. Etienne-Cummings, and K.A. Boahen. A biomorphic digital image sensor. *IEEE Journal of Solid-State Circuits*, 38(2):281–94, 2003.

[19] Peter Dayan and L. F. Abbott. *Theoretical neuroscience : computational and mathematical modeling of neural systems*. Computational neuroscience. MIT Press, Cambridge, Mass. ; London, 2001.

[20] T. Delbruck. 'bump' circuits for computing similarity and dissimilarity of analog voltages. In *Neural Networks, 1991., IJCNN-91-Seattle International Joint Conference on*, volume i, pages 475–479 vol.1, 1991.

[21] A. Destexhe. Modelling corticothalamic feedback and the gating of the thalamus by the cerebral cortex. *J Physiol Paris*, 94(5-6):391–410, 2000.

[22] A. Destexhe, T. Bal, D. A. McCormick, and T. J. Sejnowski. Ionic mechanisms underlying synchronized oscillations and propagating waves in a model of ferret thalamic slices. *J Neurophysiol*, 76(3):2049–70, 1996.

[23] A. Destexhe and J. R. Huguenard. Nonlinear thermodynamic models of voltage-dependent currents. *J Comput Neurosci*, 9(3):259–70., 2000.

[24] A. Destexhe and J. R. Huguenard. Which formalism to use for voltage-dependent conductances? In Robert C. Cannon and Erik de Schutter, editors, *Computational neuroscience : realistic modeling for experimentalists*, pages 129–157. CRC, Boca Raton, 2001.

[25] A. Destexhe, Z. F. Mainen, and T. Sejnowski. Kinetic models in synaptic transmission. In C. Koch and I. Segev, editors, *Methods in neuronal modeling : from ions to networks*, pages xiii, 671. MIT Press, Cambridge, Mass., 2nd edition, 1998.

[26] A. Destexhe, Z. F. Mainen, and T. J. Sejnowski. Synthesis of models for excitable membranes, synaptic transmission and neuromodulation using a common kinetic formalism. *J Comput Neurosci*, 1(3):195–230, 1994.

[27] A. Destexhe, M. Neubig, D. Ulrich, and J. Huguenard. Dendritic low-threshold calcium currents in thalamic relay cells. *J Neurosci*, 18(10):3574–88., 1998.

[28] A. Destexhe and T. J. Sejnowski. The initiation of bursts in thalamic neurons and the cortical control of thalamic sensitivity. *Philos Trans R Soc Lond B Biol Sci*, 357(1428):1649–57, 2002.

[29] M. W. Dubin and B. G. Cleland. Organization of visual inputs to interneurons of lateral geniculate nucleus of the cat. *J Neurophysiol*, 40(2):410–27, 1977.

[30] C. Enroth-Cugell and J.G. Robson. The contrast sensitivity of retinal ganglion cells of the cat. *J Physiol (Lond)*, 187:517–552, 1966.

[31] A. Erisir, S. C. Van Horn, and S. M. Sherman. Relative numbers of cortical and brainstem inputs to the lateral geniculate nucleus. *Proc Natl Acad Sci U S A*, 94(4):1517–20, 1997.

[32] E. E. Fanselow, K. Sameshima, L. A. Baccala, and M. A. Nicolelis. Thalamic bursting in rats during different awake behavioral states. *Proc Natl Acad Sci U S A*, 98(26):15330–5, 2001.

[33] D. D. Fraser and B. A. MacVicar. Low-threshold transient calcium current in rat hippocampal lacunosum-moleculare interneurons: kinetics and modulation by neurotransmitters. *J Neurosci*, 11(9):2812–20, 1991.

[34] M. J. Friedlander, C. S. Lin, L. R. Stanford, and S. M. Sherman. Morphology of functionally identified neurons in lateral geniculate nucleus of the cat. *J Neurophysiol*, 46(1):80–129, 1981.

[35] K. Funke and U. T. Eysel. Inverse correlation of firing patterns of single topographically matched perigeniculate neurons and cat dorsal lateral geniculate relay cells. *Vis Neurosci*, 15(4):711–29, 1998.

[36] F. Gabbiani and C. Koch. Principles of spike train analysis. In C. Koch and I. Segev, editors, *Methods in neuronal modeling : from ions to networks*. MIT Press, Cambridge, Mass., 2nd edition, 1998.

[37] T. J. Gawne, T. W. Kjaer, and B. J. Richmond. Latency: another potential code for feature binding in striate cortex. *J Neurophysiol*, 76(2):1356–60, 1996.

[38] K. Giffin, J. S. Solomon, A. Burkhalter, and J. M. Nerbonne. Differential expression of voltage-gated calcium channels in identified visual cortical neurons. *Neuron*, 6(3):321–32, 1991.

[39] D. W. Godwin, J. W. Vaughan, and S. M. Sherman. Metabotropic glutamate receptors switch visual response mode of lateral geniculate nucleus cells from burst to tonic. *J Neurophysiol*, 76(3):1800–16, 1996.

[40] P. Golshani, X. B. Liu, and E. G. Jones. Differences in quantal amplitude reflect glur4- subunit number at corticothalamic synapses on two populations of thalamic neurons. *Proc Natl Acad Sci U S A*, 98(7):4172–7, 2001.

[41] W. Guido, S. M. Lu, and S. M. Sherman. Relative contributions of burst and tonic responses to the receptive field properties of lateral geniculate neurons in the cat. *J Neurophysiol*, 68(6):2199–211, 1992.

[42] W. Guido and T. Weyand. Burst responses in thalamic relay cells of the awake behaving cat. *J Neurophysiol*, 74(4):1782–6, 1995.

[43] R. H. Hahnloser, R. Sarpeshkar, M. A. Mahowald, R. J. Douglas, and H. S. Seung. Digital selection and analogue amplification coexist in a cortex-inspired silicon circuit. *Nature*, 405(6789):947–51, 2000.

[44] J. A. Hartings, S. Temereanca, and D. J. Simons. State-dependent processing of sensory stimuli by thalamic reticular neurons. *J Neurosci*, 23(12):5264–71, 2003.

[45] E. Hartveit and P. Heggelund. Neurotransmitter receptors mediating excitatory input to cells in the cat lateral geniculate nucleus. ii. nonlagged cells. *J Neurophysiol*, 63(6):1361–72, 1990.

[46] P. Heggelund and E. Hartveit. Neurotransmitter receptors mediating excitatory input to cells in the cat lateral geniculate nucleus. i. lagged cells. *J Neurophysiol*, 63(6):1347–60, 1990.

[47] J. M. Henderson. Human gaze control during real-world scene perception. *Trends Cogn Sci*, 7(11):498–504, 2003.

[48] J. M. Henderson and A. Hollingworth. High-level scene perception. *Annu Rev Psychol*, 50:243–71, 1999.

[49] S. Hestrin. Different glutamate receptor channels mediate fast excitatory synaptic currents in inhibitory and excitatory cortical neurons. *Neuron*, 11(6):1083–91, 1993.

[50] T. L. Hill and Y. Chen. On the theory of ion transport across the nerve membrane. vi. free energy and activation free energies of conformational change. *Proc Natl Acad Sci U S A*, 69(7):1723–6, 1972.

[51] Bertil Hille. *Ionic channels of excitable membranes*. Sinauer Associates, Sunderland, Mass., 2nd edition, 1992.

[52] J. C. Hirsch, A. Fourment, and M. E. Marc. Sleep-related variations of membrane potential in the lateral geniculate body relay neurons of the cat. *Brain Res*, 259(2):308–12, 1983.

[53] A. L. Hodgkin and A. F. Huxley. A quantitative description of membrane current and its application to conduction and excitation in nerve. *J Physiol*, 117(4):500–44, 1952.

[54] K. P. Hoffmann, J. Stone, and S. M. Sherman. Relay of receptive-field properties in dorsal lateral geniculate nucleus of the cat. *J Neurophysiol*, 35(4):518–31, 1972.

[55] T. Horiuchi and K. Hynna. Spike-based vlsi modeling of the ild system in the echolocating bat. *Neural Networks*, 14(6-7):755–62., 2001.

[56] D. H. Hubel and T. N. Wiesel. Integrative action in the cat's lateral geniculate body. *J Physiol*, 155:385–98, 1961.

[57] J. R. Huguenard. Low-threshold calcium currents in central nervous system neurons. *Annu Rev Physiol*, 58:329–48, 1996.

[58] J. R. Huguenard and D. A. McCormick. Simulation of the currents involved in rhythmic oscillations in thalamic relay neurons. *J Neurophysiol*, 68(4):1373–83, 1992.

[59] J. R. Huguenard and D. A. Prince. A novel t-type current underlies prolonged ca(2+)-dependent burst firing in gabaergic neurons of rat thalamic reticular nucleus. *J Neurosci*, 12(10):3804–17, 1992.

[60] J. R. Huguenard and D. A. Prince. Intrathalamic rhythmicity studied in vitro: nominal t-current modulation causes robust antioscillatory effects. *J Neurosci*, 14(9):5485–502, 1994.

[61] K. Hynna and K. Boahen. Space-rate coding in an adaptive silicon neuron. *Neural Networks*, 14(6-7):645–56., 2001.

[62] G. Indiveri. Modeling selective attention using a neuromorphic analog vlsi device. *Neural Comput*, 12(12):2857–80, 2000.

[63] Giacomo Indiveri. A low-power adaptive integrate-and-fire neuron circuit. In *Proceedings of the 2003 IEEE International Symposium on Circuits and Systems, May 25-28 2003*, volume 4 of *Proceedings - IEEE International Symposium on Circuits and Systems*, pages 820–823, Bangkok, Thailand, 2003. Institute of Electrical and Electronics Engineers Inc.

[64] H. Jahnsen and R. Llinas. Electrophysiological properties of guinea-pig thalamic neurones: an in vitro study. *J Physiol*, 349:205–26, 1984.

[65] E. G. Jones. Some aspects of the organization of the thalamic reticular complex. *J Comp Neurol*, 162(3):285–308, 1975.

[66] Edward G. Jones, D. A. McCormick, and M. Steriade, editors. *Thalamus*, volume 1. Elsevier, New York, 1997.

[67] K. J. Kim and F. Rieke. Temporal contrast adaptation in the input and output signals of salamander retinal ganglion cells. *J Neurosci*, 21(1):287–99, 2001.

[68] K. J. Kim and F. Rieke. Slow na+ inactivation and variance adaptation in salamander retinal ganglion cells. *J Neurosci*, 23(4):1506–16, 2003.

[69] U. Kim and D. A. McCormick. The functional influence of burst and tonic firing mode on synaptic interactions in the thalamus. *J Neurosci*, 18(22):9500–16, 1998.

[70] U. Kim, M. V. Sanchez-Vives, and D. A. McCormick. Functional dynamics of gabaergic inhibition in the thalamus. *Science*, 278(5335):130–4, 1997.

[71] K. L. Kirkland and G. L. Gerstein. A model of cortically induced synchronization in the lateral geniculate nucleus of the cat: a role for low-threshold calcium channels. *Vision Res*, 38(13):2007–22, 1998.

[72] K. L. Kirkland, A. M. Sillito, H. E. Jones, D. C. West, and G. L. Gerstein. Oscillations and long-lasting correlations in a model of the lateral geniculate nucleus and visual cortex. *J Neurophysiol*, 84(4):1863–8, 2000.

[73] H.I. Krausz. Identification of nonlinear systems using random impulse train inputs. *Biological Cybernetics*, 19(4):217–30, 1975.

[74] S. W. Kuffler. Discharge patterns and functional organization of mammalian retina. *J Neurophysiol*, 16(1):37–68, 1953.

[75] M. F. Land and S. Furneaux. The knowledge base of the oculomotor system. *Philos Trans R Soc Lond B Biol Sci*, 352(1358):1231–9, 1997.

[76] N. Lavie and Y. Tsal. Perceptual load as a major determinant of the locus of selection in visual attention. *Percept Psychophys*, 56(2):183–97, 1994.

[77] D. Lee and J. G. Malpeli. Effects of saccades on the activity of neurons in the cat lateral geniculate nucleus. *J Neurophysiol*, 79(2):922–36, 1998.

[78] N. A. Lesica and G. B. Stanley. Encoding of natural scene movies by tonic and burst spikes in the lateral geniculate nucleus. *J Neurosci*, 24(47):10731–40, 2004.

[79] J. E. Lisman. Bursts as a unit of neural information: making unreliable synapses reliable. *Trends Neurosci*, 20(1):38–43, 1997.

[80] S. C. Liu, J. Kramer, G. Indiveri, T. Delbruck, T. Burg, and R. Douglas. Orientation-selective avlsi spiking neurons. *Neural Networks*, 14(6-7):629–643, 2001.

[81] X. B. Liu and E. G. Jones. Predominance of corticothalamic synaptic inputs to thalamic reticular nucleus neurons in the rat. *J Comp Neurol*, 414(1):67–79, 1999.

[82] R. Llinas and Y. Yarom. Properties and distribution of ionic conductances generating electroresponsiveness of mammalian inferior olivary neurones in vitro. *J Physiol*, 315:569–84, 1981.

[83] S. M. Lu, W. Guido, and S. M. Sherman. Effects of membrane voltage on receptive field properties of lateral geniculate neurons in the cat: contributions of the low-threshold ca2+ conductance. *J Neurophysiol*, 68(6):2185–98, 1992.

[84] S. M. Lu, W. Guido, and S. M. Sherman. The brain-stem parabrachial region controls mode of response to visual stimulation of neurons in the cat's lateral geniculate nucleus. *Vis Neurosci*, 10(4):631–42, 1993.

[85] M. Mahowald and R. Douglas. A silicon neuron. *Nature*, 354(6354):515–8, 1991.

[86] A. Massaux, G. Dutrieux, N. Cotillon-Williams, Y. Manunta, and J. M. Edeline. Auditory thalamus bursts in anesthetized and non-anesthetized states: contribution to functional properties. *J Neurophysiol*, 91(5):2117–34, 2004.

[87] A. Massaux and J. M. Edeline. Bursts in the medial geniculate body: a comparison between anesthetized and unanesthetized states in guinea pig. *Exp Brain Res*, 153(4):573–8, 2003.

[88] D. N. Mastronarde. Two classes of single-input x-cells in cat lateral geniculate nucleus. i. receptive-field properties and classification of cells. *J Neurophysiol*, 57(2):357–80, 1987.

[89] D. N. Mastronarde. Two classes of single-input x-cells in cat lateral geniculate nucleus. ii. retinal inputs and the generation of receptive-field properties. *J Neurophysiol*, 57(2):381–413, 1987.

[90] D. N. Mastronarde. Nonlagged relay cells and interneurons in the cat lateral geniculate nucleus: receptive-field properties and retinal inputs. *Vis Neurosci*, 8(5):407–41, 1992.

[91] K. McAlonan and V. J. Brown. The thalamic reticular nucleus: more than a sensory nucleus? *Neuroscientist*, 8(4):302–5, 2002.

[92] D. A. McCormick. Cholinergic and noradrenergic modulation of thalamocortical processing. *Trends Neurosci*, 12(6):215–21, 1989.

[93] D. A. McCormick and T. Bal. Sleep and arousal: thalamocortical mechanisms. *Annu Rev Neurosci*, 20:185–215, 1997.

[94] D. A. McCormick and H. R. Feeser. Functional implications of burst firing and single spike activity in lateral geniculate relay neurons. *Neuroscience*, 39(1):103–13, 1990.

[95] D. A. McCormick and M. von Krosigk. Corticothalamic activation modulates thalamic firing through glutamate "metabotropic" receptors. *Proc Natl Acad Sci U S A*, 89(7):2774–8, 1992.

[96] Carver Mead. *Analog VLSI and neural systems*. Addison-Wesley VLSI system series. Addison-Wesley, Reading, Mass., 1989.

[97] University of Florida College of Medicine. Review of neuroanatomy.

[98] V. M. Montero. c-fos induction in sensory pathways of rats exploring a novel complex environment: shifts of active thalamic reticular sectors by predominant sensory cues. *Neuroscience*, 76(4):1069–81, 1997.

[99] V. M. Montero, R. W. Guillery, and C. N. Woolsey. Retinotopic organization within the thalamic reticular nucleus demonstrated by a double label autoradiographic technique. *Brain Res*, 138(3):407–21, 1977.

[100] P. Mukherjee and E. Kaplan. Dynamics of neurons in the cat lateral geniculate nucleus: in vivo electrophysiology and computational modeling. *J Neurophysiol*, 74(3):1222–43, 1995.

[101] P. C. Murphy and A. M. Sillito. Corticofugal feedback influences the generation of length tuning in the visual pathway. *Nature*, 329(6141):727–9, 1987.

[102] P. C. Murphy and A. M. Sillito. Functional morphology of the feedback pathway from area 17 of the cat visual cortex to the lateral geniculate nucleus. *J Neurosci*, 16(3):1180–92, 1996.

[103] D. H. O'Connor, M. M. Fukui, M. A. Pinsk, and S. Kastner. Attention modulates responses in the human lateral geniculate nucleus. *Nat Neurosci*, 5(11):1203–9, 2002.

[104] T. S. Otis and I. Mody. Modulation of decay kinetics and frequency of gabaa receptor-mediated spontaneous inhibitory postsynaptic currents in hippocampal neurons. *Neuroscience*, 49(1):13–32, 1992.

[105] A. Pavasovic, A. G. Andreou, and C. R. Westgate. Characterization of subthreshold mos mismatch in transistors for vlsi systems. *J. VLSI Signal Process. Syst.*, 8(1):75–85, 1994.

[106] D. Pinault and M. Deschenes. Projection and innervation patterns of individual thalamic reticular axons in the thalamus of the adult rat: a three-dimensional, graphic, and morphometric analysis. *J Comp Neurol*, 391(2):180–203, 1998.

[107] E. J. Ramcharan, J. W. Gnadt, and S. M. Sherman. Burst and tonic firing in thalamic cells of unanesthetized, behaving monkeys. *Vis Neurosci*, 17(1):55–62., 2000.

[108] L. J. Regan. Voltage-dependent calcium currents in purkinje cells from rat cerebellar vermis. *J Neurosci*, 11(7):2259–69, 1991.

[109] P. Reinagel, D. Godwin, S. M. Sherman, and C. Koch. Encoding of visual information by lgn bursts. *J Neurophysiol*, 81(5):2558–69, 1999.

[110] Wolfram Research. Mathworld.

[111] F. Rieke. Temporal contrast adaptation in salamander bipolar cells. *J Neurosci*, 21(23):9445–54, 2001.

[112] Fred Rieke. *Spikes : exploring the neural code*. Computational neuroscience. MIT Press, Cambridge, Mass. ; London, 1997.

[113] C. Rivadulla, L. Martinez, K. L. Grieve, and J. Cudeiro. Receptive field structure of burst and tonic firing in feline lateral geniculate nucleus. *J Physiol*, 553(Pt 2):601–10, 2003.

[114] R. W. Rodieck and J. Stone. Analysis of receptive fields of cat retinal ganglion cells. *J Neurophysiol*, 28(5):832–49, 1965.

[115] H. M. Sakai. White-noise analysis in neurophysiology. *Physiol Rev*, 72(2):491–505, 1992.

[116] M. V. Sanchez-Vives and D. A. McCormick. Functional properties of perigeniculate inhibition of dorsal lateral geniculate nucleus thalamocortical neurons in vitro. *J Neurosci*, 17(22):8880–93, 1997.

[117] K. J. Sanderson. The projection of the visual field to the lateral geniculate and medial interlaminar nuclei in the cat. *J Comp Neurol*, 143(1):101–8, 1971.

[118] A. B. Saul and A. L. Humphrey. Spatial and temporal response properties of lagged and nonlagged cells in cat lateral geniculate nucleus. *J Neurophysiol*, 64(1):206–24, 1990.

[119] A. B. Saul and A. L. Humphrey. Evidence of input from lagged cells in the lateral geniculate nucleus to simple cells in cortical area 17 of the cat. *J Neurophysiol*, 68(4):1190–208, 1992.

[120] S. M. Sherman. Tonic and burst firing: dual modes of thalamocortical relay. *Trends Neurosci*, 24(2):122–6, 2001.

[121] S. M. Sherman and R. W. Guillery. Functional organization of thalamocortical relays. *J Neurophysiol*, 76(3):1367–95, 1996.

[122] S. M. Sherman and R. W. Guillery. On the actions that one nerve cell can have on another: distinguishing "drivers" from "modulators". *Proc Natl Acad Sci U S A*, 95(12):7121–6, 1998.

[123] S. Murray Sherman and R. W. Guillery. *Exploring the thalamus*. Academic Press, San Diego, 2001.

[124] S. Murray Sherman and C. Koch. Thalamus. In Gordon M. Shepherd, editor, *The synaptic organization of the brain*, pages 289–328. Oxford University Press, New York, 4th edition, 1998.

[125] A. M. Sillito, J. Cudeiro, and P. C. Murphy. Orientation sensitive elements in the corticofugal influence on centre-surround interactions in the dorsal lateral geniculate nucleus. *Exp Brain Res*, 93(1):6–16, 1993.

[126] A. M. Sillito and H. E. Jones. Corticothalamic interactions in the transfer of visual information. *Philos Trans R Soc Lond B Biol Sci*, 357(1428):1739–52, 2002.

[127] A. M. Sillito, H. E. Jones, G. L. Gerstein, and D. C. West. Feature-linked synchronization of thalamic relay cell firing induced by feedback from the visual cortex. *Nature*, 369(6480):479–82, 1994.

[128] M. F. Simoni, G. S. Cymbalyuk, M. E. Sorensen, R. L. Calabrese, and S. P. DeWeerth. A multiconductance silicon neuron with biologically matched dynamics. *IEEE Trans Biomed Eng*, 51(2):342–54, 2004.

[129] W. Singer and C. M. Gray. Visual feature integration and the temporal correlation hypothesis. *Annu Rev Neurosci*, 18:555–86, 1995.

[130] G. D. Smith, C. L. Cox, S. M. Sherman, and J. Rinzel. Fourier analysis of sinusoidally driven thalamocortical relay neurons and a minimal integrate-and-fire-or-burst model. *J Neurophysiol*, 83(1):588–610, 2000.

[131] W. R. Softky. Modeling thalamus as a non-rectifying predictive comparator. *Unpublished (http://www.rni.org/bsoftky/index.html)*, 1996.

[132] W. R. Softky and C. Koch. The highly irregular firing of cortical cells is inconsistent with temporal integration of random epsps. *J Neurosci*, 13(1):334–50, 1993.

[133] M. Steriade. To burst, or rather, not to burst. *Nat Neurosci*, 4(7):671, 2001.

[134] M. Steriade, L. Domich, and G. Oakson. Reticularis thalami neurons revisited: activity changes during shifts in states of vigilance. *J Neurosci*, 6(1):68–81, 1986.

[135] M. Steriade and P. Wyzinski. Cortically elicited activities in thalamic reticularis neurons. *Brain Res*, 42(2):514–20, 1972.

[136] C. F. Stevens. Interactions between intrinsic membrane protein and electric field. an approach to studying nerve excitability. *Biophys J*, 22(2):295–306, 1978.

[137] H. A. Swadlow and A. G. Gusev. The impact of 'bursting' thalamic impulses at a neocortical synapse. *Nat Neurosci*, 4(4):402–8., 2001.

[138] S. Thorpe, D. Fize, and C. Marlot. Speed of processing in the human visual system. *Nature*, 381(6582):520–2, 1996.

[139] Wilson A. Truccolo and Dawei W. Dong. Dynamic temporal decorrelation: An information-theoretic and biophysical model of the functional role of the lateral geniculate nucleus. *Neurocomputing*, 38-40:993–1001, 2001.

[140] D. Ulrich and J. R. Huguenard. Gamma-aminobutyric acid type b receptor-dependent burst-firing in thalamic neurons: a dynamic clamp study. *Proc Natl Acad Sci U S A*, 93(23):13245–9, 1996.

[141] D. Ulrich and J. R. Huguenard. Gaba(a)-receptor-mediated rebound burst firing and burst shunting in thalamus. *J Neurophysiol*, 78(3):1748–51, 1997.

[142] B. V. Updyke. Topographic organization of the projections from cortical areas 17, 18 and 19 onto the thalamus, pretectum and superior colliculus in the cat. *J Comp Neurol*, 173(1):81–122, 1977.

[143] W. M. Usrey. The role of spike timing for thalamocortical processing. *Curr Opin Neurobiol*, 12(4):411–7, 2002.

[144] W. M. Usrey, J. M. Alonso, and R. C. Reid. Synaptic interactions between thalamic inputs to simple cells in cat visual cortex. *J Neurosci*, 20(14):5461–7, 2000.

[145] W. M. Usrey, J. B. Reppas, and R. C. Reid. Specificity and strength of retino-geniculate connections. *J Neurophysiol*, 82(6):3527–40., 1999.

[146] S. C. Van Horn, A. Erisir, and S. M. Sherman. Relative distribution of synapses in the a-laminae of the lateral geniculate nucleus of the cat. *J Comp Neurol*, 416(4):509–20, 2000.

[147] Jonathan D. Victor and Keith P. Purpura. Metric-space analysis of spike trains: theory, algorithms and application. *Network: Computation in Neural Systems*, 8(2):127–164, 1997.

[148] M. von Krosigk, T. Bal, and D. A. McCormick. Cellular mechanisms of a synchronized oscillation in the thalamus. *Science*, 261(5119):361–4, 1993.

[149] W. Wang, H. E. Jones, I. M. Andolina, T. E. Salt, and A. M. Sillito. Focal activation of feedback from v1 to lgn shifts cell firing patterns between bursting and tonic modes. In *Society for Neuroscience Abstracts*, volume 27, page 1913, 2001.

[150] B. S. Webb, C. J. Tinsley, N. E. Barraclough, A. Easton, A. Parker, and A. M. Derrington. Feedback from v1 and inhibition from beyond the classical receptive field modulates the responses of neurons in the primate lateral geniculate nucleus. *Vis Neurosci*, 19(5):583–92, 2002.

[151] G. D. Weese, J. M. Phillips, and V. J. Brown. Attentional orienting is impaired by unilateral lesions of the thalamic reticular nucleus in the rat. *J Neurosci*, 19(22):10135–9, 1999.

[152] T. G. Weyand, M. Boudreaux, and W. Guido. Burst and tonic response modes in thalamic neurons during sleep and wakefulness. *J Neurophysiol*, 85(3):1107–18., 2001.

[153] A. R. Willms, D. J. Baro, R. M. Harris-Warrick, and J. Guckenheimer. An improved parameter estimation method for hodgkin-huxley models. *Journal of Computational Neuroscience*, 6(2):145–168, 1999.

[154] John Wolfe and Jason Moyer.

[155] K. A. Zaghloul and K. Boahen. Optic nerve signals in a neuromorphic chip i: Outer and inner retina models. *Ieee Transactions on Biomedical Engineering*, 51(4):657–666, 2004.

[156] K. A. Zaghloul, K. Boahen, and J. B. Demb. Different circuits for on and off retinal ganglion cells cause different contrast sensitivities. *J Neurosci*, 23(7):2645–54, 2003.

[157] X. J. Zhan, C. L. Cox, J. Rinzel, and S. M. Sherman. Current clamp and modeling studies of low-threshold calcium spikes in cells of the cat's lateral geniculate nucleus. *J Neurophysiol*, 81(5):2360–73, 1999.

[158] X. J. Zhan, C. L. Cox, and S. M. Sherman. Dendritic depolarization efficiently attenuates low-threshold calcium spikes in thalamic relay cells. *J Neurosci*, 20(10):3909–14, 2000.